UNIVERSITY OF BELGRADE

FACULTY OF ELECTRICAL ENGINEERING

Taufik Mohamed G Taluo

CONTROL ALGORITHM OF BRUSHLESS DOUBLY-FED RELUCTANCE GENERATOR UNDER UNBALANCED GRID VOLTAGE CONDITIONS

Doctoral Dissertation

Belgrade, 2023

УНИВЕРЗИТЕТ У БЕОГРАДУ

ЕЛЕКТРОТЕХНИЧКИ ФАКУЛТЕТ

Тауфик Мохамед Г Талуо

Алгоритам управљања двострано напајаним релуктантним генератором у условима несиметричног мрежног напона

докторска дисертација

Београд, 2023

Ментор/Mentor (Supervisor):

Др Лепосава Ристић, ванредни професор,
    Универзитет у Београду- Електротехнички факултет

Dr Leposava Ristić, Associate professor,
    (University of Belgrade, School of Electrical Engineering)

Чланови комисије/Committee members:

1. Др Жељко Ђуровић, редовни професор,
    Универзитет у Београду- Електротехнички факултет

Dr. Željko Đurović, Full Professor,
    (University of Belgrade, School of Electrical Engineering)

2. Др Богдан Брковић, доцент,
    Универзитет у Београду- Електротехнички факултет

Dr. Bogdan Brković, Assistant Professor,
    (University of Belgrade, School of Electrical Engineering)

3. Др Веран Васић, редовни професор,
    Универзитет у Новом Саду - Факултет техничких наука

Dr. Veran Vasić, Full Professor,
    (University of Novi Sad - Faculty of Technical Sciences)

4. Др Жељко Ђуришић, ванредни професор,
    Универзитет у Београду- Електротехнички факултет

Dr. Željko Đurišić, Associate professor,
    (University of Belgrade, School of Electrical Engineering)

5. Др Младен Терзић, ванредни професор,
    Универзитет у Београду- Електротехнички факултет

Dr. Mladen Terzić, Associate professor,
    (University of Belgrade, School of Electrical Engineering)

Defense date / датум одбране: _____

Title of doctoral dissertation:

Control Algorithm of Brushless Doubly-Fed Reluctance Generator under Unbalanced Grid Voltage Conditions

Abstract:

The growing demand for electrical energy, especially from renewable sources, has motivated the scientific community to develop new technologies for producing electrical energy more efficiently, reliably and economically. Over the years, many wind energy conversion system (WECS) topologies with large wind turbines have been proposed, which may be generally classified into three types: fixed speed, variable speed with a partial scale power converter, and variable speed with a full-scale power converter.

Wind turbines based on doubly fed induction generators (DFIGs), with converters rated at about 25%-30% of the generator rating, have been widely used for large-scale wind generation because of their ability to provide variable speed operation and independent active and reactive power control in a cost-effective way.

More recently, a brushless doubly-fed reluctance generator (BDFRG) has been proposed as a potential alternative to the existing solutions for wind power applications since it retains most of their merits while offering high reliability.

The BDFRG is a prominent economical solution regarding reliability and maintenance of brushes and slip-rings which are characteristic problems of the traditional DFIG in WECS. Such advantages should be particularly attractive for off-shore wind turbines, where the operation and maintenance costs of brush generators are considerable.

Since wind power plants are often installed in remote areas with weak grids where unbalanced voltages are common which may force the wind generator to be disconnected from the grid, this research work has been dedicated to and focused on the performance and control of the BDFRG under unbalanced grid voltage conditions (UGVCs). A new control algorithm is developed and proposed in this thesis based on vector control. Application of this algorithm provides an increase in the robustness of the system, as well as an improvement in controllability.

In order to achieve this goal, the research work in this thesis was conducted as follows:

1. A review of the existing literature on the topic of the doctoral thesis was carried out in order to identify the best solutions for the synthesis of the control algorithm in the considered case;

2. Dynamic models of the BDFRG were developed under conditions of unsymmetrical (unbalanced) grid voltage by applying equations for the direct and inverse system;

3. A new control algorithm based on vector control was developed with the aim of eliminating the negative influence of components of the inverse voltage system on the performance of the wind generator.

4. The performance of the proposed control algorithm was analyzed using computer simulations in Matlab/Simulink software;

5. The performance of the proposed control algorithm was analyzed using Maxwell / Simplorer / Simulink co-simulation for the small-scale BDFRG;

6. A 1.5 MW BDFRG was designed for implementation in real-time simulations;

7. The performance of a newly designed large-scale wind generator with the implemented new control algorithm was analyzed under conditions of unsymmetrical grid voltage on a HIL setup, where the C code is compiled in dSPACE® from a Simulink® model using Real-Time Workshop.

Based on the research conducted according to the introduced plan, the main scientific contributions are formulated and presented in the thesis.

Keywords: Wind energy, brushless doubly-fed reluctance generator, unbalanced grid voltage, design methodology, Maxwell/Simplorer/Simulink co-simulation, Hardware-In-the-Loop

Scientific area:

Electrical engineering and computer science

Narrow scientific area:

Power converters and drives

Наслов докторске дисертације:

Алгоритам управљања двострано напајаним релуктантним генератором у условима несиметричног мрежног напона.

Апстракт:

Растућа потражња за електричном енергијом, посебно из обновљивих извора, мотивисала је научну заједницу последњих деценија да развија нове технологије за ефикаснију, поузданију и економичнију производњу електричне енергије. Добар пример за то представља производња електричне енергије из енергије ветра, која је последњих година у сталном порасту.

Током година је предложено много различитих системских решења за примену ветроагрегата велике снаге, која се генерално могу сврстати у три категорије: топологије са непроменљивом брзином, топологије са променљивом брзином и енергетским претварачем парцијалне снаге ветроагрегата и топологије са променљивом брзином и енергетским претварачем пуне снаге ветроагрегата.

Двострано напајани асинхрони генератори (Doubly-fed Induction Generator, DFIG) код којих се ротор напаја из енергетског претварача чија снага износи око 25%–30% номиналне снаге генератора, широко су заступљени у системима са ветроагрегатима велике снаге због њихове важне карактеристике да раде са променљивом брзином и независном контролом активне и реактивне снаге на економичан начин.

У новије време се двострано напајани релуктантни генератор без четкица на ротору (Brushless Doubly-Fed Reluctance Generator, BDFRG), у даљем тексту само двострано напајани релуктантни генератор јер се код савремених машина са релуктантним ротором подразумева да немају четкице на овом делу машине, предлаже као потенцијална алтернатива постојећим решењима у ветроенергетици. BDFRG, задржавајући већину предности постојећих решења, нуди и високу поузданост у раду. BDFRG представља економично решење за проблеме које има класичан DFIG са поузданошћу и одржавањем четкица и клизних прстенова у системима за конверзију енергије ветра у електричну

енергију (Wind Energy Conversion Systems, WECS). Као што је поменуто, ове особине су од посебног интереса за ветроелектране на мору, код којих су значајни трошкови рада и одржавања четкица ветрогенератора.

Будући да се ветроелектране често постављају у удаљеним руралним подручјима, где је очекивано присуство слабих мрежа са несиметричним (неуравнотеженим) напонима који могу да доведу до искључења ветрогенератора са мреже, истраживачки рад спроведен у овој докторској дисертацији посвећен је и фокусиран на перформансе и управљање BDFRG-ом у условима несиметричног мрежног напона. У раду је развијен и предложен нови алгоритам управљања заснован на векторском управљању. Применом овог алгоритма обезбеђује се повећање робусности система на појаву инверзних компоненти мрежног напона, као и укупно побољшање перформанси система као резултат примене јнапређеног начина управљања.

Да би се остварио овај циљ, истраживачки рад у тези је спроведен на следећи начин:

1. Извршен је детаљан преглед постојеће литературе из области докторске тезе у циљу идентификације најбољих решења за синтезу алгоритма управљања у разматраном случају;

2. Динамички модели BDFRG-а развијени су у условима несиметричног мрежног напона применом једначина за директан и инверзни систем;

3. Развијен је нови алгоритам управљања заснован на векторском управљању са циљем елиминисања негативног утицаја компоненти инверзног напонског система на перформансе ветрогенератора;

4. Перформансе предложеног алгоритма управљања анализиране су коришћењем рачунарских симулација у софтверу Matlab/Simulink;

5. Перформансе предложеног алгоритма управљања су анализиране коришћењем Maxwell / Simplorer / Simulink косимулације за BDFRG мале снаге;

6. BDFRG од 1,5 MW је пројектован за примену у симулацијама у реалном времену;

7. Перформансе новопројектованог ветрогенератора велике снаге са имплементираним новим алгоритмом управљања анализиране су у условима несиметричног мрежног напона на HIL поставци, где се С код компајлира у dSPACE® из Simulink ® модела користећи Real-Time Workshop.

На основу истраживања спроведеног према утврђеном плану, формулисани су и представљени главни научни доприноси у докторској дисертацији.

Кључне речи: ветроенергетика, двострано напајани релуктантни генератор, несиметричан мрежни напон, пројектовање машина, Maxwell/Simplorer/Simulink косимулација, Hardware-In-the-Loop

Научна област:

Електротехника и рачунарство

Ужа научна област:

Енергетски претварачи и погони

Acknowledgement

First, and foremost, I would like to express my deepest gratitude to my supervisor, Dr. Leposava Ristić (Associate Professor), for her inspiring guidance, valuable suggestions, keen interest, and continuous encouragement during the course of the project. The completion of this work would not have been possible without her continuous support.

I would also like to thank Dr. Milutin G Jovanovic (Associate Professor) who has been consistently providing continuous and unlimited support and invaluable suggestions.

I would also like to express my sincere gratitude to Dr. Bogdan Brković (Assistant Professor) and Dr. Mladen Terzić (Associate Professor) for their continuous and unlimited support during the doctoral study period.

My appreciation also goes out to the ministry of higher education, the State of Libya for their trust by presenting the financial support of my Ph.D. scholarship.

My special gratitude goes to my parents for a lifetime of support and their endless love and consistent efforts to support me.

Finally, I would like to express my gratitude to my wife Marwa, and my children Ala, Mohamed, and Musab for their unflagging support throughout, and seemingly endless patience with me. Without their tremendous understanding and encouragement in the past few years, it would be impossible for me to complete my study.

Table of contents

List of Figures

List of Tables

Abbreviations and Symbols

Abbreviations

WECS	wind energy conversion system
DFIG	doubly fed induction generator
BDFRG	brushless doubly-fed reluctance generator
MPPT	maximum power point tracking
SCIG	squirrel-cage induction generator
PMSG	permanent magnet synchronous generators
BDFM	brushless doubly-fed machine
BDFRM	brushless doubly-fed reluctance machine
BDFIM	brushless doubly-fed induction machine
DFRM	doubly-fed reluctance machine
SyncRM	synchronous reluctance machine
IM	Induction machine
VOC	voltage oriented control
FOC	field-oriented control
MRAS	model reference adaptive system
MTPIA	maximum torque per inverter ampere
DPC	direct power control
UGVCs	unbalanced grid voltage conditions
PDPC	predictive direct power control
LVRT	low voltage ride through
RTI	real time implementation
HIL	hardware in the loop
MSC	machine side converter
GSC	grid side converter
FEA	finite element analysis
MMF	magentomotive force
PFOC	primary field-oriented control
PVOC	primary voltage-oriented control
SC	scalar control
V/f control	voltage/frequency control
MSVC	machine side vector control
VUF	voltage unbalance factor
PLL	phase-locked loop
SVM	space vector modulation
MOO	multi-objective optimization

Symbols

P_m	mechanical power [W]
ρ	air density
R	radius of the turbine rotor [m]
v_w	average wind speed [m/sec]
Cp	power coefficient
λ	tip speed ratio
β	pitch angle
ω_{rm}	rotor mechanical angular speed [rad/s]
I_g	gearbox ratio
T_t	output torque of the wind turbine [Nm]
g^{-1}	Inverse air-gap function
θ	angle around the air-gap [rad]
P_p	number of poles of the primary winding
P_s	number of poles of the secondary winding
P_r	number of rotor poles
$\widehat{F}_p$	peak primary magentomotive force [A-turns]
$\widehat{F}_s$	peak secondary magentomotive force [A-turns]
N_{ph_p}	total number of turns per phase (primary)
N_{ph_s}	total number of turns per phase (secondary)
ω_p	primary angular frequency [rad/sec]
ω_s	secondary angular frequency [rad/sec]
f_p	electrical frequency of the primary winding [Hz]
f_s	electrical frequency of the secondary winding [Hz]
f_r	electrical frequency regarding the rotor [Hz]
ω_{sync}	synchronous angular speed [rad/sec]
s	degree of slip
$\underline{u}_p$	primary winding voltages [V]
$\underline{u}_s$	secondary winding voltages [V]
$\underline{\lambda}_p$	primary flux [Wb]
$\underline{\lambda}_s$	secondary flux [Wb]
λ_{ps}	mutual flux linkage [Wb]
R_p	primary winding resistance [Ω]
R_s	secondary winding resistance [Ω]
L_p	primary winding inductance [H]
L_s	primary winding inductance [H]

L_{ps}	primary to secondary mutual inductance [H]
σ	leakage factor
$\underline{i}_p$	primary current [A]
$\underline{i}_s$	secondary current [A]
p_p	primary active power [W]
q_p	primary reactive power [VAr]
p_s	secondary active power [W]
q_s	secondary reactive power [VAr]
γ_{torque}	torque angle [rad]
u_{pd}, u_{pq}	primary direct and quadrature voltage components [V]
i_{pd}, i_{pq}	primary direct and quadrature current components [A]
$\lambda_{pd}, \lambda_{pq}$	primary direct and quadrature flux components [Wb]
u_{sd}, u_{sq}	secondary direct and quadrature voltage components [V]
i_{sd}, i_{sq}	secondary direct and quadrature current components [A]
$\lambda_{sd}, \lambda_{sq}$	secondary direct and quadrature flux components [Wb]
T_e	electromagnetic torque [Nm]
n_r	rotor speed [rpm]
P_{cu_p}	primary copper losses [W]
P_{cu_s}	secondary copper losses [W]
η	Efficiency
P_{st}	stator power [W]
U_r	Rotor voltage [V]
R_f	resistance of the grid side filter [Ω]
L_f	inductance of the grid side filter [H]
ξ	damping ratio
ω_n	the undamped natural frequency [rad/sec]
P_{av}	DC component of the active power [W]
P_1, P_2	amplitude of oscillating terms of the active power [w]
Q_1, Q_2	amplitude of oscillating terms of the reactive power [w]
T_{av}	DC component of the torque [Nm]
T_1, T_2	amplitude of oscillating terms of the torque [Nm]
B	flux density [T]
β	normalized flux density
λ_r	rotor pole pitch
C_{ij}	coupling factor
h	space harmonic
N_s	number of slots

N_r	number of rotor ducts
$N_{s\text{-}p}$	slots per pole per phase primary winding
$N_{s\text{-}p}$	slots per pole per phase secondary winding
δ	air gap length [mm]
ℓ	Length of stator core[mm]
J	current density [A/mm^2]
A_l	linear current density [A/m]
$\sigma_{\tan}$	average tangential stress [kPa]
N_{cond}	number of conductors per slot
D_{gap}	air gap diameter [m]
D_o	outer diameter of stator(mm)
D	inner diameter of stator(mm)
D_{ri}	inner diameter of rotor
Sl_o	slot opening(mm)
S_y	stator yoke length(mm)
S_{tw}	stator tooth width(mm)
α_t	temperature coefficient
t_{stat}	considered temperature in stator windings (C^o)
t_{amb}	ambient temperature (C^o)
L_{wire}	total wire length [mm]
S_{cu}	conductor cross-sectional area [mm^2]
$N_{t\text{-}p}$	Number of turns per slot(primary)
$N_{t\text{-}s}$	Number of turns per slot(secondary)

Superscripts

$+, -$	positive, negative components
$*$	reference value for controller

Subscripts

α, β	stationary α-β axis
d, q	synchronous d-q axis
p, s	primary, secondary
b	base
d	designed

Chapter 1

Introduction

1.1 **Introduction**

Wind power has been used for thousands of years by humans to produce mechanical energy (mills, irrigation and sailing boats) [1, 2]. The application of the kinetic energy of the wind for the generation of electric energy had its origin at the end of the 19th century. However, it was only from the 1960s onwards that there were sufficient investments to promote the advancement of wind energy conversion into electrical energy. In the 70's, during the oil crisis, with the awareness of the problems caused by the burning of fossil fuels and with government subsidies, the generation of electrical energy from wind energy was boosted [3].

There are many factors that have contributed to the increase of interest in wind energy in the last decades [3]. The first one refers to the need to look for alternative sources. The second reason was the large potential of wind energy, as it is available everywhere on the earth and in some places with a particularly high energy density. Third, there was the technological capacity. In particular, at that time there was a huge progress in other industrial fields, especially related to power electronics, which revolutionized the way wind energy could be extracted. The remaining two factors refer to the new vision of how to use the wind energy, technically and commercially, and the political will to achieve that.

The growing demand for electrical energy, especially from renewable sources, has motivated the scientific community in the last decades to develop new technologies for producing electrical power more efficiently, reliably and economically. Wind energy source is a good example of this trend; especially electrical energy generation from wind power has grown significantly in recent years. The increasing size of wind turbines resulted in new grid codes [4].

The main purpose of this chapter is to define and present the scientific framework of the thesis proposal based on published research assessing the use of a Brushless Doubly Fed Reluctance Generator (BDFRG) in variable speed systems for wind power energy conversion and their control under different grid conditions.

1.2 **Modeling of Wind Turbine Aerodynamics**

Wind turbines are used to turn the power of the wind into mechanical energy. The mechanical power captured by from the rotor blades P_m can be expressed as in (1.1),

$$P_m = \frac{1}{2}\pi\rho R^2 C_p(\lambda,\beta)v_w^3, \tag{1.1}$$

where, ρ is the air density assumed to be constant, R is the radius of the turbine rotor, v_w is the average wind speed, and C_p is the power coefficient which is given as a function of tip speed ratio λ and the pitch angle β. The tip speed ratio λ is defined as:

$$\lambda = \frac{\omega_{rm}R}{v_w I_g}, \tag{1.2}$$

where ω_{rm} is the rotor speed and I_g is the gearbox ratio.

Chapter1. Introduction

The performance of the wind turbine can be evaluated by the value of the power coefficient C_p, which represents the ratio between the power available at the rotor and the power that can be extracted by the turbine blades from the wind (i.e. it indicates the efficiency of the wind turbine). The theoretical maximum permissible value for C_p is known as the Betz limit. The maximum value of this coefficient is 0.59. The coefficient C_p can be approximated by several different possible non-linear functions. One of the most commonly used expressions is given by (1.3),

$$C_p(\lambda, \beta) = c_1 \left(\frac{c_2}{\lambda_i} - c_3\beta - c_4 \right) \exp^{\left(\frac{c_5}{\lambda_i} \right)} + c_6\lambda,$$ (1.3)

where

$$\frac{1}{\lambda_i} = \left(\frac{1}{\lambda + 0.08\beta} - \frac{0.035}{\beta^3 + 1} \right)$$ (1.4)

The coefficients c_1, c_2, c_3, c_4, c_5 and c_6 depend on the aerodynamic characteristics of the wind turbine, and are obtained empirically as in Table 1.1.

Table 1.1 Value of the aerodynamic coefficients

c_1	c_2	c_3	c_4	c_5	c_6
0.7105	250	0.4	25	26	0.010868

With the parameters defined for the wind turbine, the turbine output power with the trajectory of maximum power point tracking MPPT power is shown in Figure 1.1.
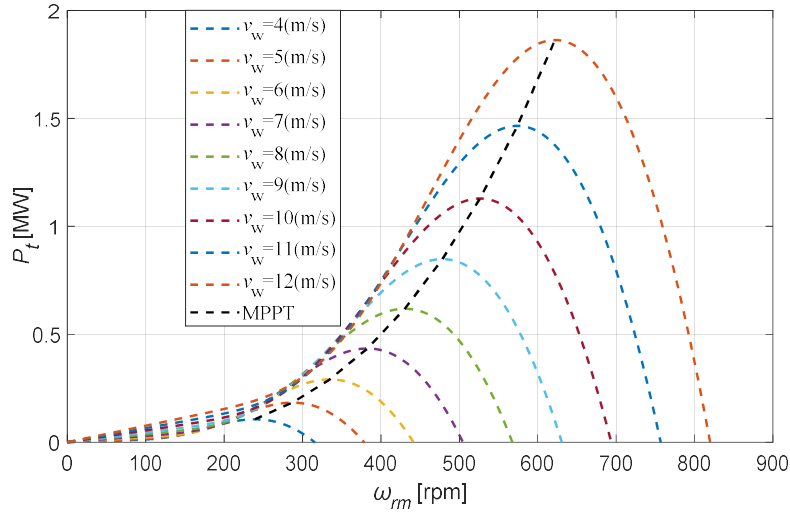
Figure 1.1. Output power of the turbine versus rotor speed with MPPT

The mechanical output torque of the wind turbine T_t, that is, the torque at the input of the gearbox, is defined by the equation:

$$T_t = \frac{P_t}{\omega_t} = \frac{P_t I_g}{\omega_{rm}}$$ (1.5)

While the input torque of the generator T_m (i.e. the torque at the output of the gearbox) is defined by the equation (1.6),

$$T_m = \frac{P_m}{\omega_{rm}} = \frac{P_m}{\omega_t I_g}$$

(1.6)

Assuming that the friction and the slip losses of the gearbox are neglected, thus, the power at the input of the gearbox is considered the same as the power at the output.

$$T_t \omega_t = T_m \omega_{rm}$$

(1.7)

Input (drive) torque on the shaft of the BDFRG is shown in Figure 1.2.
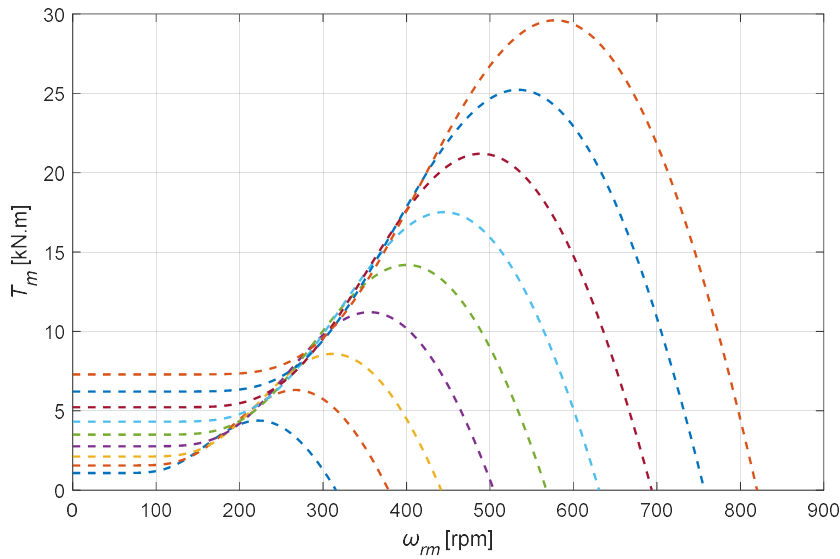
Figure 1.2. Input torque of the generator versus rotor speed

1.3 **Overview of existing wind energy conversion system topologies**

Over the years, different system topologies have been put forward, which may be generally classified into three types: fixed speed, variable speed with a partial scale power converter and variable speed with a full scale power converter [5, 6], as simplified in Figure 1.3.
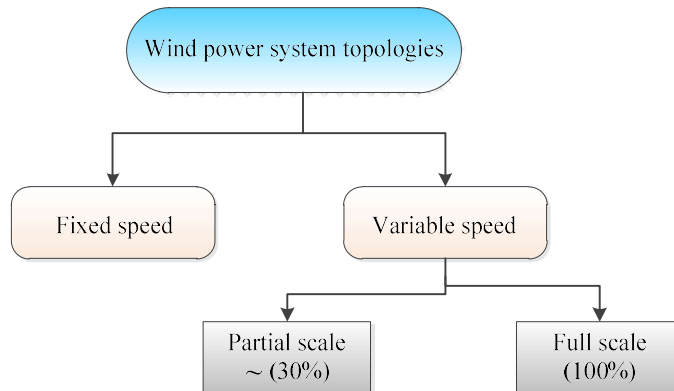
Figure 1.3. General classification of WECS topologies

1.3.1 Fixed speed WECS

The fixed-speed WECSs have already been used with a multiple-stage gearbox and a squirrel-cage induction generator (SCIG) directly connected to the grid through a soft-starter and transformer [1, 6] as illustrated in Figure 1.4.

Since the SCIG always absorbs reactive power from the grid, this concept was extended with a capacitor banks installed to correct the power factor at each wind generator. Smoother grid connection is achieved by incorporating a soft-starter, which limits the inrush current to the induction generator during start-up [1, 5-7].

The fixed-speed WECS has the advantage of being simple in construction, robust, reliable and has low initial costs. The main drawbacks of this system can be summarized as follows [1, 5-7]:

- Uncontrollable reactive power consumption,
- Mechanical stress and limited power quality control
- Necessary application of a three-stage gearbox
- Necessary excitation from the stator terminals of SCIG. Therefore, it is impossible for this type to support grid voltage control by compensating reactive power.
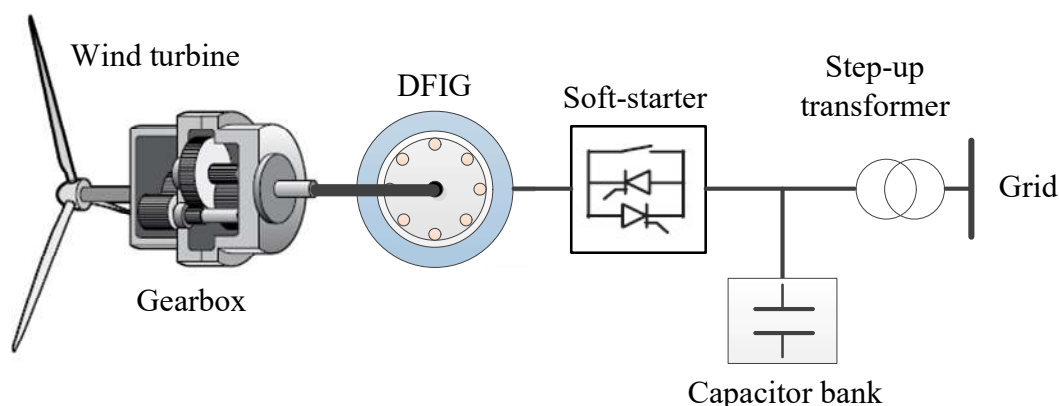
Figure 1.4. Schematic of a fixed-speed WECS with induction generator

1.3.2 Variable speed WECS

Variable-speed WECSs were designed to maximize wind power extraction over a broad range of wind speeds. With a variable-speed operation it has become possible to continuously regulate generator speed to match the maximum possible power that can be extracted with the wind turbine. Such a mechanism is known as the Maximum Power Point Tracking (MPPT) [8-10].

Other key advantages of variable speed operation are related to the increase of captured power, improvement of power quality and reduction of mechanical stress on the wind turbine. The disadvantages are increased cost of equipment because of the power converters application and accordingly their power losses.

Currently, the most common configurations of variable-speed WECS depend on the rating of the power converter.

1.3.2.1 Variable speed WECS with partial scale power converter

A typical configuration shown in Figure 1.5 is known as the DFIG concept, which uses a partial-scale power converter (rated at approximately 30% of nominal (rated) generator power) and a wound-rotor induction generator with slip rings to transfer current between the converter and the rotor windings [1, 5-7].

The power converter performs the reactive power compensation, because the grid-side power converter can control reactive power flow, independently of the generator operation.
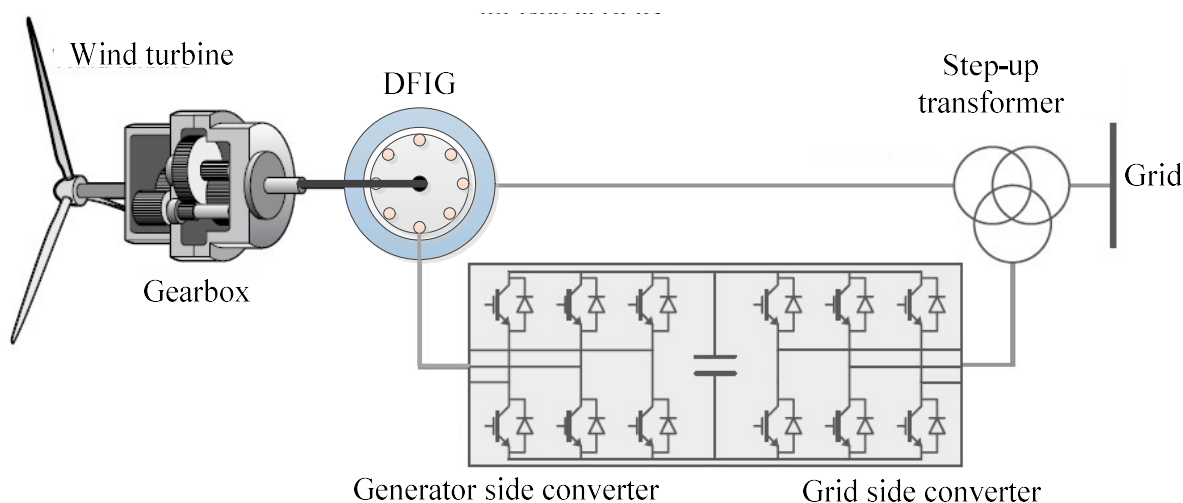
Figure 1.5. Typical configuration of doubly-fed induction generator WECS

A DFIG system can deliver active power to the grid through both the stator and the rotor side converter, while the rotor can also absorb power, depending on the generator mode of operation (sub/sub-synchronous). If the generator operates in super-synchronous mode, power will be delivered from the rotor to the grid via the converter, and if the generator operates in sub-synchronous mode, then the rotor will absorb power from the grid through the converter [5-7].

The main disadvantage of DFIG system is the use of brushes and slip rings to connect the wound rotor to the power converter. The aforementioned components require regular maintenance, which in turn increase the operating costs of the generating unit, especially on offshore wind farms. In addition, a multi-stage gearbox is still necessary in the drive train to match turbine and generator speed [5].

1.3.2.2 Variable speed WECS with full scale power converter

The typical configuration of a variable speed WECS with a full-rated power converter is illustrated in Figure 1.8. In this type of WECS the generator is connected to the grid through a power converter that handles all of the generated power, which allows effective control of active and reactive power and smooth grid connection [1, 5, 6].

Fully scale converter WECSs may or may not have a gearbox depending on generator characteristics. Different types of electrical generators can be used, such as induction, wound-rotor synchronous or permanent magnet (PMSG) synchronous generators [1, 3, 5, 6].
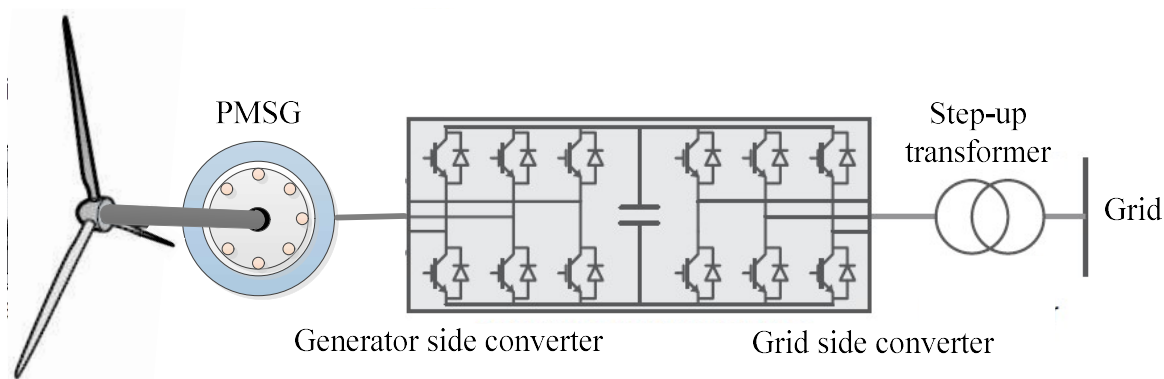
Figure 1.6. Gearless wind turbine with a permanent-magnet synchronous generator and a full-rated power converter

1.4 **Brief review of brushless doubly fed machines (BDFMs)**

The concept of BDFMs date back at the beginning of the 20th century [11], originally dating back to the patent registered by the Siemens brothers and Lydall in 1902.[12, 13] From then on, this kind of machine has experienced three major development stages [14, 15]. In the first stage, around the 1910-1920s, Hunt and Creedy researched the concept of self-cascade machines, where two wound induction motors share a common shaft and the two sets of rotor windings are electrically self-cascaded [16, 17]. Since the two sets of rotor windings are self-cascaded, there was no need for brushes or slip rings as shown in Figure 1.7.
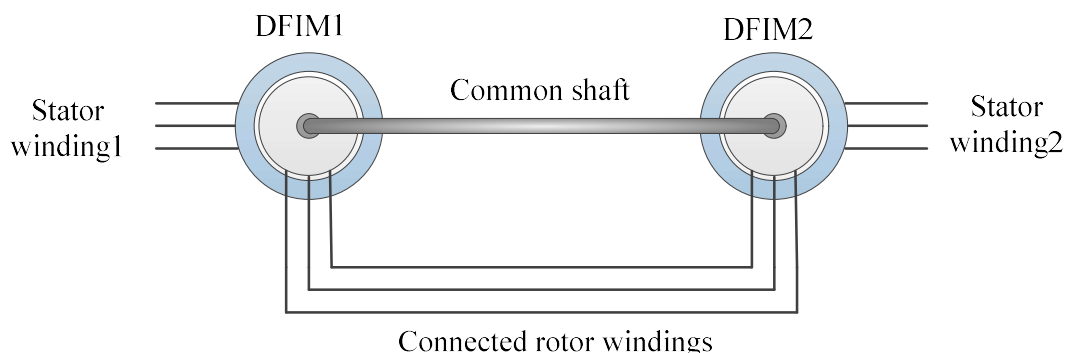
Figure 1.7. Two induction machines in cascade connection

Further improvements related to BDFM were made by Broadway, Thomas, Kusko, Somuah and others in 70s [18-21]. A single stator winding was proposed by merging the two sets of stator windings applying dual-tapped stator windings wound into a common stator core. Along the time, they sought two distinct rotors, the nested cage rotor and the salient reluctance rotor.

Further work on the subject has been presented around 1980 by Heyne and El-Antably to manufacture the Broadway's version of BDFM, but did not produce significant torque density and energy efficiency for practical applications [14, 21].

In 90s the brushless doubly fed reluctance machine (BDFRM) gained a quite attention, mainly motivated by the rapid progress in modern power electronics [15]. Since then, many papers have been published to unveil more of the BDFRM principles, operational characteristics, control methods and applications. In 1991, a transient machine model of a doubly fed reluctance motor and the 'dq' model were presented in [22, 23].

A methodology for steady-state performance analysis and design of the DFRM was presented in [24], and subsequently, investigations of the electromagnetic principles of the BDFRM performance continued [25, 26]. The authors in [27] introduced a comparison between the Synchronous Reluctance Machine (SyncRM) and the BDFRM, where some aspects such as torque capacity, efficiency and inverter ratings were addressed by the authors. The same authors presented a comparative theoretical analysis and aspects of practical implementation of the important control strategies and associated machine performance/inverter size trade-offs for the BDFRM [28, 29].

Along the years, different control strategies have been reported in the literature. They can be mainly categorized as: scalar control [30-34], vector control, which can be voltage oriented control (VOC) or field-oriented control (FOC) [35-37] and direct torque control [30, 38, 39]. These control techniques can be rotor position sensor based or sensor-less [40], established through different position or speed estimation methods, including Model Reference Adaptive System (MRAS) [37, 41-43], or observer-based schemes for speed, as well as torque (and flux) control [44]. The underlying control strategies have different objectives such as: power-winding unity power factor [36, 45], minimum converter current or maximum torque per inverter ampere (MTPIA), minimum copper losses, maximum power factor [36], reactive power and torque control [46] or Direct Power Control (DPC) [47-50]. Besides, other approaches such as Open-Winding-Based control [51, 52], improved Particle Swarm Optimization to adequately track the speed [53], etc. have also been documented [54].

1.5 WECS under unbalanced grid voltage conditions

The wind power plants are often installed in remote rural areas, where it is usually characterized by weak grids with unbalanced voltages [55-57]. Under UGVCs, negative-sequence components are present in the grid voltage, influencing problems for wind generators such as unbalanced primary currents, secondary current harmonics, unequal heating or hot spots in the windings [58] which degrade the insulation and reduce the life expectancy of the windings. The interaction between negative-sequence voltage and positive-sequence current generate power pulsations and a pulsating torque, which may cause extra mechanical stress on the drivetrain and gearbox [58-63] and may even affect the system to be unable to perform as recommended with grid codes [64, 65]. The wind turbines might have to be disconnected from the grid under UGVCs [66] due to unbalanced stator current and power, as well as torque pulsations. On the other hand, recent grid codes require wind turbines to withstand a maximum value of 2% of grid voltage unbalance without tripping [67, 68].

The conventional control systems for DFIG based on voltage oriented control (VOC) theory, have been used for controlling such systems under normal conditions [69]. However, further improvements of the control algorithm have to be made for controlling the positive and negative sequence components of the rotor current under unbalanced grid conditions, in order to eliminate the torque ripple and the active power pulsations. Various control strategies have been proposed in the literature for the DFIG under UGVCs. The system performance and control of DFIG based wind turbine under UGVCs have been studied in [65-67, 70-75]. Even though many studies have presented advances along last years, there is still a lack of research on the performance of BDFRG under unbalanced grid voltage conditions. A new mathematical model for the BDFRG under UGVCs has been introduced in [61] using positive and negative sequence equations, where the

machine equivalent circuit in the *d-q* reference frame is presented, as well as the torque and the power equations were developed. Furthermore, a real-time separation method is introduced to separate the negative sequences from its positive sequences.

The authors of [61] have provided mathematical proof of the BDFRG model under UGVCs in [76], where the space vector and *dq* models in the relative positive and negative sequence reference frames were derived from the time domain equations of the BDFRG. In addition, the model was simulated in MATLAB/Simulink in order to demonstrate the operation of the BDFRG under UGVCs. The same authors have used the model introduced in [61] to develop a Predictive DPC (PDPC) method for the BDFRG under UGVCs in [58]. The proposed PDPC is based on a power compensation strategy aiming to achieve two control objectives: balancing the primary currents and mitigating the electromagnetic torque pulsations. However, the impact of unbalanced grid voltage on the primary active power and the secondary current has not been fully investigated.

In [77] the authors proposed an extended vector control strategy to increase the immunity to a negative sequence voltage component and to improve the controllability of such unbalanced grid conditions. The dynamic model in MATLAB/Simulink was developed in order to investigate the behavior of BDFRG during UGVCs. Methods to separate positive and negative sequence components in real time have been also developed in this paper.

1.6 **Research Motivation**

The main motivations for establishing control of the BDFRG under unbalanced grid conditions could be summarized as follows:

- The BDFRG is one of the most promising machines, which gained a significant attention in the recent years, because of its reasonable cost, high reliability of brushless structure, and competitive performance with the conventional wound or cage rotor induction machine, or the brushless doubly-fed induction machine (BDFIM) counterpart [78].
- The BDFRG retains all of the cost benefits of the DFIG associated with using partially-scaled power converters, especially in applications with limited speed ranges (e.g. wind turbines) where the converter rating, size and cost can be further reduced [34].
- Wind turbines are often installed in remote areas with weak grids where unbalanced voltages are common occurrence [77, 79].
- The power system transient stability issues with high penetration of WECS in recent years and consequently their big impact on the electricity system steady-state and dynamic operation. Therefore, under voltage dip conditions caused by faults within the grid, wind generators have to stay connected and act similarly to conventional power plants providing active power control, frequency regulation and dynamic voltage control, as well as low voltage ride through (LVRT).

1.7 **Aim and Contribution**

The main purpose of this thesis is to investigate and develop vector control strategies for large scale BDFRG based WECS under unbalanced grid voltage conditions, which has not been widely

covered in literature. For that purpose, a detailed review and systematization of existing research was conducted in the field of modeling and control of DFIG and BDFRG in conditions of unbalanced grid voltage, with an emphasis on the application of BDFRG in systems for the conversion of wind energy into electricity.

Theoretical clarification has been carried out in the thesis in order to contribute to a better understanding of the performance of WECS with BDFRG in conditions with unbalanced grid voltages. A model for the BDFRG unbalanced operation has been put forward using positive and negative sequence equations. This model has been used to develop a new vector control (VC) method for the BDFRG under unbalanced grid conditions, which in turn allows taking into account grid codes requirements.

Preliminary design of a large scale BDFRG using Ansys Maxwell software has been conducted in order to verify the two newly developed and proposed control algorithm on a hardware in the loop (HIL) setup.

Demonstration of the effectiveness of the proposed control algorithm has been performed on three levels:

1. Computer simulations with MATLAB/SIMULINK

2. Maxwell / Simplorer / Simulink co-simulation for the small-scale BDFRG;

3. Real-time simulations of a newly designed large scale BDFRG using HIL development platform.

As the BDFRG is a very complex machine to design, initially a design was developed for a low-power BDFRG (1.5 kW) for which basic dimensions and parameters could be found in the literature. Then the dimensions were scaled in order to complete the design for a large scale BDFRG (1.5 MW) in accordance with the procedure based on the existing literature in this research field. The parameters of the large scale BDFRG were determined using the analytical method for parameter calculation and the FEM model. The goal of this doctoral dissertation was to analyze the performance of the BDFRG within a real wind energy conversion system that is of high power (several MW). This analysis had to be conducted in accordance with the current regulative for unbalanced grid voltage conditions, and by applying two new and original control algorithms, developed in the thesis as its main contribution. Therefore, it was necessary to design large scale machine for high power applications and to determine its parameters.

1.8 **Thesis Outline**

The remaining thesis content is organized in the following way:

Chapter 2 presents the fundamental principles of BDFRG operation including electromagnetic considerations. Both the steady state and dynamic modeling aspects are presented.

Chapter 3 introduces a detailed analysis of the three commonly used control algorithms, i.e. scalar control, vector control, and DTC. The vector control methods for the machine side converter (MSC) and grid side converter (GSC) are presented, together with design principles of proportional-integral (PI) controllers and the calculation of their parameters.

Chapter 4 presents the main aspects, the mathematical model of a BDFRG under unbalanced grid conditions, and the developed advanced vector control strategy. An extended vector control

algorithm is used to control both the positive and negative sequence components of the secondary currents independently to achieve different targets.

Chapter 5 focuses on the design of a large-scale BDFRG by deriving the design parameters from a small-scale machine. Some fundamental issues concerning the BDFRG design are addressed. The performance of a 1.5 MW design is examined through finite element analysis (FEA) employing Ansys Maxwell software.

Chapter 6 investigates the optimized control algorithm performances. The improved control algorithm has been examined and validated in two manners: using Maxwell/Simplorer/Simulink co-simulation (for a small-scale machine) and the Hardware-In-the-Loop (HIL) system (for a large-scale machine).

Conclusions of the research work presented in the thesis with emphasized contributions and plans for future work are given in Chapter 7.

Chapter 2

Operating Principles of BDFRM

2.1 **Introduction**

BDFRG is an attractive solution in variable speed applications with limited speed ranges owing to the high reliability of the brushless structure and the low cost of a partially rated converter. It has all the advantages of doubly-fed machines, with operating flexibility and control techniques similar to those of DFIG. Thus, it can operate at synchronous, super-synchronous and sub-synchronous speeds in the motor and generator operating modes [28, 80]

The rotor with half of the total number of the stator poles provides magnetic coupling between the two stator windings. The presence of the variable reluctance rotor position-dependent path modulates the magnetomotive force (MMF) waveforms of the two windings in both spatial and temporal terms, leading to linking the flux harmonic side-bands of each winding with the fundamental MMF of the complementary winding [50, 81, 82].

2.2 **Electromagnetic principles**

The performance of the BDFRM highly depends on the capability of the rotor to modulate stator magnetic fields in order to establish magnetic coupling between the stator windings that otherwise interact. The unusual electromagnetic field interaction limits the use of traditional machine analysis and needs the consideration of the associated phenomena simultaneously. The operating principles of the BDFRM are well discussed in the literature [22-26].

2.2.1 Air-gap modeling by using the salient pole rotor

In order to make the analysis feasible, some assumptions are considered [25]:

- The iron of the machine has infinite permeability
- The two sets of three phase windings of the machine will be assumed to be adequately modelled as spatially sinusoidally distributed windings.
- The stator currents are represented by sinusoidal waveforms.
- Concerning the system topology, the primary winding is directly connected to the grid under normal operating conditions and the secondary winding is converter fed.

Additionally, it is considered that air gap function can be modeled as in [25],

$$g^{-1}(\theta, \theta_{rm}) = m + n \cos[P_r(\theta - \theta_{rm})], \qquad (2.1)$$

where the constants *m* and *n* are real numbers, satisfying $m \geq n > 0$; P_r is the number of rotor poles; θ_{rm} is the rotor mechanical angle; θ is the angle around the air-gap. Figure 2.1 shows a graphical representation of the inverse air gap function, in accordance to (2.1).
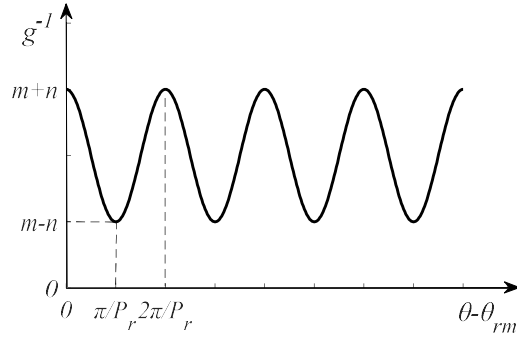
Figure 2.1. Inverse air-gap function in accordance to (2.1)

Assume that the primary and secondary three phase windings are fed with three phase sinusoidal currents, the fundamental component of the three-phase MMFs can be calculated as in [24, 25, 83],

$$\begin{cases} F_{p3\phi}(\theta,t) = \hat{F}_p \cos(\omega_p t - \dfrac{P_p}{2}\theta) \\[2mm] F_{s3\phi}(\theta,t) = \hat{F}_s \cos(\omega_s t - \alpha - \dfrac{P_s}{2}\theta) \;, \\[2mm] F_{total}(\theta,t) = F_{p3\phi}(\theta,t) + F_{s3\phi}(\theta,t) \end{cases} \tag{2.2}$$

where P_p is the number of poles of the primary winding; P_s is the number of poles of the secondary winding; $\hat{F}_p$ and $\hat{F}_s$ are the peak primary and secondary MMFs given in (2.3),

$$\hat{F}_p = \frac{3}{2} \cdot \frac{4}{\pi} \frac{N_{ph\_p} K_{w\_p}}{P_p} I_p, \qquad \hat{F}_s = \frac{3}{2} \cdot \frac{4}{\pi} \frac{N_{ph\_s} K_{w\_s}}{P_s} I_s, \tag{2.3}$$

where $N_{ph\_p,s}$ are the total number of turns per phase and $K_{w\_p,s}$ are the winding factors.

For different combinations of pole numbers, the three-phase MMFs produced from the two winding sets (only the fundamental component is considered) are shown in Figure 2.2
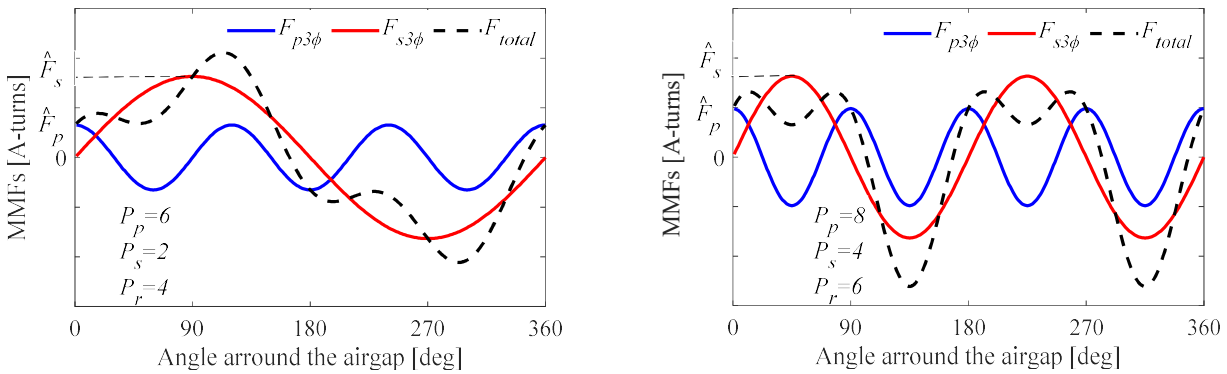
Figure 2.2.Three-phase MMFs for each winding

Considering only the fundamental component of the MMFs, one can reasonably expect some difficulties on designing a BDFRM, since the total MMF is not sinusoidal and will be further modulated by the rotor [13].

The flux density distribution along the air gap can be computed as in [25],

$$B(\theta,\theta_{rm},t) = \mu_0 g^{-1}(\theta,\theta_{rm})F_{total}(\theta,t),\tag{2.4}$$

where μ_0 represents the vacuum magnetic permeability. Most research studies assumed that m an n in (2.1) as $m = n = G/2$, $G = 1/gap$, where G is the minimum air-gap length. Carrying out some manipulations, the air-gap flux density due to the primary, as well as secondary winding is obtained and presented with following expressions:

$$B_p(\theta,\theta_{rm},t) = \frac{\mu_0 G\hat{F}_p}{2}\left\{\begin{array}{l}\cos(\omega_p t - \dfrac{P_p}{2}\theta)+\\[2mm]\dfrac{1}{2}\left[\begin{array}{l}\cos((\omega_p - P_r\omega_{rm})t - (\dfrac{P_p}{2} - P_r)\theta)\\[2mm]+\cos((\omega_p + P_r\omega_{rm})t - (\dfrac{P_p}{2} + P_r)\theta)\end{array}\right]\end{array}\right\},\tag{2.5}$$

$$B_s(\theta,\theta_{rm},t) = \frac{\mu_0 G\hat{F}_s}{2}\left\{\begin{array}{l}\cos(\omega_s t - \dfrac{P_s}{2}\theta - \alpha)+\\[2mm]\dfrac{1}{2}\left[\begin{array}{l}\cos((\omega_s - P_r\omega_{rm})t + (P_r - \dfrac{P_s}{2})\theta - \alpha)\\[2mm]+\cos((\omega_s + P_r\omega_{rm})t - (P_r + \dfrac{P_s}{2})\theta - \alpha)\end{array}\right]\end{array}\right\},\tag{2.6}$$

where $\omega_{p,s}$ is the primary and secondary angular frequency respectively; ω_{rm} is the rotor mechanical angular speed in mech-rad/sec, $\theta_{rm} = \omega_{rm}t$ is the rotor mechanical angle, and P_r is the number of rotor poles.

It can be stated that the equations (2.5) and (2.6) have a fundamental field and two sidebands. The coupling between the winding sets is achieved if one of the sidebands of one winding couples the fundamental component of the complementary winding. This means that the two values including cosine terms of the secondary fundamental component in (2.6) and the primary harmonic component in (2.5) must be equal. It is worth noting that the fundamental component of each winding can be coupled with only one sideband of the complementary winding and the remaining sideband would be a leakage flux [25].

For instance, let us analyze one of the possible combinations which is coupling of the fundamental component from secondary winding with one of the sidebands from primary winding due to rotor modulation.

$$\cos\left((\omega_p - P_r\omega_{rm})t - (\frac{P_p}{2} - P_r)\theta\right) = \cos(\omega_s t - \frac{P_s}{2}\theta)\tag{2.7}$$

The following coupling conditions for electromagnetic torque production can be concluded from (2.7):

$$\left\{\begin{array}{l}\omega_p - P_r\omega_{rm} = \omega_s \rightarrow P_r\omega_{rm} = \omega_p - \omega_s\\[2mm]\qquad\qquad\text{or}\\[2mm]-\omega_p + P_r\omega_{rm} = \omega_s \rightarrow P_r\omega_{rm} = \omega_p + \omega_s\end{array}\right.,\tag{2.8}$$

and

$$\begin{cases} \dfrac{P_p}{2} - P_r = \dfrac{P_s}{2} \rightarrow P_r = \dfrac{P_p - P_s}{2} \\ \qquad\qquad \text{or} \\ -\dfrac{P_p}{2} + P_r = \dfrac{P_s}{2} \rightarrow P_r = \dfrac{P_p + P_s}{2} \end{cases} \qquad (2.9)$$

Similar analysis can be performed for each one of the four combinations between fundamental component and the two sidebands of the complementary winding as explained in Figure 2.3
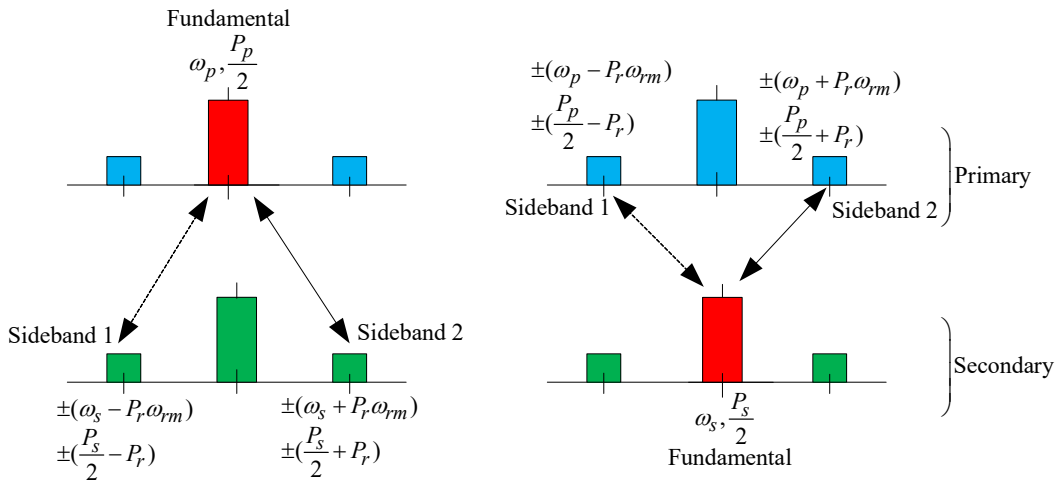
Figure 2.3. Coupling conditions for torque production of the BDFRM (adapted from [13])

2.3 Basic concepts

The BDFRG has two windings: the primary winding, known as the power winding, which is directly connected to the grid, and the secondary winding, known as the control winding, which is connected to the grid through a bidirectional power converter in back-to-back configuration as shown in Figure 2.4.
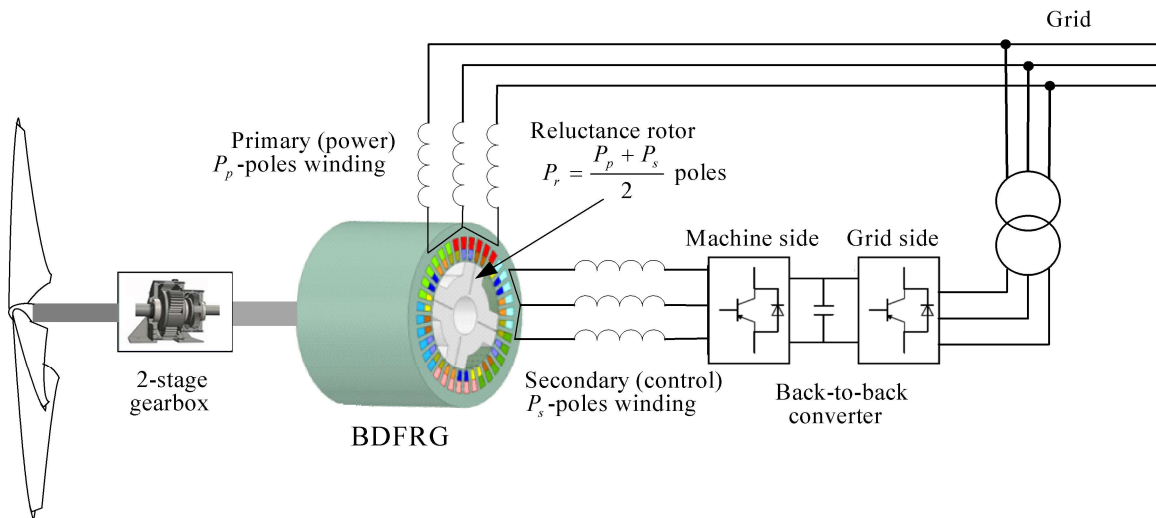
Figure 2.4. Conceptual block diagram of the BDFRG-based wind energy conversion system.

The number of rotor poles (P_r) is half the total number of poles of the stator, that is, it is equal to the sum of the pole pairs of the two windings:

$$P_r = \frac{P_p + P_s}{2}$$

(2.10)

In this way, the magnetic coupling between the two sets of windings depends on the reluctance of the rotor, that is, it depends on the position of the rotor shaft [27]. The electrical frequency of the machine rotor must be synchronized with the sum of the electrical frequencies of the primary and secondary windings [29]. As the frequency of the primary winding is constant, the frequency of the secondary winding varies with machine speed. The criterion for synchronizing the secondary winding is given by equation (2.11),

$$f_r = f_p + f_s \rightarrow f_s = f_r - f_p,$$

(2.11)

where, f_p is the electrical frequency of the primary winding, f_s represents the electrical frequency of the secondary winding, and f_r is the electrical frequency of the rotor.

The relationship between fundamental angular frequencies suitable for insight into electromechanical energy conversion and accordingly machine torque production is given in (2.12),

$$\omega_r = \frac{\omega_p + \omega_s}{P_r} = \frac{\omega_p}{P_r}(1 + \frac{\omega_s}{\omega_p}) = \omega_{sync}(1 + \frac{\omega_s}{\omega_p})$$

(2.12)

When the secondary winding is connected to DC voltage (i.e $\omega_s = 0$), the BDFRG operates in synchronous mode at $\omega_{sync} = \omega_p/P_r$, which is half of the synchronous speed of a P_r-pole DFIG. Thus, the BDFRG can be categorized as a medium-speed machine requiring a two-stage gearbox unlike the failures-prone 3-stage counterpart of the high-speed DFIG traditionally employed in these applications [84].

The rotor speed variation with the secondary winding frequency variation in the case of different rotor pole numbers is shown in Figure 2.5.
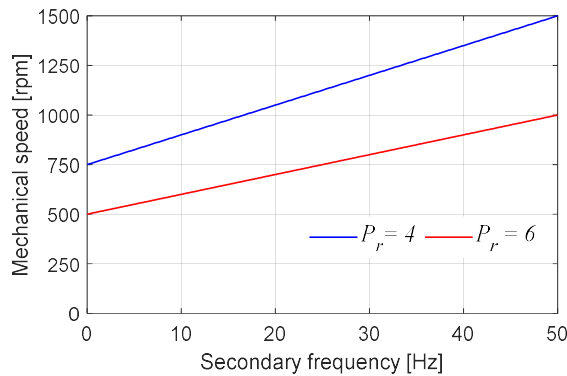
Figure 2.5. Variation of speed with secondary winding frequency when primary winding is connected to grid with 50 Hz frequency

In the BDFRM, the synchronous angular speed (ω_{syn}) is equal to the angular speed of the primary winding. Hence, the generalized slip can be defined as:

$$s = \frac{\omega_p - P_r\omega_{rm}}{\omega_p} = \frac{\omega_p - (\omega_p + \omega_s)}{\omega_p} = \frac{-\omega_s}{\omega_p} \tag{2.13}$$

2.4 Dynamic Model in Space-Vector Presentation

The dynamic model of BDFRM presented with the space vector equations can be found in detail in [26]. Based on this publication, a summary of the model is presented with equations from (2.14) to (2.17). The voltage and the flux space vector equations for the machine in a reference frame rotating at ω_p for the primary winding and $\omega_r - \omega_p$ for the secondary winding, assuming motoring convention, can be written as follows:

$$\underline{u}_p = R_p\underline{i}_p + \frac{d\underline{\lambda}_p}{dt} + j\omega_p\underline{\lambda}_p, \tag{2.14}$$

$$\underline{u}_s = R_s\underline{i}_s + \frac{d\underline{\lambda}_s}{dt} + j(\omega_r - \omega_p), \tag{2.15}$$

$$\underline{\lambda}_p = L_p\underline{i}_p + L_{ps}\underline{i}_{sm}^*, \tag{2.16}$$

$$\underline{\lambda}_s = L_s\underline{i}_s + L_{ps}\underline{i}_{pm}^* = \sigma L_s\underline{i}_s + \underbrace{\frac{L_{ps}}{L_p}\underline{\lambda}_p^*}_{\underline{\lambda}_{ps}}, \tag{2.17}$$

In these equations, $\underline{u}_p$ and $\underline{u}_s$ are the primary and secondary winding voltages respectively, while $\underline{\lambda}_p$ and $\underline{\lambda}_s$ are the corresponding fluxes. The remaining parameters are as follows: the primary and secondary winding resistances R_p and R_s, and self-inductances L_p and L_s, L_{ps} is the primary to secondary mutual inductance, $\sigma = 1 - L_{ps}^2/(L_pL_s)$ is the leakage factor, λ_{ps} is the mutual flux linkage, and "*"denotes a complex conjugate. All the vectors in the primary voltage and flux equations are stationary in a *dq* reference frame rotating at ω_p, and so are secondary counterparts but in a ω_s rotating *dq* reference frame shown in the phasor diagram in Figure 2.6. Note that $i_{sm} = i_s$ and $i_{pm} = i_p$ (in their respective frames) are the magnetically coupled currents from one machine side to the other, with the same magnitude albeit a different frequency to the original current vectors as a result of the frequency modulating action of the rotor [25, 85].
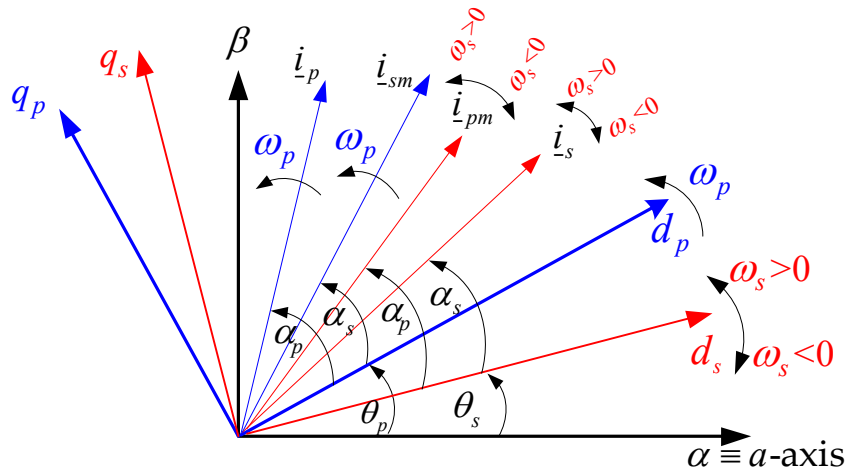
Figure 2.6. Reference frames and characteristic phasors

18

The ω_s defines the operating mode of the BDFRM (Figure 2.7), being able to work in three modes:

- Synchronous mode ($\omega_s = 0$, i.e. DC excitation), in this case the machine is essentially a conventional synchronous machine. Under this conditions when the secondary winding is not contributing any power to the system, the maximum power that can be produced by the machine is half that when the secondary winding is being fed from AC voltage source.

- Super-synchronous mode ($\omega_s > 0$), when $\omega_s = \omega_p$, case of maximum speed, the real power is shared equally by the two windings. If $\omega_s = \omega_p/2$, the real power flowing through the secondary winding is half the real power flowing through the primary winding - in this case the secondary winding is responsible for 1/3 of the total power.

- Sub-synchronous mode ($\omega_s < 0$), e.g. the opposite phase sequence of the secondary winding to the primary one. This mode of operation is inefficient because part of the real power is circulating through the machine, causing losses [25].
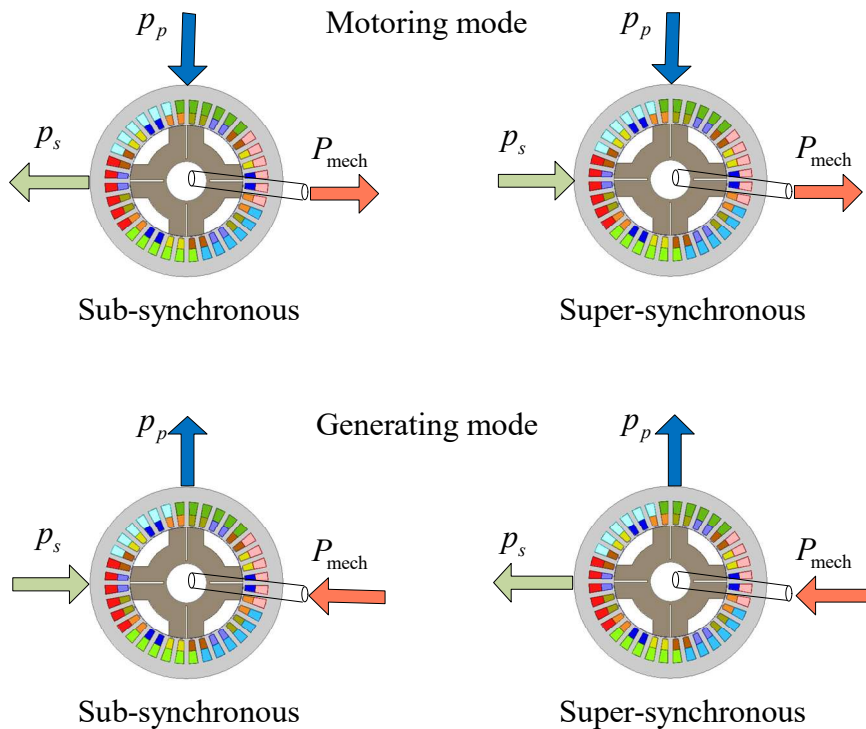
Figure 2.7. Operating modes and power flows for the BDFRM

The rotor is responsible for providing the coupling between the stator windings, satisfying equations (2.10) and (2.13). To better quantify the influence of the rotor, the expression of the electromagnetic torque in steady state is used, according to the equation (2.18).

$$T_e = \frac{3}{2} P_r L_{ps} i_p i_s \sin(\gamma_{\text{torque}}) \qquad (2.18)$$

In this equation, T_e is the electromagnetic torque and γ_{torque} is the torque angle (also called the load angle), and it depends on the phase shift between the primary and secondary winding currents and the initial rotor angle [25].

2.4.1BDFRM *d-q* Model

The advantage of using '*dq*' reference models is due to the fact that there are fewer variables than in the three-phase model. This makes it simpler to analyze and control the machine. The BDFRM space-vector model (2.14)-(2.17) in motoring mode in reference frames rotating at $\omega = \omega_p$ for the primary winding and $\omega = \omega_r - \omega_p$ for the secondary winding, can be further developed by using standard notation into the respective *dq* components as follows:

$$
\begin{cases}
u_{pd} = R_p i_{pd} + \dfrac{d\lambda_{pd}}{dt} - \omega_p \lambda_{pq} \\[2mm]
u_{pq} = R_p i_{pq} + \dfrac{d\lambda_{pq}}{dt} + \omega_p \lambda_{pd}
\end{cases}, \tag{2.19}
$$

$$
\begin{cases}
u_{sd} = R_s i_{sd} + \dfrac{d\lambda_{sd}}{dt} - (\omega_r - \omega_p)\lambda_{sq} \\[2mm]
u_{sq} = R_s i_{sq} + \dfrac{d\lambda_{sq}}{dt} + (\omega_r - \omega_p)\lambda_{sd}
\end{cases}, \tag{2.20}
$$

$$
\begin{cases}
\lambda_{pd} = L_p i_{pd} + L_{ps} i_{sd} \\[2mm]
\lambda_{pq} = L_p i_{pq} - L_{ps} i_{sq}
\end{cases}, \tag{2.21}
$$

$$
\begin{cases}
\lambda_{sd} = L_s i_{sd} + L_{ps} i_{pd} \\[2mm]
\lambda_{sq} = L_s i_{sq} - L_{ps} i_{pq}
\end{cases} \tag{2.22}
$$

The previous *d-q* equations can be developed to give expressions (2.23) and (2.24), which can be further used to establish the equivalent circuit shown in Figure 2.8.

$$
\left.
\begin{array}{l}
u_{pd} = R_p i_{pd} + \dfrac{d}{dt}(L_p i_{pd} - L_{ps} i_{pd}) + \dfrac{d}{dt}\left[L_{ps}(i_{pd} + i_{sd})\right] - \omega_p \lambda_{pq} \\[3mm]
u_{sd} = R_s i_{sd} + \dfrac{d}{dt}(L_s i_{sd} - L_{ps} i_{sd}) + \dfrac{d}{dt}\left[L_{ps}(i_{sd} + i_{pd})\right] - (\omega_r - \omega_p)\lambda_{sq}
\end{array}
\right\}, \tag{2.23}
$$

$$
\left.
\begin{array}{l}
u_{pq} = R_p i_{pq} + \dfrac{d}{dt}(L_p i_{pq} - L_{ps} i_{pq}) + \dfrac{d}{dt}\left[L_{ps}(i_{pq} - i_{sq})\right] + \omega_p \lambda_{pd} \\[3mm]
u_{sq} = R_s i_{sq} + \dfrac{d}{dt}(L_s i_{sq} - L_{ps} i_{sq}) + \dfrac{d}{dt}\left[L_{ps}(i_{sq} - i_{pq})\right] + (\omega_r - \omega_p)\lambda_{sd}
\end{array}
\right\} \tag{2.24}
$$

The *d-q* model equations are very similar to those of the induction machine, which means that the BDFRM is equivalent to a wound rotor induction machine with $2P_r$-pole [26, 80]. The corresponding equivalent circuit is shown in Figure 2.8.
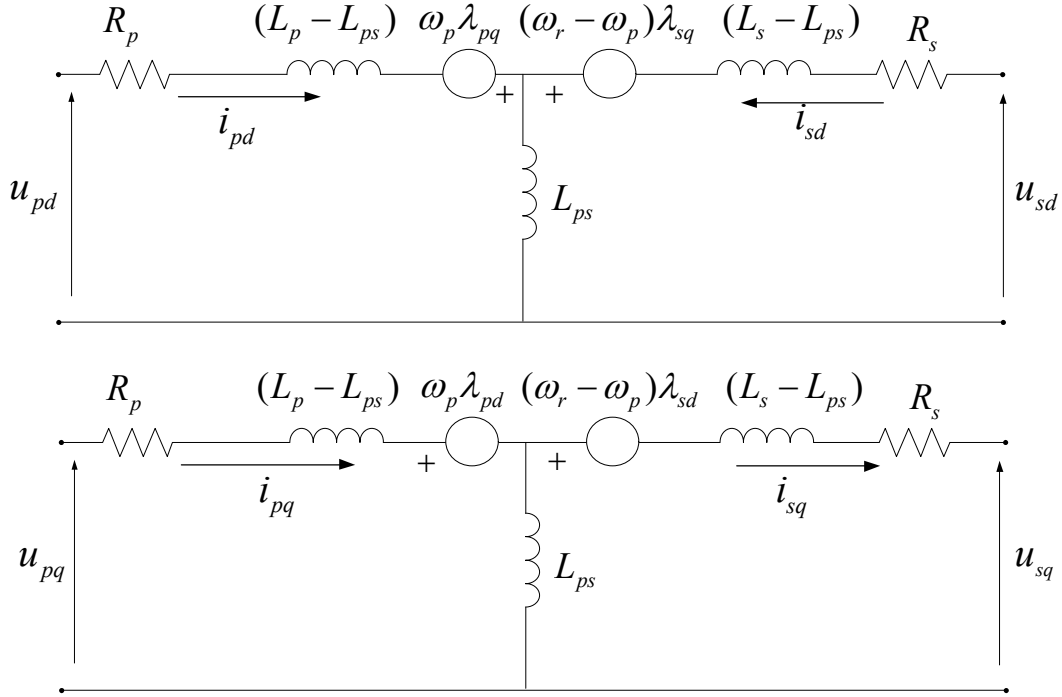
Figure 2.8. *d-q* equivalent circuit of BDFRM

The expression (2.25) is chosen among various expressions for the BDFRM electromagnetic torque representation. Thus, it can be concluded that the electromagnetic torque only appears as a function of flux variations in the primary winding and the secondary current. In this way, the electromagnetic torque can be controlled by the secondary current [25, 26], while the primary fluxes (λ_{pd} and λ_{pq}) are approximately constant (primary winding is connected directly to the grid). Secondary currents (i_{sd} and i_{sq}) are controlled by the power converter.

$$T_e = \frac{3}{2}\frac{P_r L_{ps}}{L_p}(\lambda_{pd}i_{sq} + \lambda_{pq}i_{sd}) \tag{2.25}$$

The mechanical equation for a single lumped inertia load (*J*), used in the model for simulation purposes is given with (2.26):

$$\omega_{rm} = \frac{1}{J}\int(T_e - T_{\text{Load}} - B_g\omega_{rm})dt \tag{2.26}$$

Figure 2.9. Ideal Dynamic Model of BDFRM for Simulations with Matlab/Simulink

The mechanical power equation presented in (2.27) shows the individual contributions of each winding.

$$P_m = T_e \omega_{rm} = \underbrace{\frac{T_e \omega_p}{P_r}}_{p_p} + \underbrace{\frac{T_e \omega_s}{P_r}}_{p_s} = p_p(1 + \frac{\omega_s}{\omega_p}) = p_p(1 - s) \cdot \qquad (2.27)$$

The machine operating mode is determined by the power flow on the primary side, i.e. from the grid for motoring ($T_e > 0$), and to the grid for generating ($T_e < 0$), while the secondary can absorb or deliver active power subject to the winding phase sequence, i.e. the ω_s sign: the BDFRM would absorb (produce) positive secondary power at super (sub)-synchronous speeds as a motor, and at sub (super)-synchronous speeds as a generator.

Table 2.1. Power flow for typical operating modes

Speed mode	Motor $T_e > 0$	Generator $T_e < 0$
Sub-synchronous ($\omega_s < 0$)	$p_p > 0$ & $p_s < 0$	$p_p < 0$ & $p_s > 0$
Super-synchronous ($\omega_s > 0$)	$p_p > 0$ & $p_s > 0$	$p_p < 0$ & $p_s < 0$

2.5 Starting procedure

Because a partially-scaled power converter is used, the starting current of the secondary winding must be limited below the rated value of the used power converter. To achieve a soft starting, the BDFRM is started as an induction machine. In this case, auxiliary contactors are needed to short-circuit the secondary winding terminals directly or via external resistors to prevent the inverter

transient over currents and allow the BDFRM to start as an unloaded induction machine [30, 85, 86].

On the other hand, the machine could be started with the shorted primary windings using the inverter, and then self-synchronize it to the grid for doubly-fed operation, following the procedure similar to that used for commercial DFIM drives [86, 87].

2.6 **Steady-State Analysis of BDFRGs**

A study of the steady-state characteristics is useful to understand the BDFRM performance in a broader spectrum. It shows how the speed and the power are affected by the applied secondary voltage.

The steady state equations for the BDFRM can be written as:

$$\underline{U}_p = R_p \underline{I}_p + j\omega_p(L_p - L_{ps})\underline{I}_p + j\omega_p L_{ps}(\underline{I}_p + \underline{I}_s^* e^{j\gamma}) , \tag{2.28}$$

$$\frac{\underline{U}_s e^{j\gamma}}{s} = \frac{R_s}{s}\underline{I}_s^* e^{j\gamma} + j\omega_p(L_s - L_{ps})\underline{I}_s^* e^{j\gamma} + j\omega_p L_{ps}(\underline{I}_s^* e^{j\gamma} + \underline{I}_p) , \tag{2.29}$$

where the *p* subscript denotes the primary winding and the *s* subscript denotes the secondary winding.

It is worth noting that the frequencies of the primary and the secondary sides of the machine are different, therefore this fact is applied in the main steady-state equations. The coupled equivalent circuit is obtained by defining a relationship between the two frequencies being applied to the system. This relationship is derived in terms of a slip. Hence, the secondary parameters have not been referred to the primary winding in a turns ratio sense (or vice-versa). However, a frequency referencing operation has been carried out [25]. The corresponding equivalent circuit drawn from these equations is shown in Figure 2.10.
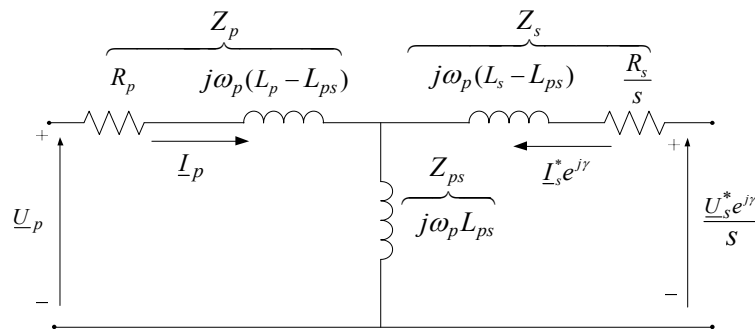
Figure 2.10. The steady-state equivalent circuit of the BDFRM

Compared with the DFIM equivalent circuit, one can observe a great deal of similarity in form despite the entirely different operating principles of the two machines. This model is virtually exactly the same as the per-phase steady state model of DFIM derived in [88]. The angle γ in (2.28) and (2.29) is the torque angle, and it depends on the phase shift between the primary and secondary winding currents and the initial rotor angle. The output torque of the BDFRM can be expressed as follows,

$$T_e = \frac{3}{2} P_r L_{ps} I_p I_s \sin(\overbrace{\alpha - \theta_{r_0}}^{\gamma}),$$

(2.30)

where α is the phase shift between the primary and secondary currents, and θ_{r0} is the initial rotor angle. Equation (2.30) reveals that the output torque of the machine is directly proportional to rotor pole number (P_r), peak variation of mutual coupling between the windings (L_{ps}), and peak currents in both the windings (I_p, I_s). Inspection of (2.30) indicates that if α is zero, torque has its maximum value when the initial rotor angle is 90 degrees. In that case, the self and mutual fluxes are orthogonal in both windings.

If the secondary is shorted in Figure 2.10, the model becomes equivalent to a traditional SCIM. This reinforces the close connection between the modeling of the BDFRM and the IM. It also designates the ability of the BDFRM to work as an induction machine in case of inverter failure.

The primary and secondary currents can be calculated from the steady-state equivalent circuit using the superposition theorem as follows:

$$\underline{I}_p = \frac{(Z_s + Z_{ps})\underline{U}_p - Z_{ps}\dfrac{\underline{U}_s^*}{s}e^{j\gamma}}{Z_p Z_{ps} + Z_p Z_s + Z_s Z_{ps}},$$

(2.31)

$$\underline{I}_s^* = \frac{Z_{ps}\underline{U}_p e^{-j\gamma} - (Z_p + Z_{ps})\dfrac{\underline{U}_s^*}{s}}{Z_p Z_{ps} + Z_p Z_s + Z_s Z_{ps}}.$$

(2.32)

When the rotor rotates at synchronous speed, the secondary current falls to zero and the primary current becomes a no-load current and has a minimum value. It means that, in order to obtain the same conditions when the wind speed drops, the secondary currents should be set to zero at some value of the slip. For a BDFRG, this could be achieved by applying an appropriate voltage to the secondary circuit. At the given slip, and zero secondary current (i.e. at virtual synchronous speed), the secondary voltage which has to be applied during wind speed drop to keep the machine working as a generator can be calculated as:

$$\underline{I}_s = 0 \Rightarrow \underline{U}_s = (\frac{sZ_{ps}}{(Z_p + Z_{ps})}\underline{U}_p e^{-j\gamma})^*$$

(2.33)

According to the BDFRM presentation given in the previous section, a 1.5 MW, 690 V, 50 Hz BDFRG with its parameters listed in Table 2.2, is considered for analysis and calculation of characteristic values for the generator operation of the BDFRG.

Firstly, the equivalent circuit is solved in motor operating mode with short-circuited secondary. In this case, the analysis is then performed on the generator runs super-synchronously, assuming the same efficiency and power factor as in motor mode.

In order to assess the effect of the secondary voltage on the performance of the BDFRG, the analysis is then performed in the case of wind speed drop. In this case, the secondary voltage should be applied, and the BDFRG works in a sub-synchronous generator regime

Table 2.2. The parameters of the DFIG and BDFRG

Parameter	DFIG	BDFRG
Rated power (MW)	1.5	1.5
Line voltage (V)	690	690
Stator, rotor poles	6	8/4, 6
Synchronous speed (rpm)	1000	500
Power winding resistance (Ω)	0.0014	0.005103
Power winding inductance (H)	0.001616	0.00237
Control winding resistance (Ω)	0.00099	0.006827
Control winding inductance (H)	0.0016081	0.0044334
Mutual inductance (H)	0.001526	0.002924

By neglecting both friction and iron losses, the BDFRM in a motor operating mode with short-circuited secondary, develops full shaft power at 492.7 rpm, i.e. at slip s=1.46%. By solving the equivalent circuit for the motor full-load operating point, the following quantities (Table 2.3) are calculated:

Table 2.3. The results for the BDFRM full-load operating point (U_S=0)

n_r(rpm)	s%	I_p(kA)	I_s(kA)	p_p(MW)	q_p(MVAr)	P_{cu_p}(kW)	P_{cu_s}(kW)	P_m(MW)	η	$\cos\phi$
492.7	1.46	1.6214	1.0138	1.48	1.24	40.248	21.050	1.421	95.86	0.7648

Let's assume that the BDFRM generates its rated power for wind speed v_w=10.3 m/s with λ=7 and C_p=0.4, with the same efficiency and power factor as in motor mode. The turbine radius used in turbine design is R=42 m, and the power is easily determined from the following expression:

$$P_m = \frac{1}{2}\pi\rho R^2 C_p v_w^3 = p_p \tag{2.34}$$

The corresponding turbine angular speed is:

$$\omega_t = \frac{\lambda \times v_w}{R} = 1.7167 \text{rad/s} \tag{2.35}$$

By solving the equivalent circuit of the BDFRM with short-circuited secondary (U_s=0), the machine will generate 1.4802 MW of active power at a rotor speed of n_r=506.82 rpm (super-synchronous mode) and slip s=−1.36%. The quantities for the generator mode of operation were calculated and reported in Table 2.4.

Table 2.4. The results for the BDFRG full-load operating point (U_S=0)

n_r(rpm)	s%	I_p(kA)	I_s(kA)	p_p(MW)	q_p(MVAr)	P_{cu_p}(kW)	P_{cu_s}(kW)	P_m(MW)	η	$\cos\phi$
506.82	−1.36	1.589	0.986	−1.4217	1.2588	38.648	19.92	−1.4802	96.04	−0.7487

The gearbox ratio for a six-pole machine with rated load slip $s=-1.36\%$ can be calculated as follows:

$$I_g = \frac{\omega_r}{\omega_t} = \frac{506.82 \times \pi / 30}{1.7167} = 1: \ 30.92 \tag{2.36}$$

In the previous calculations, a short-circuited secondary machine has been considered for rated-load generator operation, with the rated speed in the super-synchronous range (506.82 rpm).

In order to keep the machine working as a generator in the sub-synchronous range (i.e. for lower wind speeds), a proper voltage should be applied to the secondary winding. Let's assume that the wind speed drops to v_w=9.8 m/s, according to (2.34), the mechanical power at this wind speed is 1.278 MW. In this case, the turbine angular speed will drop to 1.6333 rad/s and the rotor speed becomes 482.265 rpm. This speed can be moved to the generator mode speed range (i.e. the synchronous speed can be virtually lowered below 482.26 rpm), by applying an appropriate secondary voltage. The new synchronous speed can be calculated as:

$$n_{syn\_new} = \frac{482.265}{(1-s)} = \ 475.775 \ \text{rpm} \cdot \tag{2.37}$$

The corresponding actual slip, based on the original synchronous speed (n_{syn}=500 rpm), is:

$$S_{new} = \frac{n_{sync} - n_{sync\_new}}{n_{sync}} = \ 0.0484 \ . \tag{2.38}$$

This slip value is substituted into (2.33) to calculate the secondary voltage, obtaining the value given in (2.39).

$$\underline{U}_s = 25.23 \angle 90° \, \text{V} \tag{2.39}$$

2.6.1 The Results of Comparison between DFIG and BDFRG

The calculation has been performed for the same turbine and wind speed range, as well as the same rated power of 1.5 MW of machines with six poles on their rotors, BDFRM and DFIM. The obtained results presented in Figure 2.11 show a great deal of similarity in performance for both machines.

When both machines, the DFIM and the BDFRM, operate as induction generators, they generate the same active power (about 1.43 MW). On the other hand, the DFIG absorbs 1.218 MVAr of reactive power, while the BDFRG absorbs 1.2588 MVAr of reactive power. In this case, the power factor and machine efficiency are, respectively: (0.767, 98%) for DFIG and (0.7487, 96%) for BDFRG.

By applying the calculated control voltage, a new operating point is obtained. The results for the new operating point when the generators run sub-synchronously are summarized in Table 2.5. In this case, the BDFRG produces about 50% of its rated power, while the DFIG produces only about 14% of its rated power.

Table 2.5. Steady-state characteristics at the new operating point

DFIG	n_r (rpm)	I_s (kA)	I_r (kA)	P_{st} (MW)	P_{cu} (kW)	η %
	954.86	0.3972	0.485	-0.201	1.36	99.3
BDFRG	n_r (rpm)	I_p (kA)	I_s (kA)	p_p (MW)	P_{cu} (kW)	η %
	482.26	0.634	0.665	-0.757	15.2	98

It is worth noting that the control voltage calculated above is valid only for the new operating point; when the wind speed changes, a new calculation based on the new slip is required. The control voltage to be applied as a function of the wind speed is shown in Figure 2.12.
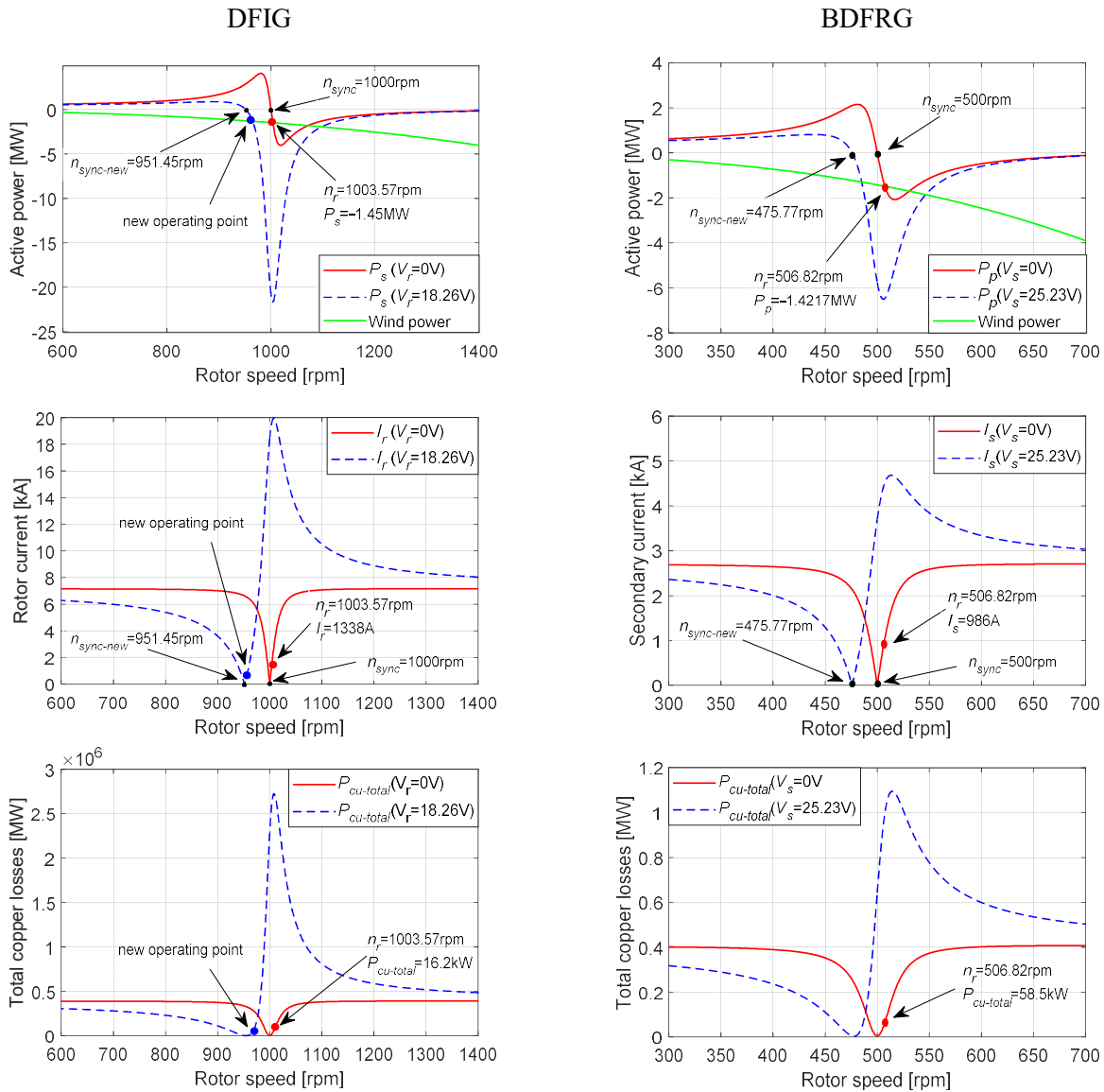
Figure 2.11. Results of comparison between DFIM and BDFRM natural (U_r, $U_s = 0$) and modified (U_r, $U_s \neq 0$) characteristics
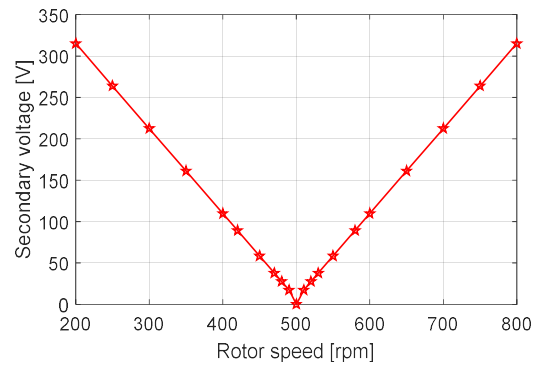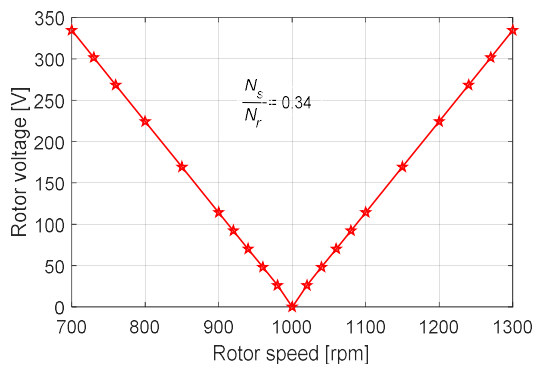
Figure 2.12. Control voltage vs rotor speed for DFIM (left) and BDFRM (right)

Chapter 3

BDFRG Control Methods

3.1 **Introduction**

The control of BDFRG is important for its optimal operation. Regarding the WECS, various control techniques to extract maximum power from the wind turbine have been reported in the literature over the years. The most cited control methods are classified in the literature as: scalar control (SC) [30-33], Vector-Oriented Strategies, which can be primary voltage oriented control (PVOC) or primary field-oriented control (PFOC) [35-37] and direct torque control (DTC) [30, 38, 39]. These control techniques can be shaft position sensor based or without a rotor position sensor [40], achieved using different position or speed estimation methods, including Model Reference Adaptive System (MRAS) [37, 41], or observer-based schemes for speed, as well as torque (and flux) control [44]. In [43] a new sensorless MRAS control was proposed and evaluated for inherently decoupled torque and reactive power control.

The three commonly used control algorithms, i.e. scalar control, vector control and DTC would be further discussed in detail in this chapter.

3.2 **Scalar Control**

Scalar control, often called V/f control, is considered a simple control algorithm in which the air-gap flux is kept almost at its maximum value for the best torque production. Thus, to keep the flux constant, the voltage must vary with frequency and the *V/f* ratio must be kept constant. Sudden changes in speed and frequency are cause for attention as they can initiate operational instability. Thus, this control technique is suitable for systems where steady-state, rather than dynamic, performance is of main concern (such as fans, pumps, compressors, blowers and similar loads) [89].

In order to determine an adequate *V/f* ratio for SC implementation of the BDFRM, the secondary voltage should be calculated in a flux-oriented reference frame as in (3.1),

$$\underline{u}_s = R_s \underline{i}_s + j\omega_s \lambda_s = R_s \underline{i}_s + j\omega_s (\sigma L_s \underline{i}_s + \underline{\lambda}_{ps}) \tag{3.1}$$

When maximum torque per inverter Ampere (MTPIA) is required, then $i_{sd} = 0$, resulting in (3.1) to become:

$$\underline{u}_s = j(R_s i_{sq} + \omega_s \lambda_{ps}) - \sigma \omega_s L_s i_{sq} . \tag{3.2}$$

For large scale machines, the winding resistances are low, and by neglecting the secondary impedance voltage drop, which can be proven to be a valid assumption for frequencies near synchronous speed, the expression for the secondary winding voltage can be simplified as follows:

$$\underline{u}_s \approx j\omega_s \lambda_{ps} \approx j\omega_s \frac{L_{ps}}{L_p} \lambda_p \approx j\omega_s \frac{L_{ps}}{L_p} \frac{u_p}{\omega_p} \tag{3.3}$$

The secondary voltage reference for a given primary voltage then can be determined as:

$$u_s^* \cong \omega_s^* \frac{L_{ps}}{L_p} \frac{u_p}{\omega_p} \tag{3.4}$$

Figure 3.1 shows a closed-loop scalar control method for the BDFRM.
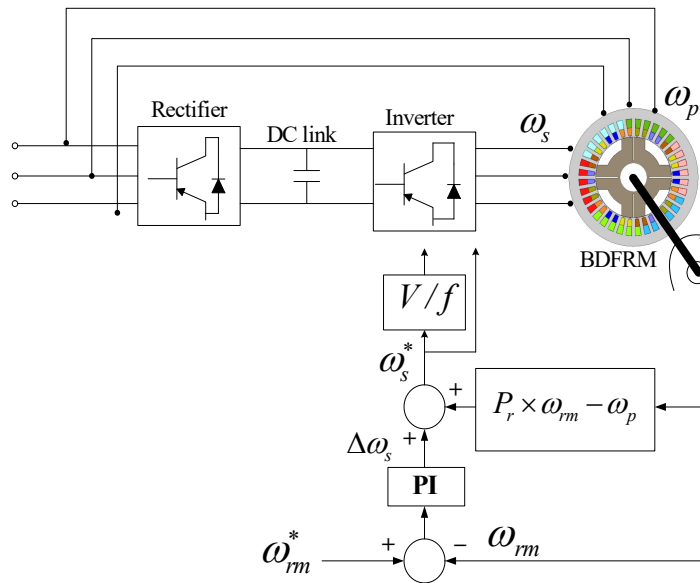
Figure 3.1. A block diagram of the BDFRM drive with closed-loop scalar control

3.3 **Vector Control**

Vector control (VC) algorithm is considered the common algorithm to control traditional machines, especially when a fast dynamic response and accurate control is required [90]. Furthermore, applying VC allows decoupled control of active and reactive power produced by the machine. DFIG systems have been conventionally controlled using either voltage-oriented [91], [92] or flux-oriented [10], [93] control based on *d-q* decoupling.

The power relations for primary VOC and PFOC for BDFRG can be derived from the BDFRG model (2.14) and (2.15) in ω_p and ω_s frames. Substituting for i_p from the λ_p equation of (2.16) and (2.17) into $s_p = \frac{3}{2} \underline{u}_p \underline{i}_p^*$, the following relationships are obtained [35]:

$$\left. \begin{array}{l} p_{P_{\text{VOC}}} = \dfrac{3\omega_p}{2} (\lambda_{ps_d} i_{sq} - \lambda_{ps_q} i_{sd}) \\[3mm] q_{P_{\text{VOC}}} = \dfrac{3\omega_p}{2} (\dfrac{\lambda_p^2}{L_p} - \lambda_{ps_d} i_{sd} - \lambda_{ps_q} i_{sq}) \end{array} \right\}, \tag{3.5}$$

There are coupling terms that can be observed from the VOC expressions, since i_{sd} and i_{sq} exist in both active and reactive power relationships of (3.5). The degree of coupling can be reduced by aligning the q_p-axis to the primary voltage vector as shown in Figure 3.2(a). In this case λ_p would be phase shifted ahead of the corresponding d_p-axis, depending on the winding resistance which is generally smaller in large machines and can be neglected.

$$
\left. \begin{array}{l}
p_{p_{FOC}} = \dfrac{3\omega_p}{2} \lambda_{ps_d} i_{sq} \\[4mm]
q_{p_{FOC}} = \dfrac{3\omega_p}{2} \left(\dfrac{\lambda_p^2}{L_p} - \lambda_{ps_d} i_{sd} \right) = \dfrac{3\omega_p}{2} \lambda_p i_{pd}
\end{array} \right\}
\tag{3.6}
$$

The PFOC is achieved if the d_p-axis is aligned to primary flux linkage (i.e. $\lambda_{pq} = 0$), as shown in Figure 3.2(b). The most important advantage of FOC over VOC is the inherently decoupled control of the primary active and reactive power. However, these valuable FOC properties come at the cost of the flux angle estimation. Furthermore, the winding resistance (R_p) knowledge is required, especially in low to medium power applications [35].

- (a) Voltage oriented control
- (b) Flux oriented control
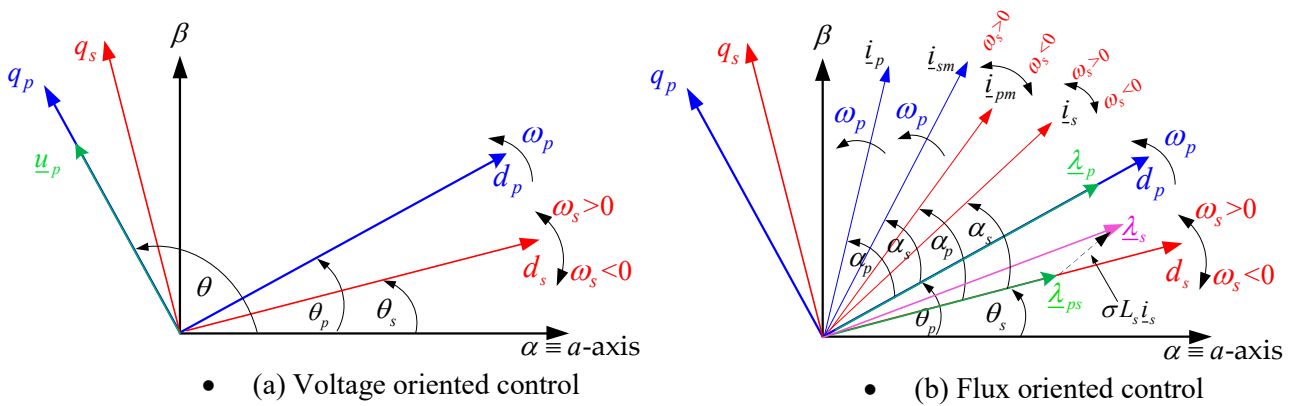
Figure 3.2. Phasor diagram and reference frames used in the BDFRM equations

3.3.1 Machine Side Vector Control (MSVC)

The MSVC scheme is shown in Figure 3.3, including both the inner and external control loops. The external control loop requires two PI controllers in order to control the primary active and reactive power independently. Likewise the inner one requires two PI controllers, but to regulate the d and q secondary current components.

Since the system is symmetrical (i.e. the transfer function is the same for d and q secondary current, as well as for the active and reactive power), the parameters of PI controllers are the same for the d-axis and q-axis secondary current loops, as well as for the reactive and active power loops.
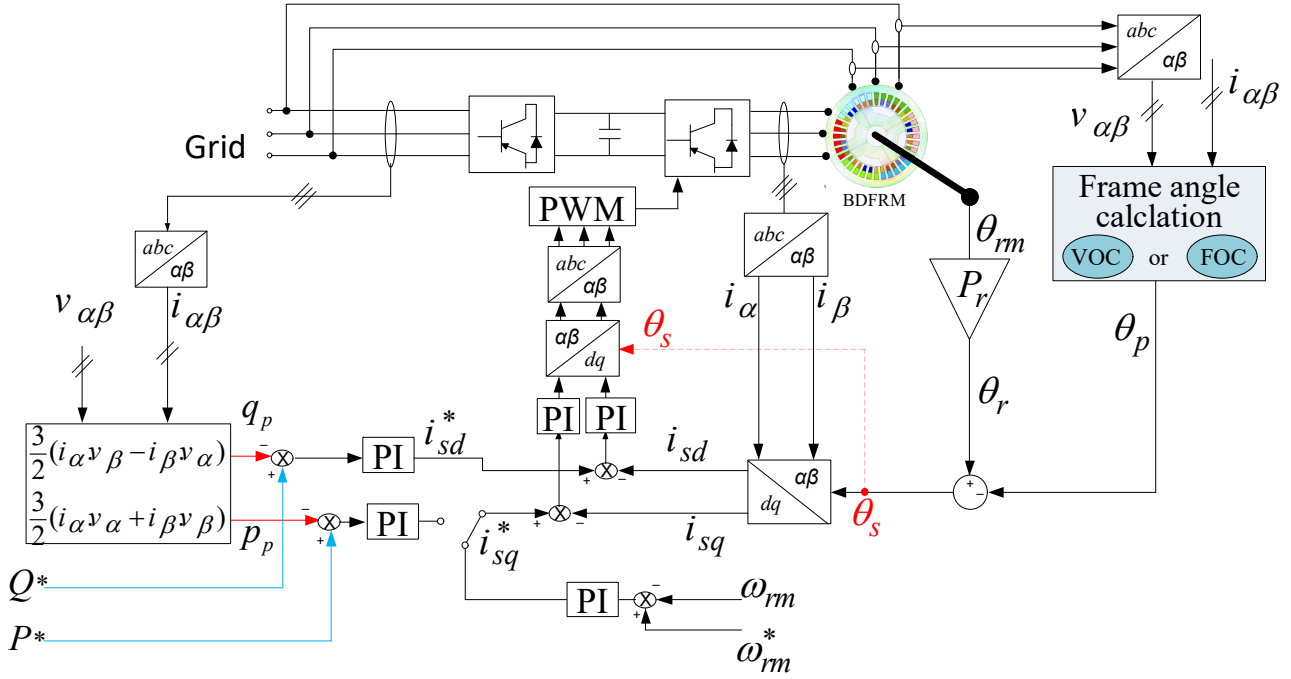
Figure 3.3. Configuration of the VC for a BDFRM machine side converter

3.3.1.1 Inner Loop (Currents Loop)

According to the BDFRM steady-state model, the secondary *d-q* voltages can be identified as:

$$\left. \begin{array}{l} u_{sd} = R_s i_{sd} + \omega_s(\sigma L_s i_{sd} + \lambda_{ps_d}) \\ u_{sq} = R_s i_{sq} + \omega_s(\sigma L_s i_{sq} + \lambda_{ps_q}) \end{array} \right\} \tag{3.7}$$

Equation (3.7) is important for the VC algorithm and can be used to calculate the reference voltage values. Since the flux linkage component is fairly constant, the use of PI current controllers is justified for this purpose and can be formulated as in [94]:

$$\left. \begin{array}{l} u^*_{sd} = PI(i^*_{sd} - i_{sd}) \\ u^*_{sq} = PI(i^*_{sq} - i_{sq}) \end{array} \right\} \tag{3.8}$$

The current control loop is shown in Figure 3.4 , and hence the corresponding transfer function can be written as follows:

$$\frac{i_{s_{dq}}(s)}{i^*_{s\,dq}(s)} = \frac{\dfrac{k_P}{\sigma L_s}s + \dfrac{k_I}{\sigma L_s}}{s^2 + \dfrac{R_s + k_P}{\sigma L_s}s + \dfrac{k_I}{\sigma L_s}} \tag{3.9}$$

where, (*) denotes the reference values
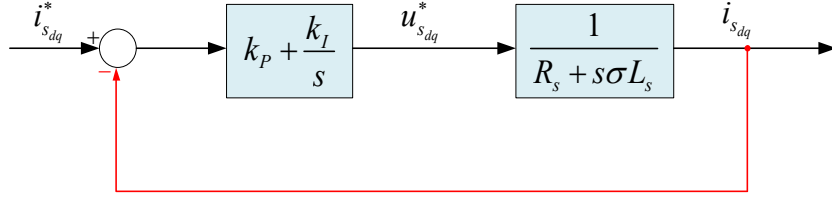
Figure 3.4. Current control loop of the secondary-side power converter.

Assuming $k_P << k_I$, (3.9) can be simplified as a second-order transfer function of the following form:

$$\frac{i_{s_{dq}}(s)}{i^*_{s_{dq}}(s)} = \frac{\dfrac{k_I}{\sigma L_s}}{s^2 + \dfrac{R_s + k_P}{\sigma L_s}.s + \dfrac{k_I}{\sigma L_s}} = \frac{\omega_n^2}{s^2 + 2\xi.\omega_n s + \omega_n^2}, \qquad (3.10)$$

where ξ is the damping ratio, which affects the maximum overshoot and response speed. An optimum damping ratio for classical second-order system is typically considered as 0.707, since it gives a very small overshoot (less than 5%) with an acceptable settling time. On the other hand, the undamped natural frequency ω_n affects the response speed. Hence, the PI controller parameters can be determined as in (3.11) [95],

$$k_P = (2\xi\omega_n\sigma L_s - R_s) \qquad , \qquad k_I = \omega_n^2\sigma L_s. \qquad (3.11)$$

3.3.1.2 Power Loop Derivation

In the case of VOC, the q_p-axis of the reference frame is aligned to the primary voltage vector as presented in Figure 3.2(a). Hence, the flux vector λ_p would be phase shifted ahead of the d_p-axis, depending on the winding resistance, which is typically smaller as the machine is larger. Therefore, VC could be similar to FOC as $\lambda_{ps_d} >> \lambda_{ps_q}$, i.e. $\lambda_{ps_d} \approx \lambda_{ps}$ and (3.5) becomes:

$$\left.\begin{array}{l} p_{p_{VOC}} \approx p_{p_{FOC}} = \dfrac{3\omega_p}{2}\lambda_{ps_d}i_{sq} \\[3mm] q_{p_{VOC}} \approx q_{p_{FOC}} = \dfrac{3\omega_p}{2}(\dfrac{\lambda_p^2}{L_p} - \lambda_{ps_d}i_{sd}) = \dfrac{3\omega_p}{2}\lambda_p i_{pd} \end{array}\right\} \qquad (3.12)$$

Since the primary winding is grid connected at line frequency, the magnitudes of λ_p and λ_{ps} are approximately constant. According to (3.12), p_p and q_p are proportional to i_{sq} and i_{sd} currents respectively, which means that the use of PI controllers is correct:

$$\left.\begin{array}{l} i^*_{sd} = PI(q^*_P - q_P) \\[2mm] i^*_{sq} = PI(p^*_P - p_P) \end{array}\right\} \qquad (3.13)$$

Because the inner control loops are much faster than the external control loops, the power converter dynamics and measurement delays would be neglected, as shown in Figure 3.5.
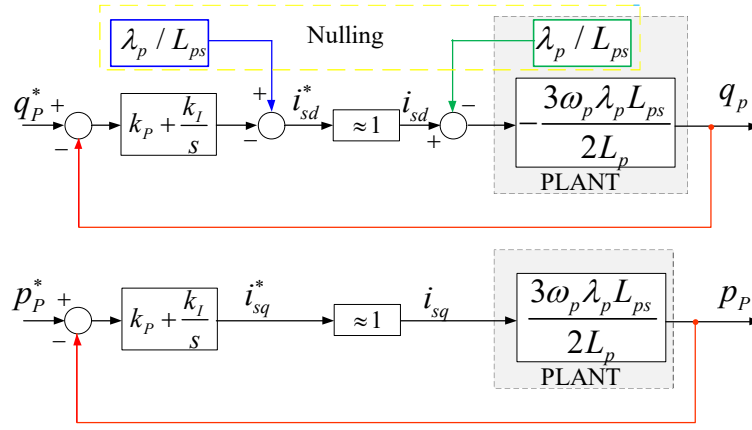
Figure 3.5. Power control loops of the secondary-side power converter

Transfer functions for the active and reactive power are the same and can be expressed as:

$$\frac{q_p^*}{q_p} = \frac{p_p^*}{p_p} = \frac{As+1}{(\frac{1}{Bk_I}+A)s+1},$$ (3.14)

where: $A = \dfrac{k_P}{k_I}$, $B = \dfrac{3}{2}U_p\dfrac{L_{ps}}{L_p}$

Assuming that ratio A is the dominant term in the denominator (i.e. $A \approx A + 1/Bk_I$), then the transfer function can be approximated as a unity gain with a poor noise rejection property. Thus, A should be very small in order to use a first order approximation of the transfer function and to determine the PI gains as follows:

$$\frac{p_p^*}{p_p} = \frac{q_p^*}{q_p} = \frac{As+1}{(\frac{1}{Bk_I}+A)s+1} \approx \frac{1}{\tau_o s + 1},$$ (3.15)

$$k_I = \frac{1}{B(\tau_o - A)} \quad , \quad k_P = Ak_I,$$ (3.16)

where τ_o is the external loop time constant and should be much larger than the inner loop time constant.

3.3.1.3 Speed Loop in Vector Control

Vector control is commonly used in the most electrical drive applications owing to the high quality response provided at fixed sampling rates. The inner loop is to control the secondary dq current components, while the external one corresponds to the speed control. In this case, the actual machine rotation is torque based. From equation (2.25) and by aligning the d_p-axis of the reference frame to the primary flux vector (i.e. $\lambda_{pq}=0$), the torque expression can be simplified as:

$$T_e = \frac{3}{2}\frac{P_r L_{ps}}{L_p}\lambda_p i_{sq} \tag{3.17}$$

The appropriate torque is developed as illustrated in Figure 3.6.
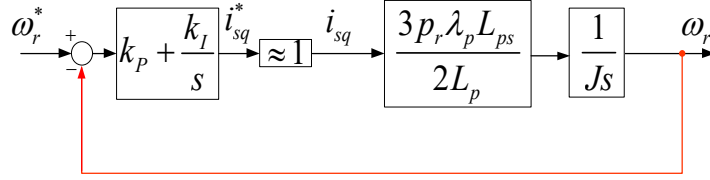
Figure 3.6. Speed control loop of the secondary-side converter

The corresponding transfer function for the speed control loop can be written as follows:

$$\frac{\omega_r}{\omega_r^*} = \frac{k_P m s + k_I m}{s^2 + k_P m s + k_I m} \tag{3.18}$$

where $m=3P_r L_{ps}\lambda_p/(2L_p\, J)$. Assuming $k_P \ll k_I$, equation (3.18) can be approximated as a second-order transfer function, and the controller gains can then be calculated as follows:

$$\frac{\omega_r}{\omega_r^*} = \frac{k_I m}{s^2 + k_P m s + k_I m} = \frac{\omega_n^2}{s^2 + 2\xi\omega_n s + \omega_n^2}\,, \tag{3.19}$$

$$k_P = \frac{2\xi\omega_n}{m}\quad,\quad k_I = \frac{\omega_n^2}{m} \tag{3.20}$$

3.3.2 Vector Control of Grid Side Converter (GSC)

The main objective of the GSC is to maintain the DC-link voltage between the two converters at a desired value and to regulate the reactive power exchange between the GSC and the grid. The power factor of the GSC is usually set to unity ($q_g=0$). However, it can be used to inject reactive power into the grid during the grid fault for voltage support [96].

The VOC is selected for the GSC by aligning the *d*-axis of the rotating frame with the grid voltage space vector ($u_{gq}=0$). In this case the grid active and reactive power equations can be simplified as in (3.21):

$$\begin{cases} p_g = \dfrac{3}{2}u_g i_{g_d} \\[2mm] q_g = -\dfrac{3}{2}u_g i_{g_q} \end{cases} \tag{3.21}$$

It is clear that i_{gd} current is responsible for the active power, while the i_{gq} current is responsible for controlling the reactive power.

Similar to the machine side converter, the control part of the GSC includes two inner and one external control loop as shown in Figure 3.7.
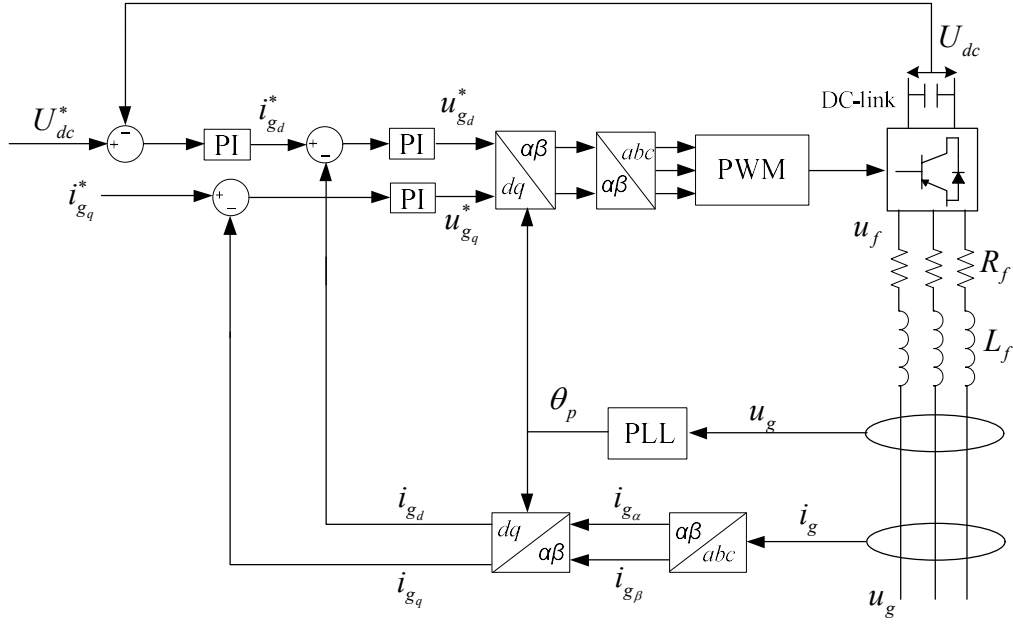
Figure 3.7. Control scheme of the grid side converter

3.3.2.1 Mathematical Model of the Current Loops

The voltage balance across the grid filter in the synchronous *dq* reference frame rotating at ω_p is given by (3.21),

$$\begin{cases} u_{g_d} - u_{f_d} = (R_f + L_f)i_{gd} - \omega_p L_f i_{g_q} \\ u_{g_q} - u_{f_q} = (R_f + L_f)i_{gq} + \omega_p L_f i_{g_d} \end{cases}, \tag{3.22}$$

where R_f and L_f are respectively the resistance and inductance of the grid side filter, $u_{gd,q}$ and $i_{gd,q}$ are the *dq* components of the grid voltage and current respectively, $u_{fd,q}$ and $i_{fd,q}$ are the *dq* components of the grid filter voltage and current respectively.

The grid-side converter inner control loop shown in Figure 3.8 has the following transfer function:

$$\frac{i_{g_{dq}}}{i_{g_{dq}}^*} = \frac{\dfrac{k_P}{L_f}s + \dfrac{k_I}{L_f}}{s^2 + (\dfrac{R_f + k_P}{L_f})s + \dfrac{k_I}{L_f}} \approx \frac{\omega_n^2}{s^2 + 2\xi\omega_n s + \omega_n^2} \tag{3.23}$$

The PI controller gains can be calculated as follows:

$$\begin{cases} k_p = (2\xi\omega_n L_f - R_f) \\ k_I = \omega_n^2 L_f \end{cases} \tag{3.24}$$
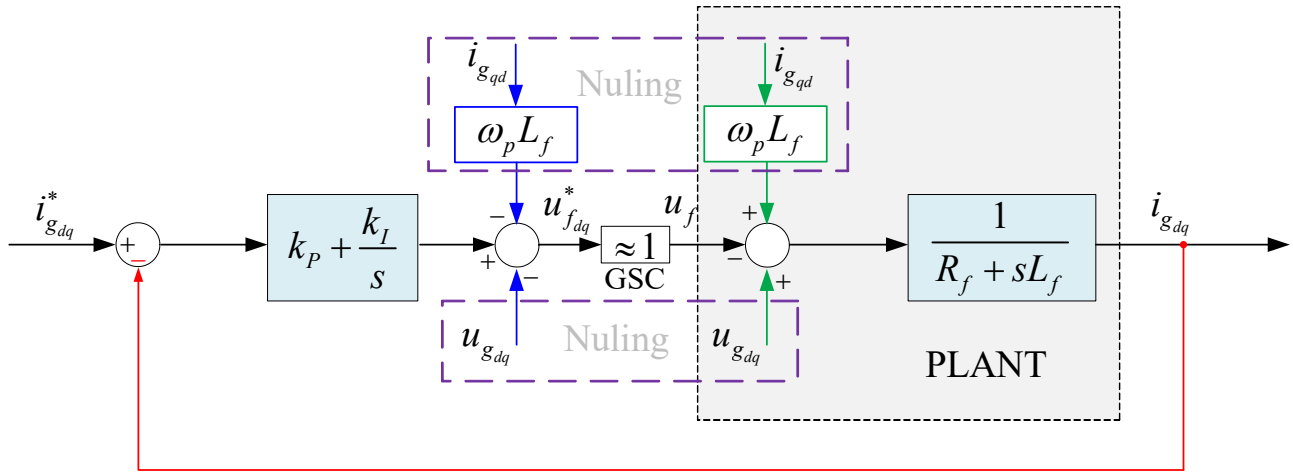
Figure 3.8. Current control loops of the grid-side converter

3.4 Sensorless Torque and Reactive Power Controller for BDFRM

The basic concept of the DTC control can be established from the torque expression defined with (3.25), because it shows the relationship between the electromagnetic torque, the secondary flux (λ_s), the mutual flux (λ_{ps}), and the angle (δ) between the corresponding phasors [97, 98]:

$$T_e = \frac{3P_r}{2\sigma L_s}\left|\underline{\lambda}_{ps} \times \underline{\lambda}_s\right| = \frac{3P_r}{2\sigma L_s}\underbrace{\frac{L_{ps}}{L_p}\lambda_p}_{\lambda_{ps}}\lambda_s \sin\delta \tag{3.25}$$

It is worth mentioning that both of (λ_s) and (λ_{ps}) vectors rotate at ω_s as illustrated in Figure 3.9.
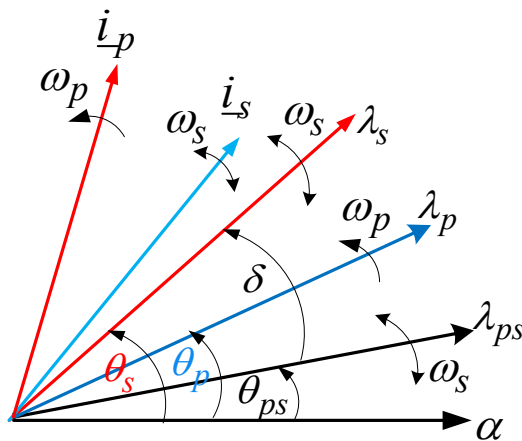
Figure 3.9. Phasor diagram in a stationary reference frame

In addition, the secondary flux vector (λ_s) is ahead of the mutual flux vector (λ_{ps}) for motoring operation, and vice versa in the generating regime as shown in Figure 3.10.
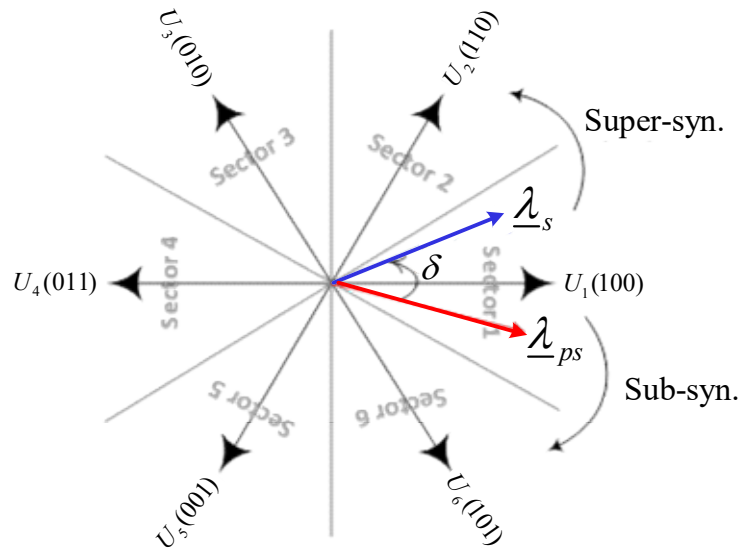
Figure 3.10. Flux vectors characteristics and secondary voltage vectors in associated π/3 sectors

To better understand the mechanism by which the λ_s dynamics affect the instantaneous torque and primary reactive power, two extreme scenarios are inspected under the PFOC conditions (i.e. $\lambda_p = \lambda_{pd}$ and $\lambda_{ps} = \lambda_{psd}$), as in (3.12):

$$q_p = \frac{3\omega_p \lambda_p}{2L_p}(\lambda_p - \lambda_{ps_d} i_{sd}) \tag{3.26}$$

Let us assume that the machine magnetization is completely performed from the primary side ($i_{sd} = 0$) and i_{sq} is to be changed from zero to its rated value. The λ_s behavior can be observed from (3.27) and Figure 3.2(b). It reveals a predominant change of $\lambda_{sq} = \sigma L_s i_{sq} = \lambda_s \sin \delta$ and, therefore, δ in (3.25) with $\lambda_s \approx \lambda_{sd} = \lambda_{ps} \approx$ const is being unaffected.

$$\underline{\lambda}_s = \overbrace{\sigma L_s i_{sd} + \lambda_{ps_d}}^{\lambda_{sd}} + j(\overbrace{\sigma L_s i_{sq} + \lambda_{ps_q}}^{\lambda_{sq}}). \tag{3.27}$$

Hence, increase/decrease in δ resulting in increase/decrease of torque according to (3.25). On the other hand, moving λ_s in a desired direction (i.e. δ change) would not affect q_p much according to (3.26).

Contrarily, if the unloaded machine is considered (i.e. $i_{sq}= 0$) and i_{sd} is changed from zero to its rated value, it will result in $\lambda_{sq} = 0$ and $\lambda_s = \lambda_{sd} = \lambda_{ps} + \sigma L_s i_{sd}$. Therefore, variations in i_{sd} would have a significant effect on λ_s and hence on q_p (but in opposite direction) according to (3.26). In contrast to this, it has a marginal influence on δ and consequently on T_e.

In conclusion, if q_p is required to be increased/decreased, i_{sd} and, consequently, λ_s must be decreased/increased [39, 46, 98].

A structural diagram of the control scheme is shown in Figure 3.11. The reactive power reference (q^*) is set to achieve the required line power factor, whereas the specific torque reference T_e^* is commonly generated by a conventional PI speed controller (in drive applications) or a MPPT controller (e.g. in variable speed WECS) [39, 46].
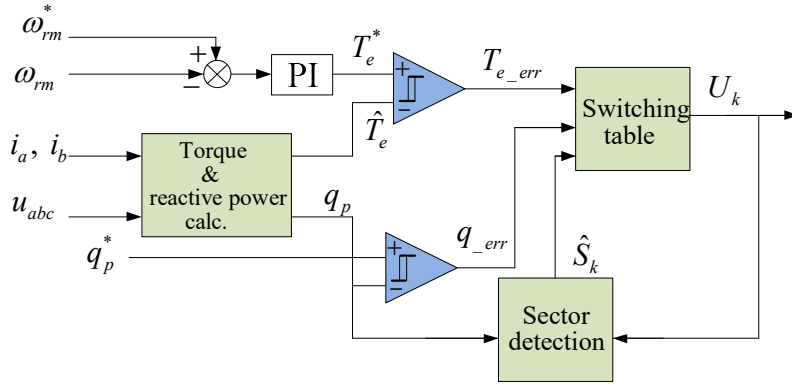
Figure 3.11. Structure of the torque and reactive power control

The primary phase measurements are used to calculate the estimated value of torque and the actual reactive power as in (3.28),

$$
\left.\begin{aligned}
\hat{T}_e &= \frac{3}{2} P_r \left(\hat{\lambda}_{p_d} i_{p_q} - \hat{\lambda}_{p_q} i_{p_d} \right) \\
q_p &= \frac{3}{2} \left(u_{p_q} i_{p_d} - u_{p_d} i_{p_q} \right)
\end{aligned}\right\}
\tag{3.28}
$$

where $\hat{\lambda}_{dq}$ are estimated using

$$
\underline{\hat{\lambda}}_p = \overbrace{\int (u_{p_d} - R i_{p_d}) dt}^{\hat{\lambda}_{p_d}} + j \overbrace{\int (u_{p_q} - R i_{p_q}) dt}^{\hat{\lambda}_{p_q}}
\tag{3.29}
$$

The comparators' outputs (T_{e_err} and $q_{\_err}$), along with information about the secondary flux sector, can be used to index the relevant look-up tables and determine the appropriate voltage vector that should be applied to the secondary terminals at any given time.

3.4.1 Voltage vectors and their effects

Considering anti clockwise direction of rotation to be positive, note that λ_s is ahead of λ_{ps} in motoring mode of operation (as in Figure 3.10) and λ_s is behind λ_{ps} in generating mode.

According to (2.12), λ_s and λ_{ps} rotate clockwise at sub-synchronous speeds when $\omega_s< 0$, remain stationary at the synchronous speed ($\omega_s = 0$), and start rotating in the negative direction at super-synchronous speeds when $\omega_s > 0$. It is noteworthy that by analogy to the DTC case, only the non-zero switching vectors are used to avoid the speed dependence of the torque controller induced by paradoxical influences of the same zero vectors at super- and sub-synchronous speeds [99].

Obviously, influences of a particular secondary voltage vector shown in Figure 3.10 on the dynamic performance of the machine depend on the position of λ_s at a given time instant. Let us assume that λ_s is located in sector 1 as shown in Figure 3.10 and that the BDFRM is operated as a motor, then either U_2 or U_3 would move λ_s anti-clockwise (positive phase shift) increasing both the angle δ and instantaneous torque (T_e), as presented in (3.25). On the other hand, U_5 or U_6 would move λ_s clockwise resulting in the δ and T_e to decrease. In summary, one can conclude that If λ_s lies

in the k_{th} sector, then the application of voltage vectors U_{k+1} or U_{k+2} would increase torque, while U_{k-1} or U_{k-2} would decrease it [39].

It is obvious from Figure 3.10, that the vectors U_1, U_2 or U_6 will increase the values of $\lambda_{sd} \approx \lambda_s$, which will in turn increase the reactive power contributed by the inverter. This means reduction in the q_p required to establish the machine flux. In contrast to this, any of U_3, U_4 or U_5 will have an opposite effects (i.e. will decrease λ_{sd}), which will in turn increase the amount of q_p to be taken from the grid.

In summary, it can be therefore said that if the secondary flux vector is located in the k_{th} sector, then the voltage vectors U_k, U_{k+1} or U_{k-1} will reduce q_p, while U_{k+2}, U_{k+3} or U_{k-2} will increase q_p.

The switching table for active voltage vector selection is shown in Table 3.1 in accordance to negative and positive torque and reactive power deviations. This switching strategy ensures that T_e and q_p are controlled within the hysteresis bands $(T_e^* \pm \Delta T, q_p^* \pm \Delta q_p)$.

Table 3.1. Selection of active switching states

Deviations		Sector					
T_{e_err}	q_{p_err}	1	2	3	4	5	6
$> \Delta T_e$	$> \Delta q_p$	U_3	U_4	U_5	U_6	U_1	U_2
$> \Delta T_e$	$\leq -\Delta q_p$	U_2	U_3	U_4	U_5	U_6	U_1
$\leq -\Delta T_e$	$> \Delta q_p$	U_5	U_6	U_1	U_2	U_3	U_4
$\leq -\Delta T_e$	$\leq -\Delta q_p$	U_6	U_1	U_2	U_3	U_4	U_5

Chapter 4

Modeling and Control of BDFRG under Unbalanced Grid Conditions

4.1 **Introduction**

Most of the wind turbines are connected to weak grids where unbalanced-load distributions are usually not corrected. A major cause of an unbalanced voltage is typically unsymmetrical loads that are applied to all three phases (i.e. the loads are not symmetrically distributed among the three phases). Unbalanced voltage problems also appear in large public power systems where single-phase lighting loads are common in large commercial facilities [55]. Furthermore, an unbalanced-voltage may also occur due to unequal transformer windings or transmission impedance, and many other causes [100].

Presence of negative-sequence components in the grid voltage poses serious problems to wind generators including unbalanced primary currents, current harmonics at the secondary side, unequal heating or hot spots in the windings [58] which degrade the insulation and reduce windings life expectancy [59, 101]. The interaction between negative-sequence voltage and positive-sequence current also cause power and torque pulsations, which may cause extra mechanical stress on the drive train and gearbox [60-62] and increase acoustic noise, too. Hence, studying the performance of wind generators under UGVCs and designing a suitable control algorithm are very important tasks.

This chapter presents the main aspects, mathematical model of a BDFRG under UGVCs and the advanced vector control strategy developed for UGVCs. An extended vector control algorithm is used to control both the positive and negative sequence components of the secondary currents independently. The model of the machine under unbalanced primary voltage is developed in the positive and negative synchronous reference frames, and then used to derive the control form relationships between torque, active and reactive power, including positive and negative components.

4.2 **Mathematical Model of BDFRM under Unbalanced Grid Voltage Conditions**

Every non-symmetrical three-phase system can be represented by three symmetrical three-phase systems: direct, inverse, and zero sequence system. Due to the isolated neutral point of the BDFRG winding, the zero system voltage does not affect the performance of the BDFRG. Hence, any vector can be represented as the sum of the positive and negative components [55, 61, 102] as shown in Figure 4.1.

In the case of unbalanced grid voltages, all primary variables (voltages, currents, and fluxes) can be represented in a stationary ($\alpha\beta$) reference frame as follows:

$$\underline{F}_{p_s} = F_{p_1}e^{j(\omega_p t + \phi_{Fp}^+)} + F_{p_2}e^{j(-\omega_p t + \phi_{Fp}^-)}, \tag{4.1}$$

where F_{p1} and F_{p2} are the modules of the positive and negative sequences respectively, while ϕ^+_{Fp} and ϕ^-_{Fp} are their initial angular positions. Transforming (4.1) into the primary reference frame (by multiplying with $e^{-j\omega pt}$) leads to:

$$\underline{F}_p = F_{p_1}e^{j\phi_{Fp}^+} + F_{p_2}e^{j\phi_{Fp}^-}e^{-j2\omega_p t} = \underline{F}_p^+ + \underline{F}_p^-e^{-j2\omega_p t}, \tag{4.2}$$

where F^+_p and F^-_p are the positive and negative sequence components of F_p in the respective positive and negative reference frames rotating at ω_p and $-\omega_p$, respectively.

In the same manner, any secondary winding variable represented in the space vector form in the $\alpha\beta$ reference frame under unbalanced grid voltage conditions can be expressed as:

$$\underline{F}_{s_s} = F_{s_1} e^{j((\omega_r - \omega_p)t + \phi^+_{Fs})} + F_{s_2} e^{j((\omega_r + \omega_p)t + \phi^-_{Fs})} , \qquad (4.3)$$

where F_{s1} and F_{s2} are the modules of the positive and negative sequences, respectively, and ϕ^+_{Fs} and ϕ^-_{Fs} are their initial angular positions.
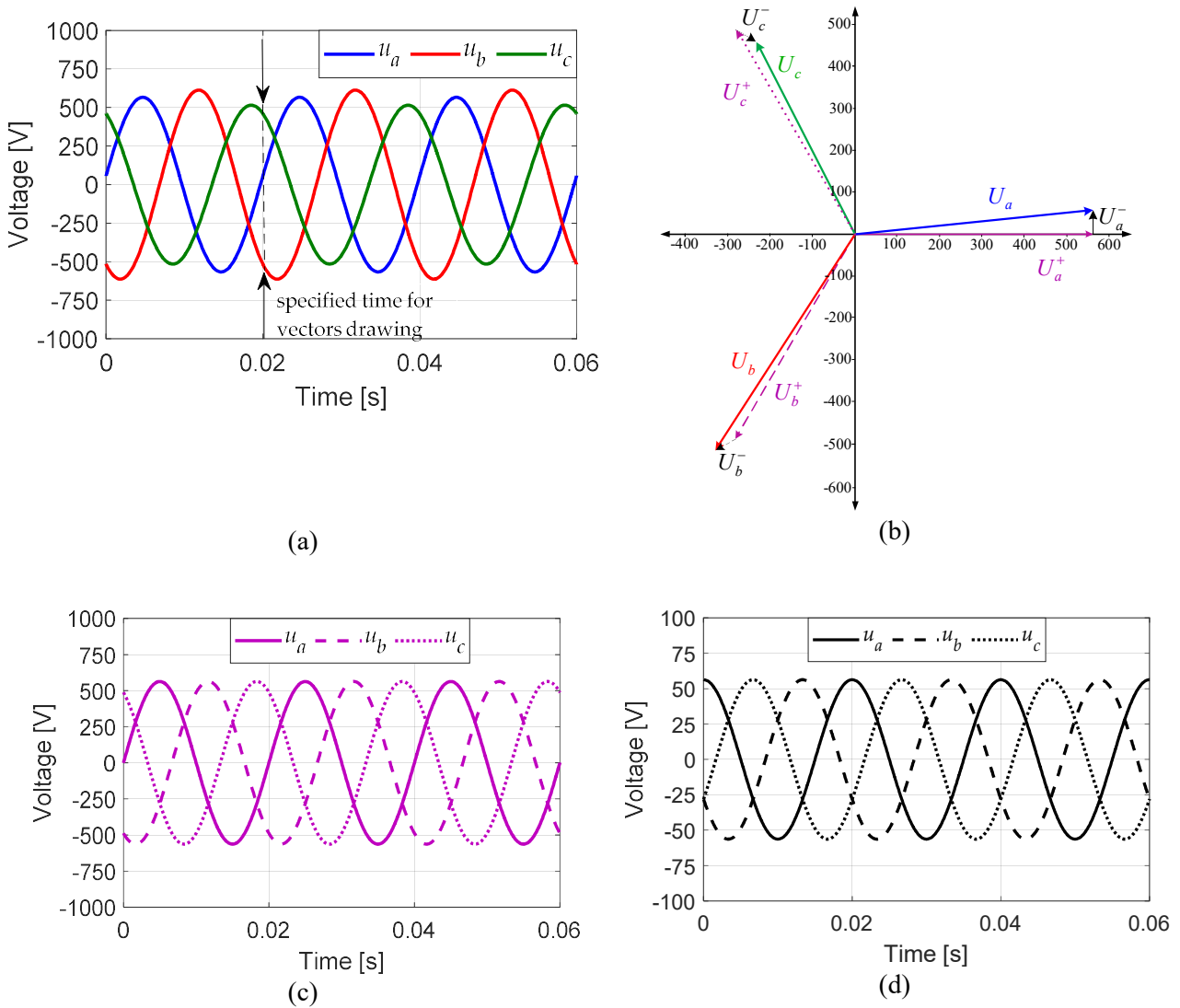
Figure 4.1. (a) Three-phase unbalanced voltage instantaneous values with 10% Voltage Unbalance Factor (VUF) (b) three phase vector diagram of the distorted waveform (c) positive sequence, and (d) negative sequence. Negative sequence voltage magnitudes are 10% of positive counterparts at the same frequency.

By multiplying equation (4.3) with $e^{-j\omega st}$, this equation will be transformed into the secondary reference frame:

$$\underline{F}_s = F_{s1}e^{j\phi_{Fs}^+} + F_{s_2}e^{j\phi_{Fs}^-}e^{j2\omega_p t} = \underline{F}_s^+ + \underline{F}_s^- e^{j2\omega_p t}, \tag{4.4}$$

where F_s^+ and F_s^- are the positive and negative sequence components in the respective positive and negative reference frames rotating at $(\omega_r - \omega_p)$ and $(\omega_r + \omega_p)$, respectively as illustrated in Figure 4.2.
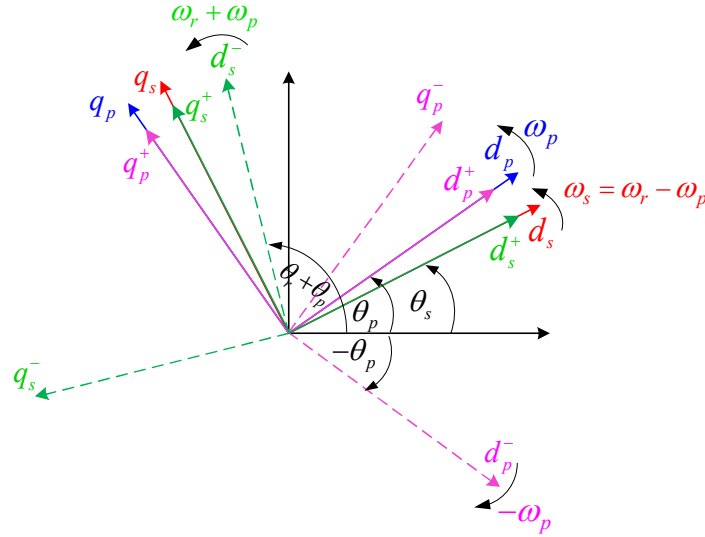
Figure 4.2. The reference frames used for the BDFRG model under unbalanced conditions

It is worth noting that the positive sequence equations are similar to the space vector model under balanced conditions given by (2.19) and (2.20) [61]:

$$\begin{cases} \underline{u}_p^+ = R_p \underline{i}_p^+ + \dfrac{d\underline{\lambda}_p^+}{dt} + j\omega_p \underline{\lambda}_p^+ \\[2mm] \underline{u}_s^+ = R_s \underline{i}_s^+ + \dfrac{d\underline{\lambda}_s^+}{dt} + j(\omega_r - \omega_p)\underline{\lambda}_s^+ \end{cases}, \tag{4.5}$$

where

$$\begin{cases} \underline{\lambda}_p^+ = L_p \underline{i}_p^+ + L_{ps} \underline{i}_s^{+*} \\[2mm] \underline{\lambda}_s^+ = L_s \underline{i}_s^+ + L_{ps} \underline{i}_p^{+*} \end{cases} \tag{4.6}$$

Likewise, the negative sequence model can be obtained as follows:

$$\begin{cases} \underline{u}_p^- = R_p \underline{i}_p^- + \dfrac{d\underline{\lambda}_p^-}{dt} - j\omega_p \underline{\lambda}_p^- \\[2mm] \underline{u}_s^- = R_s \underline{i}_s^- + \dfrac{d\underline{\lambda}_s^-}{dt} + j(\omega_r + \omega_p)\underline{\lambda}_s^- \end{cases}, \tag{4.7}$$

where

$$\begin{cases} \underline{\lambda}_p^- = L_p \underline{i}_p^- + L_{ps} \underline{i}_s^{-*} \\ \underline{\lambda}_s^- = L_s \underline{i}_s^- + L_{ps} \underline{i}_p^{-*} \end{cases} \tag{4.8}$$

Using the aforementioned space vector equations, the *dq* equations for the positive sequence can be derived as follows:

$$\left.\begin{aligned} u_{pd}^+ &= R_p i_{pd}^+ + \frac{d\lambda_{pd}^+}{dt} - \omega_p \lambda_{pq}^+ \\ u_{pq}^+ &= R_p i_{pq}^+ + \frac{d\lambda_{pq}^+}{dt} + \omega_p \lambda_{pd}^+ \end{aligned}\right\}, \tag{4.9}$$

$$\left.\begin{aligned} u_{sd}^+ &= R_s i_{sd}^+ + \frac{d\lambda_{sd}^+}{dt} - (\omega_r - \omega_p)\lambda_{sq}^+ \\ u_{sq}^+ &= R_s i_{sq}^+ + \frac{d\lambda_{sq}^+}{dt} + (\omega_r - \omega_p)\lambda_{sd}^+ \end{aligned}\right\}, \tag{4.10}$$

where the fluxes are expressed as follows:

$$\left.\begin{aligned} \lambda_{pd}^+ &= L_p i_{pd}^+ + L_{ps} i_{sd}^+ \\ \lambda_{pq}^+ &= L_p i_{pq}^+ - L_{ps} i_{sq}^+ \end{aligned}\right\}, \tag{4.11}$$

$$\left.\begin{aligned} \lambda_{sd}^+ &= L_s i_{sd}^+ + L_{ps} i_{pd}^+ \\ \lambda_{sq}^+ &= L_s i_{sq}^+ - L_{ps} i_{pq}^+ \end{aligned}\right\} \tag{4.12}$$

Likewise, the negative sequence *dq* equations can be obtained as follows:

$$\left.\begin{aligned} u_{pd}^- &= R_p i_{pd}^- + \frac{d\lambda_{pd}^-}{dt} + \omega_p \lambda_{pq}^- \\ u_{pq}^- &= R_p i_{pq}^- + \frac{d\lambda_{pq}^-}{dt} - \omega_p \lambda_{pd}^- \end{aligned}\right\}, \tag{4.13}$$

$$\left.\begin{aligned} u_{sd}^- &= R_s i_{sd}^- + \frac{d\lambda_{sd}^-}{dt} - (\omega_r + \omega_p)\lambda_{sq}^- \\ u_{sq}^- &= R_s i_{sq}^- + \frac{d\lambda_{sq}^-}{dt} + (\omega_r + \omega_p)\lambda_{sd}^- \end{aligned}\right\}, \tag{4.14}$$

and

$$\left.\begin{aligned} \lambda_{pd}^- &= L_p i_{pd}^- + L_{ps} i_{sd}^- \\ \lambda_{pq}^- &= L_p i_{pq}^- - L_{ps} i_{sq}^- \end{aligned}\right\}, \tag{4.15}$$

$$\left.\begin{aligned} \lambda_{sd}^- &= L_s i_{sd}^- + L_{ps} i_{pd}^- \\ \lambda_{sq}^- &= L_s i_{sq}^- - L_{ps} i_{pq}^- \end{aligned}\right\} \tag{4.16}$$

4.2.1 Power and Torque Equations

The power and torque expressions can be derived by substituting the *dq* positive and negative components into the following general power and torque expressions [61]:

$$p_{p,s} = \frac{3}{2} \text{Re} \left\{ \underline{u}_{p,s} \underline{i}_{p,s}^* \right\} \\ q_{p,s} = \frac{3}{2} \text{Im} \left\{ \underline{u}_{p,s} \underline{i}_{p,s}^* \right\}, \tag{4.17}$$

$$T_e = j\frac{3}{4} P_r \left\{ \underline{\lambda}_p \underline{i}_p^* - \underline{\lambda}_p^* \underline{i}_p \right\}, \tag{4.18}$$

where $p_{p,s}$ and $q_{p,s}$ are the active and reactive powers for the primary and secondary windings respectively. The resulting powers and torque can be expressed as in [61, 103]:

$$p_p = P_{av} + P_1 \sin(2\omega_p t) + P_2 \cos(2\omega_p t) \\ q_p = Q_{av} + Q_1 \sin(2\omega_p t) + Q_2 \cos(2\omega_p t), \tag{4.19}$$

where

$$\begin{bmatrix} P_{av} \\ P_1 \\ P_2 \end{bmatrix} = \frac{3}{2L_p} \left(\begin{bmatrix} \lambda_{pd}^+ & \lambda_{pq}^+ & \lambda_{pd}^- & \lambda_{pq}^- \\ \lambda_{pq}^- & -\lambda_{pd}^- & -\lambda_{pq}^+ & \lambda_{pd}^+ \\ \lambda_{pd}^- & \lambda_{pq}^- & \lambda_{pd}^+ & \lambda_{pq}^+ \end{bmatrix} \begin{bmatrix} u_{pd}^+ \\ u_{pq}^+ \\ u_{pd}^- \\ u_{pq}^- \end{bmatrix} + L_{ps} \begin{bmatrix} -u_{pd}^+ & u_{pq}^+ & -u_{pd}^- & u_{pq}^- \\ -u_{pq}^+ & -u_{pd}^- & u_{pq}^+ & u_{pd}^+ \\ -u_{pd}^- & u_{pq}^- & -u_{pd}^+ & u_{pq}^+ \end{bmatrix} \begin{bmatrix} i_{sd}^+ \\ i_{sq}^+ \\ i_{sd}^- \\ i_{sq}^- \end{bmatrix} \right), \tag{4.20}$$

$$\begin{bmatrix} Q_{av} \\ Q_1 \\ Q_2 \end{bmatrix} = \frac{3}{2L_p} \left(\begin{bmatrix} -\lambda_{pq}^+ & \lambda_{pd}^+ & -\lambda_{pq}^- & \lambda_{pd}^- \\ \lambda_{pd}^- & \lambda_{pq}^- & -\lambda_{pd}^+ & -\lambda_{pq}^+ \\ -\lambda_{pq}^- & \lambda_{pd}^- & -\lambda_{pq}^+ & \lambda_{pd}^+ \end{bmatrix} \begin{bmatrix} u_{pd}^+ \\ u_{pq}^+ \\ u_{pd}^- \\ u_{pq}^- \end{bmatrix} + L_{ps} \begin{bmatrix} -u_{pq}^+ & -u_{pd}^+ & -u_{pq}^- & -u_{pd}^- \\ u_{pd}^- & -u_{pq}^- & -u_{pd}^+ & u_{pq}^+ \\ -u_{pq}^- & -u_{pd}^- & -u_{pq}^+ & -u_{pd}^+ \end{bmatrix} \begin{bmatrix} i_{sd}^+ \\ i_{sq}^+ \\ i_{sd}^- \\ i_{sq}^- \end{bmatrix} \right) \tag{4.21}$$

It can be observed from (4.19), (4.20) and (4.21) that there are DC components P_{av} and Q_{av}, together with the oscillating terms at twice the grid frequency, $P_1\sin(2\omega_p t)$, $P_2\cos(2\omega_p t)$ and $Q_1\sin(2\omega_p t)$, $Q_2\cos(2\omega_p t)$, which indicate the effect of negative sequence components.

The electromagnetic torque expression for the BDFRG under unbalanced conditions can be obtained by substituting (4.2) and $F=F_d+jF_q$ into (4.18), resulting with (4.22),

$$T_e = T_{av} + T_1 \sin(2\omega_p t) + T_2 \cos(2\omega_p t), \tag{4.22}$$

where

$$\begin{bmatrix} T_{av} \\ T_1 \\ T_2 \end{bmatrix} = \frac{3P_r L_{ps}}{2L_p} \begin{bmatrix} \lambda_{pq}^+ & \lambda_{pd}^+ & \lambda_{pq}^- & \lambda_{pd}^- \\ -\lambda_{pd}^- & \lambda_{pq}^- & \lambda_{pd}^+ & -\lambda_{pq}^+ \\ \lambda_{pq}^- & \lambda_{pd}^- & \lambda_{pq}^+ & \lambda_{pd}^+ \end{bmatrix} \begin{bmatrix} i_{sd}^+ \\ i_{sq}^+ \\ i_{sd}^- \\ i_{sq}^- \end{bmatrix} \tag{4.23}$$

Apart from the fundamental component T_{av}, there are two additional oscillating components at $2\omega_p$. One can conclude that the unbalanced grid voltage causes the appearance of pulsations in the power and torque waveforms.

4.3 Methods for Real-Time Separation of Positive and Negative Sequences

In order to obtain the positive and negative sequence components, the real-time separation of the positive and negative sequences is required. Furthermore, the effectiveness of the proposed control method highly relies on the accurate separation of positive and negative sequences in real-time.

Generally, there are four methods reported in the literature: analytically based method [61], "Signal delay cancellation" [4], and filtering methods, i.e. low-pass filters [4] and notch filters (band trap, band-stop) [67]. Any of these methods can be used for this purpose.

The first method, which is an analytically based method, derived on the fact that F^+_{pd}, F^+_{pq} and F^+_{sd}, F^+_{sq} represent the DC components of F_{pd}, F_{pq}, F_{sd} and F_{sq} because frequencies of F^+_p and F^+_s are respectively equal with the frequencies of dq_p and dq_s frames (i.e. F^+_{pd}, F^+_{pq} and F^+_{sd}, F^+_{sq} are the mean values of F_{pd}, F_{pq}, F_{sd} and F_{sq}).

The real and imaginary parts of (4.2) and (4.4) can be expressed as:

$$\left.\begin{array}{l} F_{pd} = F^+_{pd} + F^-_{pd}\cos(2\omega_p t) + F^-_{pq}\sin(2\omega_p t) \\ F_{pq} = F^+_{pq} + F^-_{pq}\cos(2\omega_p t) - F^-_{pd}\sin(2\omega_p t) \end{array}\right\}, \tag{4.24}$$

$$\left.\begin{array}{l} F_{sd} = F^+_{sd} + F^-_{sd}\cos(2\omega_p t) - F^-_{sq}\sin(2\omega_p t) \\ F_{sq} = F^+_{sq} + F^-_{sq}\cos(2\omega_p t) + F^-_{sd}\sin(2\omega_p t) \end{array}\right\}, \tag{4.25}$$

where F^+_{pd}, F^+_{pq} and F^+_{sd}, F^+_{sq} represent the DC components of F_{pd}, F_{pq}, F_{sd} and F_{sq}:

$$\left.\begin{array}{l} F^+_{pd} = \overline{F}_{pd} \\ F^+_{pq} = \overline{F}_{pq} \end{array}\right\}, \tag{4.26}$$

$$\left.\begin{array}{l} F^+_{sd} = \overline{F}_{sd} \\ F^+_{sq} = \overline{F}_{sq} \end{array}\right\}, \tag{4.27}$$

where $\overline{F}_{pd}, \overline{F}_{pq}, \overline{F}_{sd}$ and $\overline{F}_{sq}$ are the mean values of F_{pd}, F_{pq}, F_{sd} and F_{sq}, respectively. From (4.24) and (4.25), the negative sequence components can be obtained as follows:

$$\left.\begin{array}{l} F^-_{pd} = (F_{pd} - \overline{F}_{pd})\cos(2\omega_p t) - (F_{pq} - \overline{F}_{pq})\sin(2\omega_p t) \\ F^-_{pq} = (F_{pq} - \overline{F}_{pq})\cos(2\omega_p t) + (F_{pd} - \overline{F}_{pd})\sin(2\omega_p t) \end{array}\right\}, \tag{4.28}$$

$$\left.\begin{array}{l} F^-_{sd} = (F_{sd} - \overline{F}_{sd})\cos(2\omega_p t) + (F_{sq} - \overline{F}_{sq})\sin(2\omega_p t) \\ F^-_{sq} = (F_{sq} - \overline{F}_{sq})\cos(2\omega_p t) - (F_{sd} - \overline{F}_{sd})\sin(2\omega_p t) \end{array}\right\} \tag{4.29}$$

"Signal delay cancellation" described in [4], is the second method. In this method, the *abc* system is firstly converted to the stationary *αβ* reference frame, and then it is delayed for *T*/4 as formulated below:

$$\begin{bmatrix} F_\alpha(t) \\ F_\beta(t) \end{bmatrix} = \begin{bmatrix} F_\alpha^+(t)+F_\alpha^-(t) \\ F_\beta^+(t)+F_\beta^-(t) \end{bmatrix} = \begin{bmatrix} F^+\cos(\omega t+\phi^+)+F^-\cos(-\omega t+\phi^-) \\ F^+\sin(\omega t+\phi^+)+F^-\sin(-\omega t+\phi^-) \end{bmatrix}, \tag{4.30}$$

$$\begin{bmatrix} F_\alpha(t-\dfrac{T}{4}) \\ F_\beta(t-\dfrac{T}{4}) \end{bmatrix} = \begin{bmatrix} F^+\sin(\omega t+\phi^+)-F^-\sin(\omega t+\phi^-) \\ -F^+\cos(\omega t+\phi^+)+F^-\cos(-\omega t+\phi^-) \end{bmatrix} \tag{4.31}$$

From (4.30) and (4.31), the positive and negative sequence components can be calculated as follows:

$$\begin{bmatrix} F_\alpha^+(t) \\ F_\beta^+(t) \\ F_\alpha^-(t) \\ F_\beta^-(t) \end{bmatrix} = \frac{1}{2} \begin{bmatrix} 1 & 0 & 0 & -1 \\ 0 & 1 & 1 & 0 \\ 1 & 0 & 0 & 1 \\ 0 & 1 & -1 & 0 \end{bmatrix} \begin{bmatrix} F_\alpha(t) \\ F_\beta(t) \\ F_\alpha(t-T/4) \\ F_\beta(t-T/4) \end{bmatrix} \tag{4.32}$$

The positive and negative sequences in the stationary *αβ* reference frame will then be transformed into positive and negative *dq* sequences using:

$$\begin{bmatrix} F_d^+(t) \\ F_q^+(t) \end{bmatrix} = \begin{bmatrix} \cos\theta & \sin\theta \\ -\sin\theta & \cos\theta \end{bmatrix} \begin{bmatrix} F_\alpha^+(t) \\ F_\beta^+(t) \end{bmatrix}, \tag{4.33}$$

$$\begin{bmatrix} F_d^-(t) \\ F_q^-(t) \end{bmatrix} = \begin{bmatrix} \cos\theta & -\sin\theta \\ \sin\theta & \cos\theta \end{bmatrix} \begin{bmatrix} F_\alpha^-(t) \\ F_\beta^-(t) \end{bmatrix} \tag{4.34}$$

The third and fourth method are filtering-dependent. The positive (negative) Park's transformation is applied to variables *F* in the *abc* system to produce variables *F* in the positive (negative) *dq* synchronously rotating reference frame. It is well-known fact that negative sequence components manifest themselves as second-order harmonics in the positive *dq* synchronously rotating reference frame according to (4.2), and vice-versa for the positive sequence components. Hence, a low-pass filter [4], or notch filter [67] can be used to separate positive and negative sequence components in real time.

The results of applying the aforementioned separation methods are presented in Figure 4.3. The results show that without the four listed separation methods, second-order harmonics appear in the *dq* positive synchronously rotating reference frame.
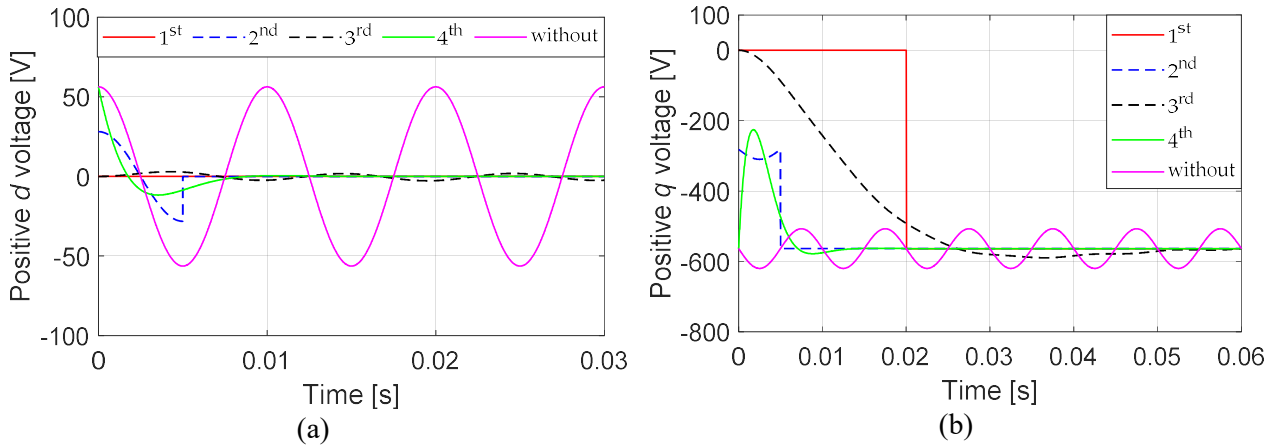
Figure 4.3. Unbalanced voltages in positive *dq* reference frame with and without using the separation methods (a) positive *d* component (b) positive *q* component.

4.4 Conventional Vector Control Strategy under Unbalanced Grid Voltage Conditions

In order to demonstrate the performance of the conventional vector control presented in section 3.3 under unbalanced grid conditions, simulations of the dynamical model are conducted. The following test is performed:

- The machine started as a slip-ring-induction machine (i.e., with the shorted secondary winding) until it reaches the steady synchronous speed of 500rpm, then the control is enabled at $t = 60$ s, with a super-synchronous speed reference set to 600rpm. After reaching a steady state, 10% VUF was introduced at 80 s and terminated at 100 s. The system response to the conventional single PI current control design to a given period of unbalanced operation is shown in Figure 4.4.
- The MTPIA objective is selected by adopting $i_{sd} = 0$. This approach minimizes the secondary current magnitude, and hence reduces both the copper and converter losses, for a given torque.

With the conventional VC, the primary current becomes unbalanced in the presence of grid voltage unbalance as clearly be noticed in Figure 4.4(g). In addition, the secondary currents contain both the fundamental component of 10 Hz and the harmonic component of 110 Hz, as presented in Figure 4.4(h). Although the averaged torque, active and reactive powers were regulated, significant torque and powers oscillations are still observed as clearly seen in Figure 4.4(d), Figure 4.4(e) and Figure 4.4(f).

It can be concluded that during grid voltage unbalance, the positive sequence components are well regulated by common PI controllers, while the negative sequence component cannot be fully regulated due to the controller's limited bandwidth. Therefore, conventional VC without backward sequence control is not able to solve problems caused by the unbalanced grid voltage and consequently gives an unsatisfactory performance.

Hence, the extension of the conventional VC should be performed with additional negative sequence current controllers for BDFRG secondary winding, which is leading to the development of a new and original control algorithm, presented in the next section
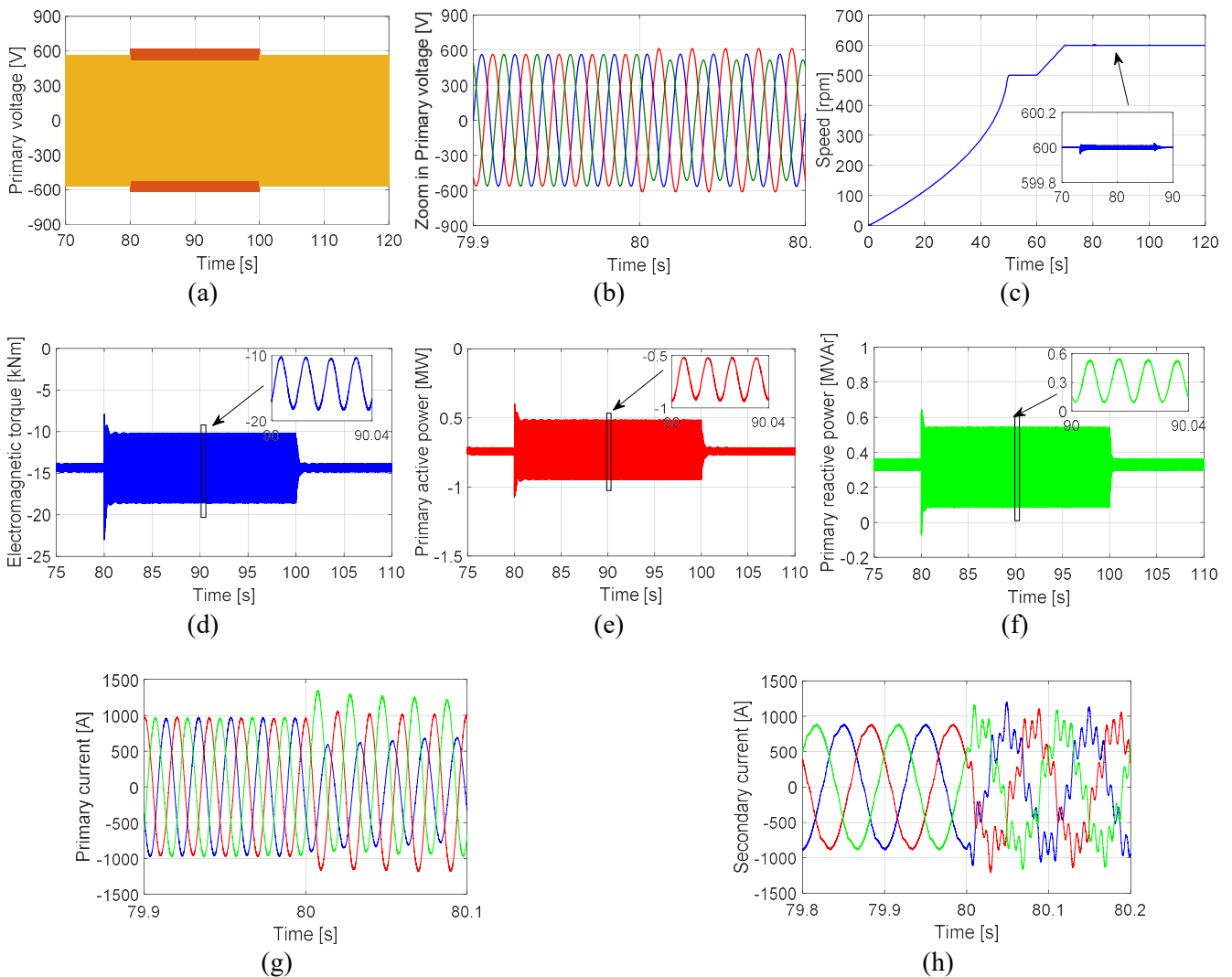
Figure 4.4. Simulated results with conventional control under transient primary voltage unbalance of 10%VUF during 80–100 s, with a constant rotor speed at 600 rpm; (a) primary voltage profile; (b) transient transaction period between normal and unbalanced condition; (c) speed curve of the BDFRG; (d) electromagnetic torque; (e) primary active power; (f) primary reactive power; (g) Transient transaction period between normal and unbalanced condition for the primary current; (h) transient transaction period for the secondary current.

4.5 Extended Vector Control Strategy under Unbalanced Grid Voltage Conditions

The negative sequence controller design is similar to the positive controller design. The controller uses a standard PI controller with decoupling and feed forward control loops to generate the reference current vector. Under unbalanced conditions, the positive and negative sequence components were completely decoupled as shown in (4.9)–(4.16), and thus the BDFRG can be controlled in *dq* positive and negative reference frames independently.

Choosing appropriate reference values for the controller is a key point in the design of the auxiliary controller. In the following, different control targets for the controller design are described, where each target uses a unique reference value. There are four secondary current components, i.e. i^+_{sd}, i^+_{sq}, i^-_{sd}, and i^-_{sq} to be controlled. Apart from the average primary active and reactive power, i.e. P_{av}, and Q_{av} in (4.20) and (4.21), two more parameters can be controlled. Hence, there are four selectable control targets that can be addressed [67]. Using the FOC approach by aligning the d^+_p-axis to λ_p, i.e. $\lambda^+_{pq} = 0$, the secondary reference current can then be calculated for each selectable control target, as further elaborated.

- Target I. Balancing primary currents to ensure uniform heating in the primary winding.

The balanced primary currents imply that $i^-_{pd} = 0$ and $i^-_{pq} = 0$. According to (4.15), the negative sequence primary current can be expressed as:

$$\left.\begin{aligned} i^-_{pd} &= \frac{\lambda^-_{pd} - L_{ps}i^-_{sd}}{L_p} \\ i^-_{pq} &= \frac{\lambda^-_{pq} + L_{ps}i^-_{sq}}{L_p} \end{aligned}\right\} \qquad (4.35)$$

And hence the reference negative sequence secondary currents can be defined as:

$$i^{-*}_{sd} = \frac{\lambda^-_{pd}}{L_{ps}}, \quad i^{-*}_{sq} = \frac{-\lambda^-_{pq}}{L_{ps}}. \qquad (4.36)$$

In this case, the converter intentionally injects the backward sequence currents into the secondary winding to repress the corresponding components in the primary.

- Target II. Providing constant torque to reduce mechanical stresses on the turbine system.

The reference values are set to eliminate the torque pulsating terms presented in (4.23), i.e. $T_1 = T_2 = 0$. This condition can only be achieved if the BDFRG is controlled with the reference currents formulated as:

$$\left.\begin{aligned} T_1 = 0 &\Rightarrow i^{-*}_{sd} = \frac{\lambda^-_{pd}i^+_{sd} - \lambda^-_{pq}i^+_{sq}}{\lambda^+_{pd}} \\ T_2 = 0 &\Rightarrow i^{-*}_{sq} = -(\frac{\lambda^-_{pd}i^+_{sq} + \lambda^-_{pq}i^+_{sd}}{\lambda^+_{pd}}) \end{aligned}\right\} \qquad (4.37)$$

- Target III. Eliminating the double-frequency pulsations of the primary active power.

In this case, the oscillating terms of the primary active power in (4.20) should be zero. This can only be achieved under the following conditions:

$$i_{sd}^{-*} = \frac{\lambda_{pd}^-}{L_{ps}} - \frac{L_p}{L_{ps}}\left(\frac{(u_{pq}^-u_{pq}^+ - u_{pd}^+u_{pd}^-)}{u_{pd}^{+2} + u_{pq}^{+2}}i_{pd}^{+} - \frac{(u_{pd}^-u_{pq}^+ + u_{pd}^+u_{pq}^-)}{u_{pd}^{+2} + u_{pq}^{+2}}i_{pq}^{+}\right)$$

$$i_{sq}^{-*} = \frac{L_p}{L_{ps}}\left(\frac{(u_{pd}^-u_{pd}^+ - u_{pq}^-u_{pq}^+)}{u_{pd}^{+2} + u_{pq}^{+2}}i_{pq}^{+} - \frac{(u_{pd}^-u_{pq}^+ + u_{pd}^+u_{pq}^-)}{u_{pd}^{+2} + u_{pq}^{+2}}i_{pd}^{+}\right) - \frac{\lambda_{pq}^-}{L_{ps}}$$

(4.38)

- Target IV. Eliminating the double-frequency pulsations of the primary reactive power

The reference values are set to eliminate reactive power oscillatory terms. In this case, the oscillating terms of the primary reactive power in (12) should be zero i.e. $Q_1 = Q_2 = 0$. This can only be achieved under the following conditions:

$$i_{sd}^{-*} = \frac{\lambda_{pd}^-}{L_{ps}} - \frac{L_p}{L_{ps}}\cdot\left[\frac{(u_{pd}^+u_{pd}^- - u_{pq}^+u_{pq}^-)}{u_{pd}^{+2} + u_{pq}^{+2}}i_{pd}^{+} + \frac{(u_{pd}^+u_{pq}^- + u_{pq}^+u_{pd}^-)}{u_{pd}^{+2} + u_{pq}^{+2}}i_{pq}^{+}\right]$$

$$i_{sq}^{-*} = \frac{L_p}{L_{ps}}\left[\frac{(u_{pd}^+u_{pq}^- + u_{pq}^+u_{pd}^-)}{u_{pd}^{+2} + u_{pq}^{+2}}i_{pd}^{+} - \frac{(u_{pd}^+u_{pd}^- - u_{pq}^+u_{pq}^-)}{u_{pd}^{+2} + u_{pq}^{+2}}i_{pq}^{+}\right] - \frac{\lambda_{pq}^-}{L_{ps}}$$

(4.39)

- Target V. Eliminating the secondary currents pulsations.

The reference values in this case are set to eliminate the negative sequence secondary current. The most straight-forward approach of mitigating the secondary current oscillations is setting the negative sequence secondary current references to zero:

$$\left.\begin{matrix} i_{sd}^{-*} = 0 \\ i_{sq}^{-*} = 0 \end{matrix}\right\}$$

(4.40)

According to the previous discussion, a new control algorithm is proposed as shown in Figure 4.5.
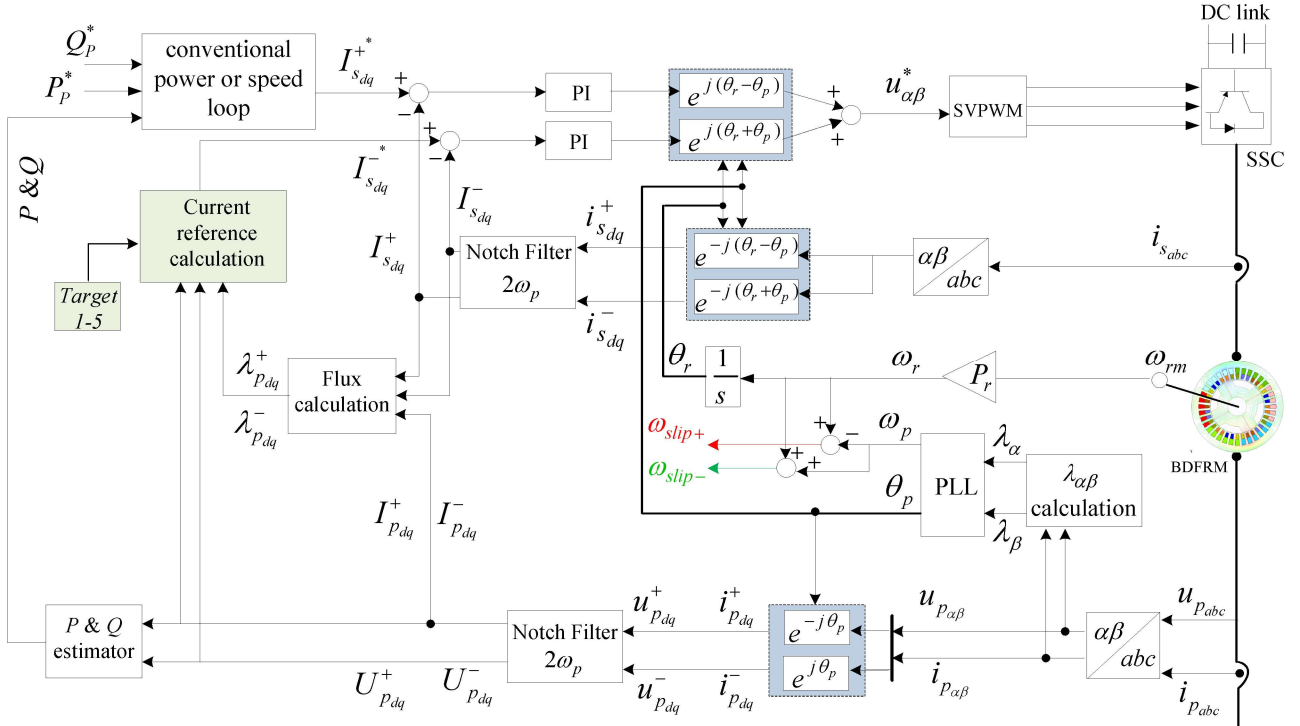
Figure 4.5. A block diagram of the proposed control strategies under unbalanced grid voltage conditions (sign "*" denotes reference values).

In order to achieve an accurate reference frame transformation, the PLL must only recognize the positive sequence primary flux. Therefore, a notch filter is used and tuned at $2\omega_p$ to remove the negative sequence components (Figure 4.6).
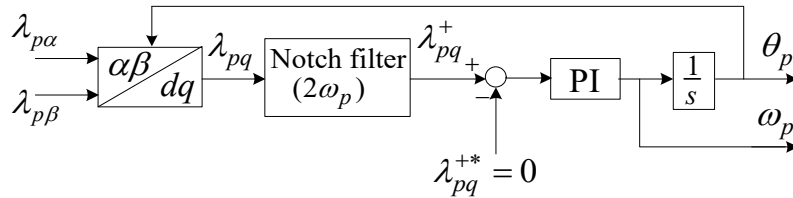
Figure 4.6. Block diagram of the phase-locked loop (PLL).

Once the angular frequency ω_p and position θ_p of the positive sequence primary flux are detected by the PLL, primary currents and flux in the stationary $\alpha\beta$ frame can be transformed to dq_p^+ and dq_p^- rotating reference frames. Likewise, the secondary current will also be transformed to dq_s^+ and dq_s^- reference frames.

4.6 Simulation Results

The simulations of the proposed control algorithm are implemented in Matlab/Simulink using the parameters of a 1.5MW BDFRG-based WECS given in Table 4.1. The rated DC-link voltage is set to 1200 V and a standard Space Vector Modulation (SVM) with a switching frequency of 4 kHz is used. In order to achieve the MTPIA objective for the main controller, i_{sd}^+ is set to zero.

Table 4.1. BDFRG parameters

Parameter	Value
Rated power (MW)	1.5
Line voltage (V), frequency (Hz)	690, 50
Rated speed (rpm)	600
Primary/secondary, rotor poles	8/4, 6
Primary winding resistance (Ω)	0.007
Primary inductance (H)	0.0047
Secondary winding resistance (Ω)	0.014
Secondary inductance (H)	0.0057
Magnetizing (mutual) inductance (H)	0.00475
BDFRG and wind turbine inertia constant H (s)	2.6

Under regular grid conditions with slight voltage imbalance, the system could be regulated with a conventional controller, while the negative sequence current controller is disabled. When the voltage unbalance is detected, the auxiliary controller (i.e. negative sequence current controller) will instantly be enabled and the negative sequence reference currents are generated subjected to the selected control target. The positive and negative sequence reference currents are passed to the main and auxiliary PI controller to generate the required secondary control voltage.

Initially, the system runs under balanced conditions with the BDFRG being started as a slip ring induction machine (i.e. with the shorted secondary winding). After reaching the steady-state, the conventional FOC is enabled, and a 10% voltage unbalance is instigated at 80 s time instant. Figure 4.7-Figure 4.10 show a comparison of the responses obtained by conventional vector control and the proposed control design in different modes based on the selected target. Following the unbalance inception at 80 s, the conventional design cannot provide a sufficient control of the negative-sequence currents, resulting in significant active power oscillations and unbalanced currents in the primary winding. On the other hand, with the proposed control design, the negative sequence currents are completely controlled according to the Target I requirements as illustrated in Figure 4.7.

(a) (b) (c)
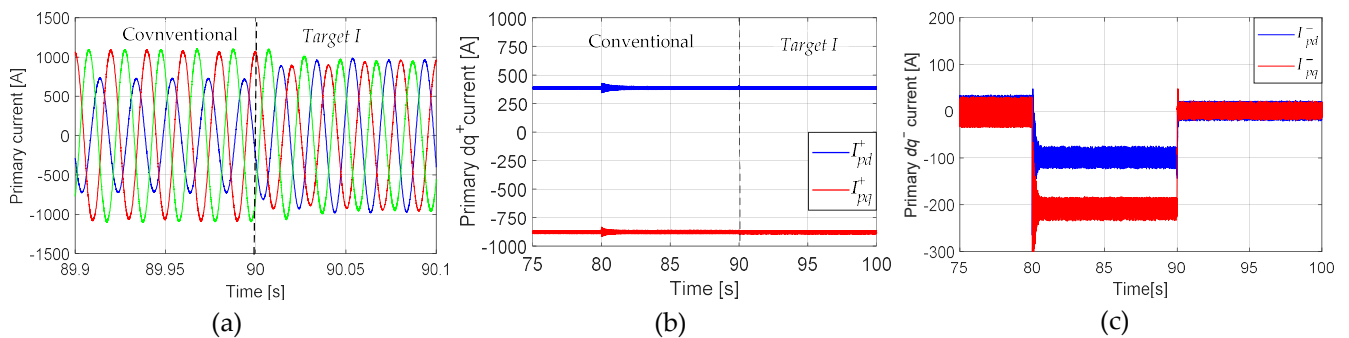
Figure 4.7. Simulation results comparison during voltage unbalance of 10% starting at 80 s with Target I for balancing primary currents (a) primary current; (b) positive components; (c) negative components

Figure 4.8 shows that the torque oscillations can be mitigated with the proposed control design applying Target II. It is worth noticing that torque oscillation is the most concerning issue during grid voltage unbalance [67]. According to (4.21) and (4.23), the primary reactive power pulsations are also suppressed.
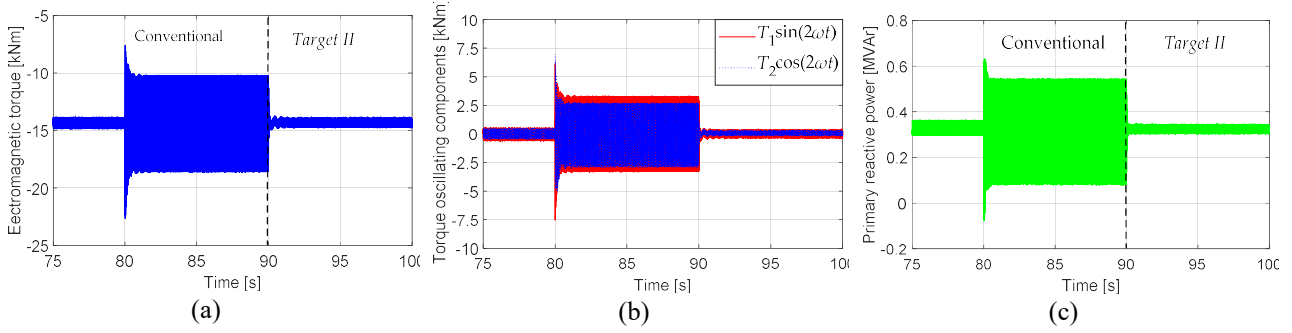
Figure 4.8. Simulation results comparison with Target II for torque and reactive power ripple elimination (a) torque response; (b) torque components; (c) primary reactive power

It can also be seen that with the proposed controller, the operation of the system is much smoother with reduced primary active power pulsations according to the Target III requirements as shown in Figure 4.9.
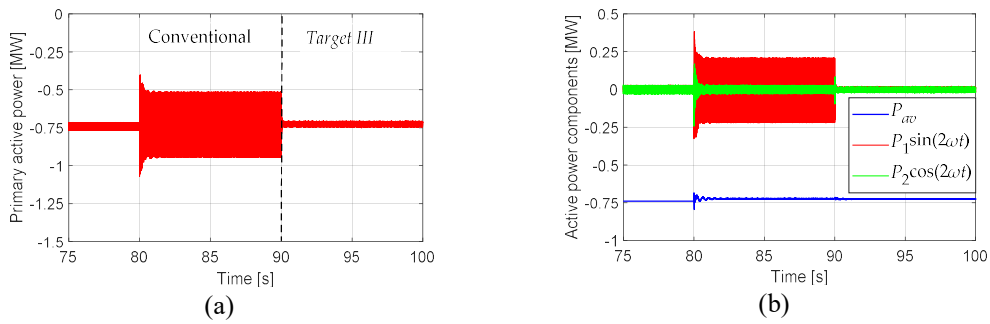
Figure 4.9. Simulation results comparison with Target III for primary active power ripple elimination(a) Primary active power response; (b) Active power components

As described in (4.4) and Figure 4.2, under unbalanced conditions, the secondary current contains both the fundamental component of 10 Hz (positive slip 60 Hz-50 Hz) and the harmonic component of 110 Hz (negative slip 60 Hz +50 Hz), which can be eliminated by applying the proposed control with Target V. Thus, the secondary current immediately becomes harmonic free as it is clearly observed from Figure 4.10.
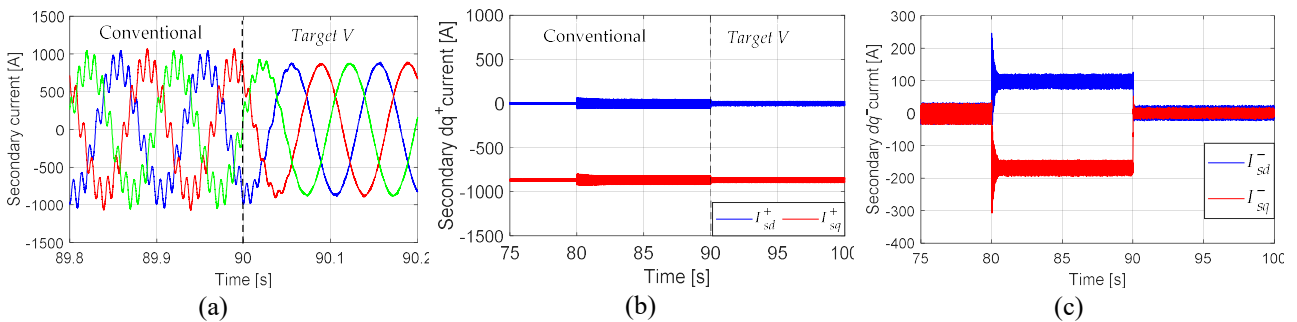
Figure 4.10. Simulation results comparison with Target V for secondary currents harmonics elimination (a) secondary current; (b) positive components; (c) negative components

In order to evaluate the control targets under consideration, they have been applied sequentially as shown in Figure 4.11(a). For all four control objectives, P_{av} and Q_{av} are controlled to be constant. As a result, the positive sequence components, i^+_{pdq} and i^+_{sdq} remain constant, too. With Target I, i^-_{pdq} was controlled at zero. The values of i^-_{pdq} increased during Target II and Target III. In contrast,

56

these values are partially controlled during the Target V period due to the indirect coupling between the primary and secondary currents.
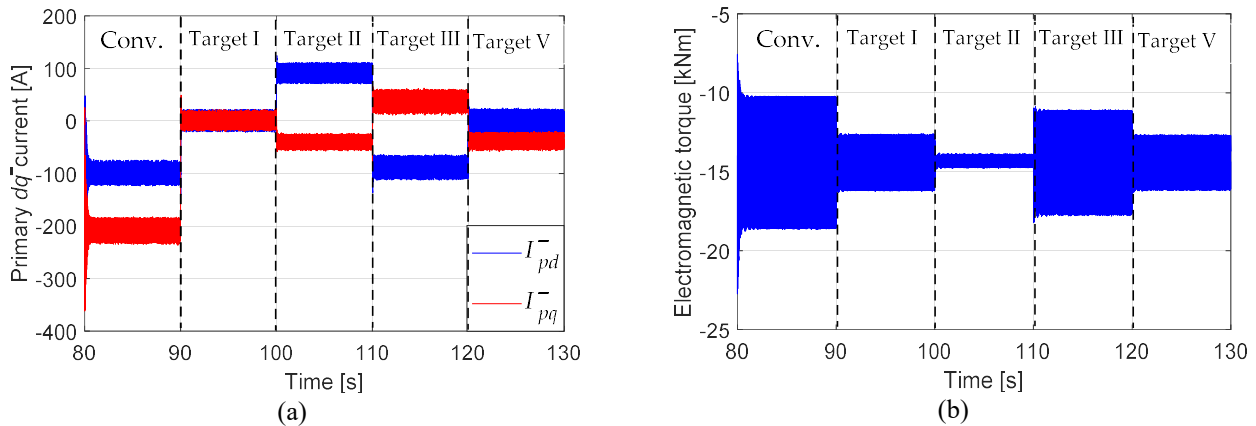
Figure 4.11. Simulated results with 10% primary voltage unbalance: 90–100 s: Target I; 100–110 s: Target II; 110–120 s: Target III; 120–130 s: Target V; (a) primary negative sequence currents; (b) electromagnetic torque

Figure 4.11(b) shows that by applying the proposed control strategy with Target II, the BDFRG generation system can be improved by eliminating the double-frequency pulsations of electromagnetic torque. On the other hand, significant pulsations can be observed during the Target III period and relatively lower pulsations can be seen during the Target V period.

According to (4.21) and (4.23), the pulsation of primary reactive power would diminish when the pulsations of the electromagnetic torque are eliminated as clearly seen from Figure 4.12(a)
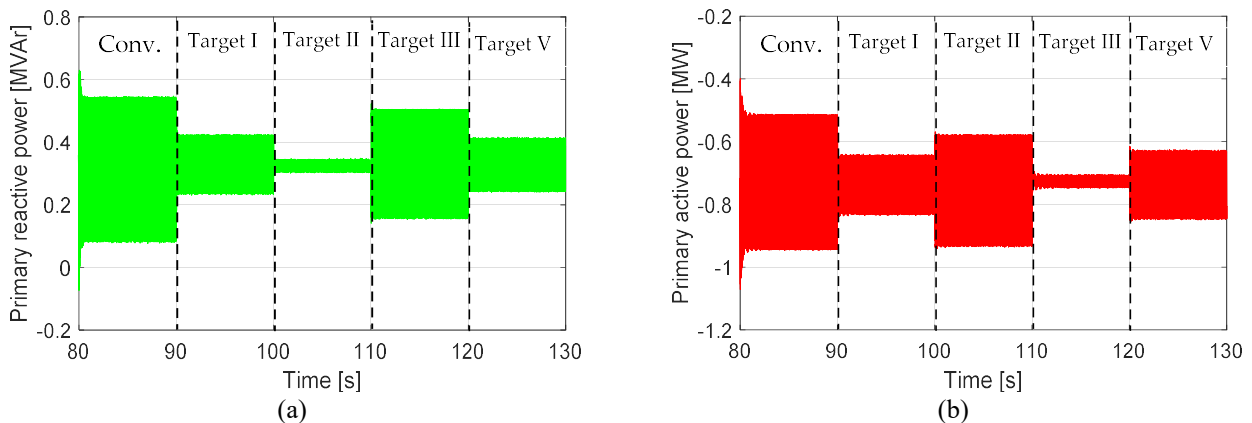
Figure 4.12. Simulated results with different control targets: 90–100s: Target I; 100–110s: Target II; 110–120s: Target III; 120–130s: Target V; (a) primary reactive power; (b) primary active power

Further reduction of active power oscillations is achieved with Target III, as shown in Figure 4.12(b). Moreover, increased oscillation can be observed during the Target II period.

Figure 4.13 shows the behavior of the secondary current under different control targets. Obviously, with Target V, the negative sequence components are completely eliminated. On the other hand, the negative sequence secondary current cannot be completely eliminated during the rest of the considered targets.

57
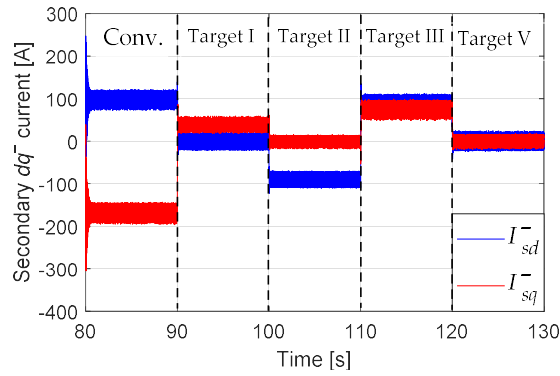
Figure 4.13. Simulated results for the secondary negative sequence currents with different control targets: 90–100s: Target I; 100–110s: Target II; 110–120s: Target III; 120–130s: Target V

Table 4.2 recaps the following metrics for different control targets: the primary currents unbalance (i.e. the deviation from positive sequence value), total harmonic distortion of the secondary current, pulsations of the electromagnetic torque, and pulsations of the primary active and reactive power.

Figure 4.11-Figure 4.13 and Table 4.2 clearly show that with the controller set to Target I, the primary current unbalance became very low (about 0.8%) compared to the result equal to 24% achieved with conventional control design. When it is switched to Target II at 100 s, the torque pulsations are practically eliminated (about 0.6% left), as well as the primary reactive power oscillations. When Target III was chosen at 110 s, the primary active power pulsations have been mitigated to 2.1%. At 120 s, when the controller was set to Target V, the secondary current immediately became harmonic free (110 Hz), and the total harmonic distortion (THD) factor has been reduced to 0.7%.

Table 4.2. Comparisons of different control targets with conventional control

Target	I	II	III	V	conventional
I_p unbalance (%)	0.8	11.3	10.3	5	24
I_s distortion (%)	4.5	10.3	13.8	0.7	22
T_e pulsations (%)	11.2	0.6	24	10.7	±27
P_p pulsations (%)	14.5	22	2.1	13	±28
Q_p pulsations (%)	28	0.4	34	26	±42

One can conclude that by using the aforementioned control design objectives, it is not possible to achieve more than a single control objective simultaneously. Therefore, to achieve optimal performance under UGVCs, the proposed control strategy should be optimized.

In order to evaluate the performance of the proposed control under variable speed and loading conditions (Figure 4.14), the speed mode change from super to sub-synchronous is analyzed. The test is conducted with the MPPT.

The BDFRG control response to reference speed and associated load in a narrow range around synchronous speed are shown in Figure 4.15-Figure 4.17.
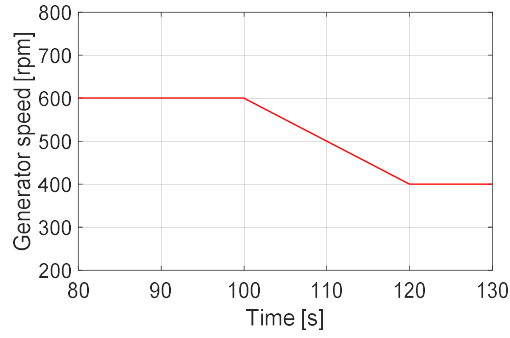
Figure 4.14. Speed reduction from 600 rpm to 400 rpm

Under Target I, the primary current remained balanced during the transient and the new steady state as clearly seen in Figure 4.15. Good torque response can also be observed from Figure 4.16(a) during the transient transaction period between super- and sub-synchronous speeds according to Target II. In addition, the reactive power remained constant which is expected under the MTPIA. During the speed change, the primary active power is well controlled according to the Target III requirements as shown in Figure 4.16(c).

Furthermore, Figure 4.17 shows a phase sequence reversal from super- to sub-synchronous speed mode with good performance under Target V.

(a)   (b)   (c)
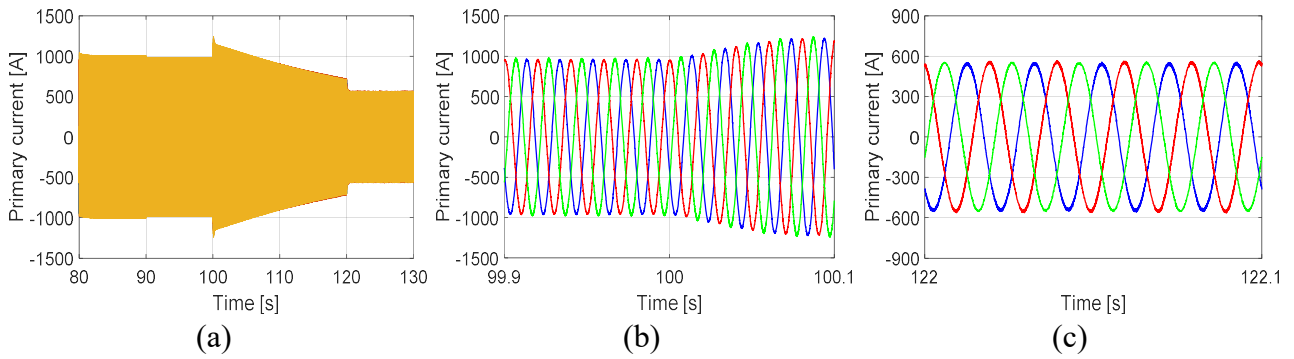
Figure 4.15. .(a) Primary current response to reference speed dependent load variations (Target I); (b) transient response of the primary current; (c) steady state of the primary current

(a)   (b)   (c)
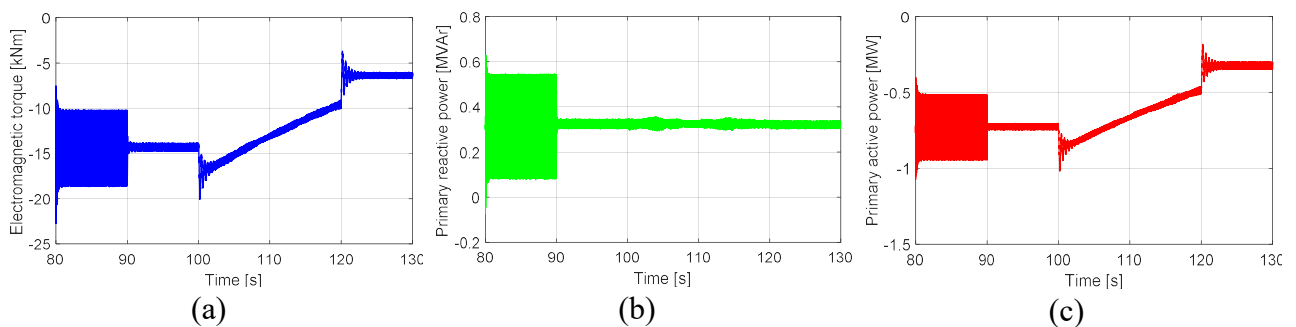
Figure 4.16. (a) Electromagnetic torque response to reference speed dependent load variations (Target II); (b) primary reactive power (Target II); (c) primary active power (Target III).

59
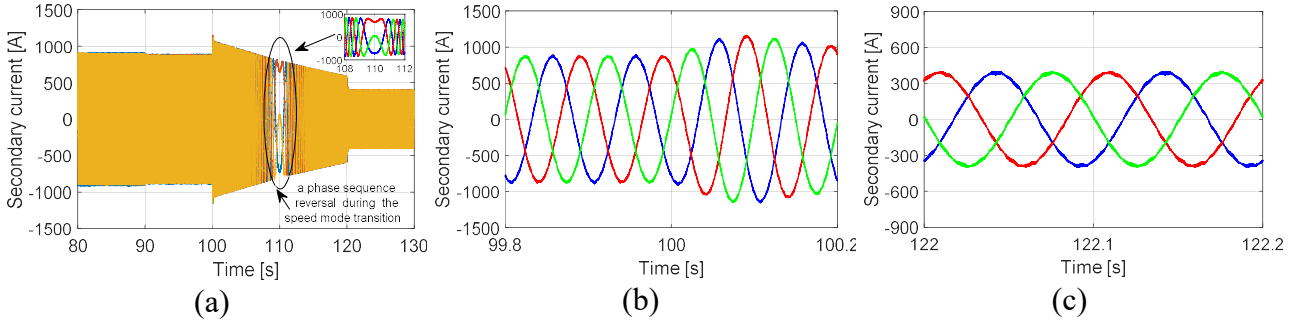
Figure 4.17. (a) Secondary current response, showing a phase sequence reversal in from super- to sub-synchronous speed mode (Target V); (b) transient response of the secondary current; (c) steady state of the secondary current

4.7 BDFRG Vector Control Optimization under Unbalanced Grid Conditions

As it can be seen from section 4.5, the reference values for secondary currents can be set to achieve only one pair of objectives at a time out of the total of five objectives. Therefore, an optimal control strategy is required to comprise all the aforementioned objectives simultaneously, which is leading to the development of a second new and original control algorithm within this thesis.

In the proposed optimal control algorithm, the controller's reference values are selected using a multi-objective optimization (MOO) method. A weighted-sum approach is used to convert multiple objectives into a parametric single-objective cost function.

4.7.1 Overview of the Multi-Objective Optimization (MOO) Formulation

The general MOO problem can be stated as follows [104, 105]:

$$\underset{\text{x}}{\text{Minimize: }} F(\text{x}) = [F_1(\text{x}), F_2(\text{x}), ..., F_k(\text{x})]^T ,$$
$$\text{subject to : } g_j(\text{x}) \leq 0; \ j = 1, 2, ..., m \tag{4.41}$$

where *k* is the number of objective functions and *m* is the number of inequality constraints.

The aim is to define the reference values for negative sequence *dq* secondary currents in order to minimize negative sequence terms of secondary current, negative terms of primary current, oscillatory terms of torque, and oscillatory terms of active/reactive powers, simultaneously.

The most widely-used method for multi-objective optimization is the so-called weighted sum method. Using the weighted sum method to solve the problem in (4.41) requires choosing scalar weight coefficients w_i and minimizing the composite objective function in (4.42):

$$U = \sum_{i=1}^{k} w_i F_i(\text{x}) \tag{4.42}$$

One may set the weight coefficients to reflect objective-importance directly, but this way can lead to difficulties. This difficulty arises because the relative magnitudes of the terms $w_i F_i$ in (4.42)

dictate the solution to the weighted sum, not just the magnitudes of the functions or weight coefficients alone. In addition, the value of a certain weight coefficient is significant not only relative to other weight coefficients but also relative to its corresponding objective function [105].

In the given optimization problem, three weight coefficients are considered:

- The first weight coefficient is the scaling factor and is considered for all objectives as:

$$w_{1,i}=1; \, i=1, \, ..., \, 10 \, . \tag{4.43}$$

- The second weight coefficient represents the importance of the objectives in the optimization based on an expert opinion. The optimization of particular terms may be of higher importance. For example, for WECS that are often installed in remote areas with weak grids, the system power quality may be of lower priority than the torque, and the system longevity is of higher importance [106]. For this purpose, coefficient 2 is assumed for the secondary current and torque, and coefficient 1 is considered for the rest of the objectives:

$$w_{2,i} = \begin{cases} 2; \, i \in \{1,2,7,8\} \\ 1; \quad else \end{cases} \tag{4.44}$$

- The third weight coefficient, which is considered only for negative sequence secondary and primary currents, represents the sensitivity of $P_{1,2}$, $Q_{1,2}$, and $T_{1,2}$ variations due to changes in i_s^- and i_p^- [106]. The sensitivity of $P_{1,2}$, $Q_{1,2}$, $T_{1,2}$ and i_p^- variations due to changes in i_s^- can be determined from (4.20), (4.21), (4.23) and (4.35) respectively:

$$\left. \begin{aligned} S_{i_s^-}^{P_1} &= \frac{\delta P_1}{\delta i_{sd}^-} + \frac{\delta P_1}{\delta i_{sq}^-} = \frac{3L_{ps}}{2L_p}(u_{pq}^+ + u_{pd}^+) \\ S_{i_s^-}^{P_2} &= \frac{\delta P_2}{\delta i_{sd}^-} + \frac{\delta P_2}{\delta i_{sq}^-} = \frac{3L_{ps}}{2L_p}(-u_{pd}^+ + u_{pq}^+) \end{aligned} \right\} \tag{4.45}$$

$$\left. \begin{aligned} S_{i_s^-}^{Q_1} &= \frac{\delta Q_1}{\delta i_{sd}^-} + \frac{\delta Q_1}{\delta i_{sq}^-} = \frac{3L_{ps}}{2L_p}(-u_{pd}^+ + u_{pq}^+) \\ S_{i_s^-}^{Q_2} &= \frac{\delta Q_2}{\delta i_{sd}^-} + \frac{\delta Q_2}{\delta i_{sq}^-} = \frac{3L_{ps}}{2L_p}(-u_{pq}^+ - u_{pd}^+) \end{aligned} \right\} \tag{4.46}$$

In the primary field orientation (PFO) frame, $\lambda_{pd}^+ = \lambda_p^+$ and $\lambda_{pq}^+ = 0$:

$$\left. \begin{aligned} S_{i_s^-}^{T_1} &= \frac{\delta T_1}{\delta i_{sd}^-} + \frac{\delta T_1}{\delta i_{sq}^-} = \frac{3P_r L_{ps}}{2L_p}\lambda_p^+ \\ S_{i_s^-}^{T_2} &= \frac{\delta T_2}{\delta i_{sd}^-} + \frac{\delta T_2}{\delta i_{sq}^-} = \frac{3P_r L_{ps}}{2L_p}\lambda_p^+ \end{aligned} \right\}, \tag{4.47}$$

$$S^{i^-_{pd}}_{i^-_s} = \frac{\delta i^-_{pd}}{\delta i^-_{sd}} + \frac{\delta i^-_{pd}}{\delta i^-_{sq}} = -\frac{L_{ps}}{L_p} \left.\begin{matrix} \\ \\ \\ \\ \\ \end{matrix}\right\}$$

$$S^{i^-_{pq}}_{i^-_s} = \frac{\delta i^-_{pq}}{\delta i^-_{sd}} + \frac{\delta i^-_{pq}}{\delta i^-_{sq}} = \frac{L_{ps}}{L_p}$$

(4.48)

Sensitivities of the oscillatory parts of the active and reactive powers corresponding to the negative sequence primary current are as follows:

$$S^{P_1}_{i^-_p} = \frac{\dfrac{\delta P_1}{\delta i^-_{sd}}}{\dfrac{\delta i^-_{pd}}{\delta i^-_{sd}}} + \frac{\dfrac{\delta P_1}{\delta i^-_{sq}}}{\dfrac{\delta i^-_{pq}}{\delta i^-_{sq}}} = \frac{3}{2}(u^+_{pd} - u^+_{pq})$$

$$S^{P_2}_{i^-_p} = \frac{\dfrac{\delta P_2}{\delta i^-_{sd}}}{\dfrac{\delta i^-_{pd}}{\delta i^-_{sd}}} + \frac{\dfrac{\delta P_2}{\delta i^-_{sq}}}{\dfrac{\delta i^-_{pq}}{\delta i^-_{sq}}} = \frac{3}{2}(u^+_{pd} + u^+_{pq})$$

(4.49)

$$S^{Q_1}_{i^-_p} = \frac{\dfrac{\delta Q_1}{\delta i^-_{sd}}}{\dfrac{\delta i^-_{pd}}{\delta i^-_{sd}}} + \frac{\dfrac{\delta Q_1}{\delta i^-_{sq}}}{\dfrac{\delta i^-_{pd}}{\delta i^-_{sq}}} = \frac{3}{2}(u^+_{pd} + u^+_{pq})$$

$$S^{Q_2}_{i^-_p} = \frac{\dfrac{\delta Q_2}{\delta i^-_{sd}}}{\dfrac{\delta i^-_{pd}}{\delta i^-_{sd}}} + \frac{\dfrac{\delta Q_2}{\delta i^-_{sq}}}{\dfrac{\delta i^-_{pd}}{\delta i^-_{sq}}} = \frac{3}{2}(u^+_{pq} - u^+_{pd})$$

(4.50)

Equations (4.45)-(4.50) denote that any rate of reduction in the secondary and primary currents decreases the other portions of the objective function. Thus, for minimizing the objective function, a reduction in negative sequence secondary and primary currents is more significant than the other objectives. Therefore, the third weight coefficient for negative sequence secondary and primary currents can be considered as follows:

$$w^{i^-_s}_3 = (\frac{3P_r L_{ps}}{2L_p} \lambda^+_p + \frac{3L_{ps}}{2L_p}(u^+_{pq} - u^+_{pd}) + \frac{L_{ps}}{L_p}) + 1 \quad ,$$

(4.51)

$$w^{i^-_p}_3 = \frac{3}{2}(u^+_{pd} + u^+_{pq}) + 1$$

(4.52)

For the rest of the objectives, the third weight coefficient is considered to be 1. The resulting multi-objective function can be obtained as follows:

$$U = W_1 T_1^2 + W_2 T_2^2 + W_3 P_1^2 + W_4 P_2^2 + W_5 Q_1^2 + W_6 Q_2^2 + W_7 i_{ds}^{-2} + W_8 i_{qs}^{-2} + W_9 i_{dp}^{-2} + W_{10} i_{qp}^{-2}$$

(4.53)

where;

$$W_1 = (w_{1,1}w_{2,1}w_{3,1})_{T_1} = 2, \quad W_2 = (w_{1,2}w_{2,2}w_{3,2})_{T_2} = 2, \quad W_3 = (w_{1,3}w_{2,3}w_{3,3})_{P_1} = 1, \quad W_4 = (w_{1,4}w_{2,4}w_{3,4})_{P_2} = 1$$

$$W_5 = (w_{1,5}w_{2,5}w_{3,5})_{Q_1} = 1, \quad W_6 = (w_{1,6}w_{2,6}w_{3,6})_{Q_2} = 1$$

$$W_7 = (w_{1,7}w_{2,7}w_{3,7})_{i_{ds}^-} = 2\left((\frac{3P_r L_{ps}}{2L_p}\lambda_p^+ + \frac{3L_{ps}}{2L_p}(u_{pq}^+ - u_{pd}^+) + \frac{L_{ps}}{L_p}) + 1 \right)$$

$$W_8 = (w_{1,8}w_{2,8}w_{3,8})_{i_{qs}^-} = 2\left((\frac{3P_r L_{ps}}{2L_p}\lambda_p^+ + \frac{3L_{ps}}{2L_p}(u_{pq}^+ - u_{pd}^+) + \frac{L_{ps}}{L_p}) + 1 \right)$$

$$W_9 = (w_{1,9}w_{2,9}w_{3,9})_{i_{dp}^-} = \frac{3}{2}(u_{pd}^+ + u_{pq}^+) + 1 \quad , \quad W_{10} = (w_{1,10}w_{2,10}w_{3,10})_{i_{qp}^-} = \frac{3}{2}(u_{pd}^+ + u_{pq}^+) + 1$$

In the utility function U, undesirable effects of negative sequence currents, torque and power oscillations are determined according to their absolute size, not the positive or negative signs. Therefore, the power of two or the absolute value of the objective functions $F_i(x)$ should be used to turn the problem into an unconstrained optimization problem.

In order to find the optimal reference values of i^-_{ds} and i^-_{qs}, the gradient of U in (4.53) is equalized to zero, yielding a closed form solution for global optimum.

$$\nabla U_{i_{ds}^-} = 0, \quad \nabla U_{i_{qs}^-} = 0 \tag{4.54}$$

The secondary current references can be deduced as follows:

$$I_{ds}^* = \frac{\begin{bmatrix} (L_{ps}(2u_{pq}^- + 3u_{pd}^+ u_{pq}^- + 3u_{pq}^+ u_{pq}^- + \\ 18\lambda_{pd}^- u_{pd}^{+2}\omega_p + 18\lambda_{pd}^- u_{pq}^{+2}\omega_p + \\ 9L_{ps}\lambda_p^+\lambda_{pd}^- i_{ds}^+ p_r^2\omega_p - 9L_{ps}\lambda_p^+\lambda_{qp}^- i_{qs}^+ p_r^2\omega_p)) \end{bmatrix}}{\begin{bmatrix} (\omega_p(9L_{ps}^2\lambda_p^{+2}p_r^2 + 36L_{ps}^2 u_{pd}^{+2} + \\ 3L_{ps}^2 u_{pd}^+ + 36L_{ps}^2 u_{pq}^{+2} + 3L_{ps}^2 u_{pq}^+ + \\ 2L_{ps}^2 + 6L_{ps}L_p\lambda_p^+ p_r - 6L_{ps}L_p u_{pd}^+ + \\ 6L_{ps}L_p u_{pq}^+ + 4L_{ps}L_p + 4L_p^2)) \end{bmatrix}}, \tag{4.55}$$

$$I_{ds}^* = \frac{\begin{bmatrix} -(L_{ps}(18\lambda_{pq}^- u_{pd}^{+2}\omega_p - 3u_{pd}^+ u_{pd}^- - \\ 3u_{pd}^- u_{pq}^+ - 2u_{pd}^- + 18\lambda_{pq}^- u_{pq}^{+2}\omega_p + \\ 9L_{ps}\lambda_p^+\lambda_{pd}^- i_{qs}^+ p_r^2\omega_p + 9L_{ps}\lambda_p^+\lambda_{qp}^- i_{ds}^+ p_r^2\omega_p)) \end{bmatrix}}{\begin{bmatrix} (\omega_p(9L_{ps}^2\lambda_p^{+2}p_r^2 + 36L_{ps}^2 u_{pd}^{+2} + \\ 3L_{ps}^2 u_{pd}^+ + 36L_{ps}^2 u_{pq}^{+2} + 3L_{ps}^2 u_{pq}^+ + \\ 2L_{ps}^2 + 6L_{ps}L_p\lambda_p^+ p_r - 6L_{ps}L_p u_{pd}^+ + \\ 6L_{ps}L_p u_{pq}^+ + 4L_{ps}L_p + 4L_p^2)) \end{bmatrix}} \tag{4.56}$$

In order to implement the optimized control strategy, the secondary reference currents calculated in (4.55) and (4.56) are used. The simulation results presented in Figure 4.18-Figure 4.20 prove that the proposed optimized control method can significantly enhance the control and operation of the BDFRG system under UGVCs. From Figure 4.18, it can be clearly observed that the negative sequence components of the primary current are mitigated as soon as the optimized controllers are enabled.
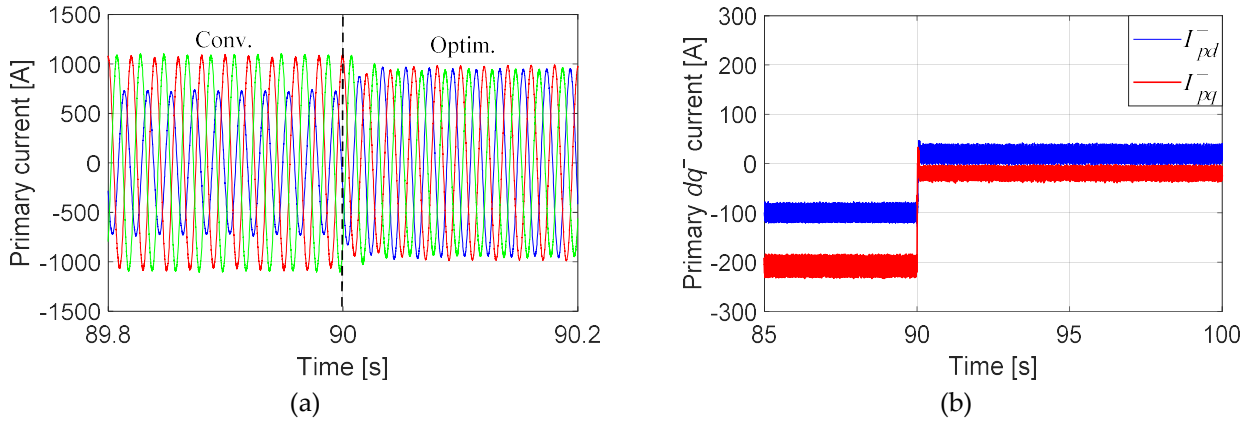
Figure 4.18. Simulation results with the proposed optimal algorithm: (a) primary current; (b) dq components of negative sequence primary current

From Figure 4.19 (a-c), it can be seen that compared to conventional design, the optimized control system results in much smoother operation with oscillations of the torque, reactive and active power all being fairly reduced simultaneously.
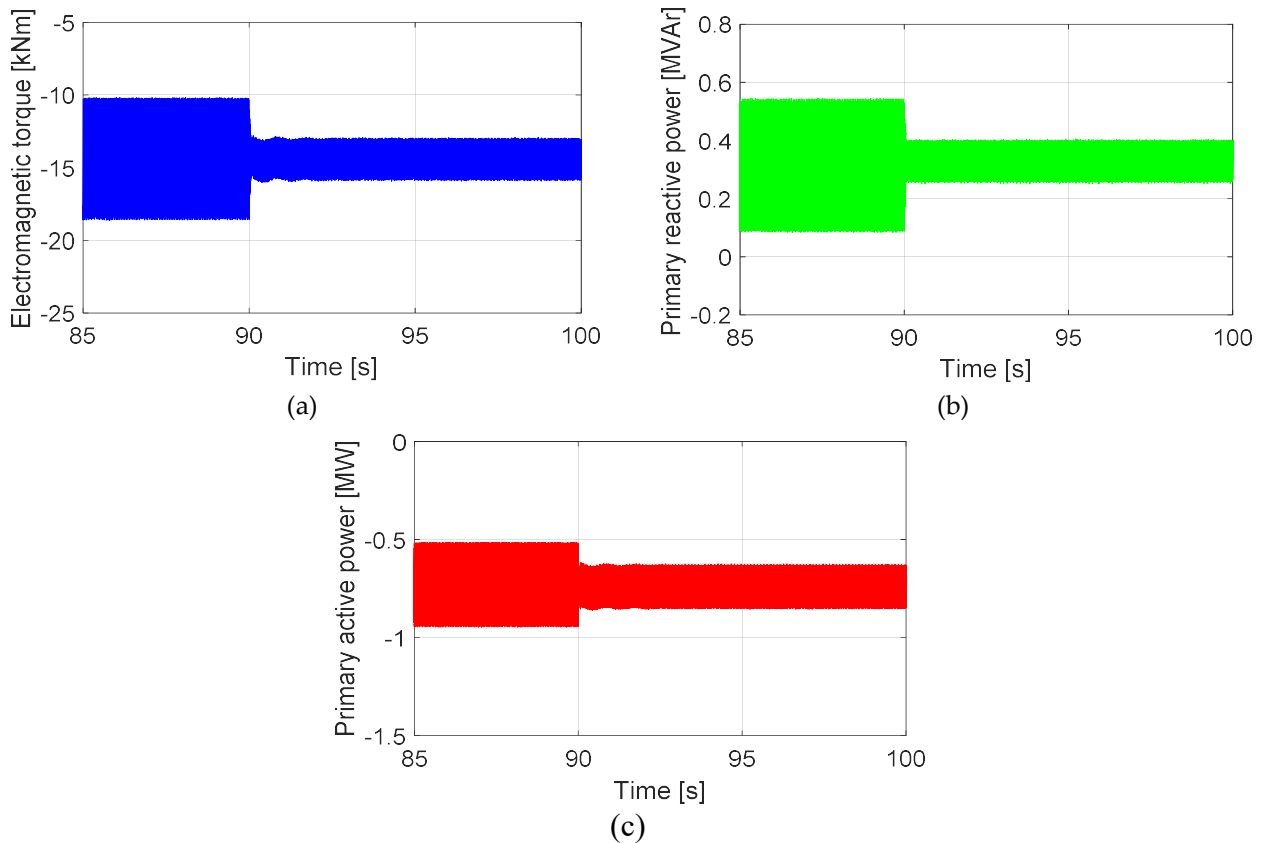
Figure 4.19. Simulation results with the proposed optimal algorithm: (a) electromagnetic torque; (b) primary reactive power; (c) primary active power

64

From Figure 4.20, it can be seen that the ripple of the secondary current is significantly mitigated.
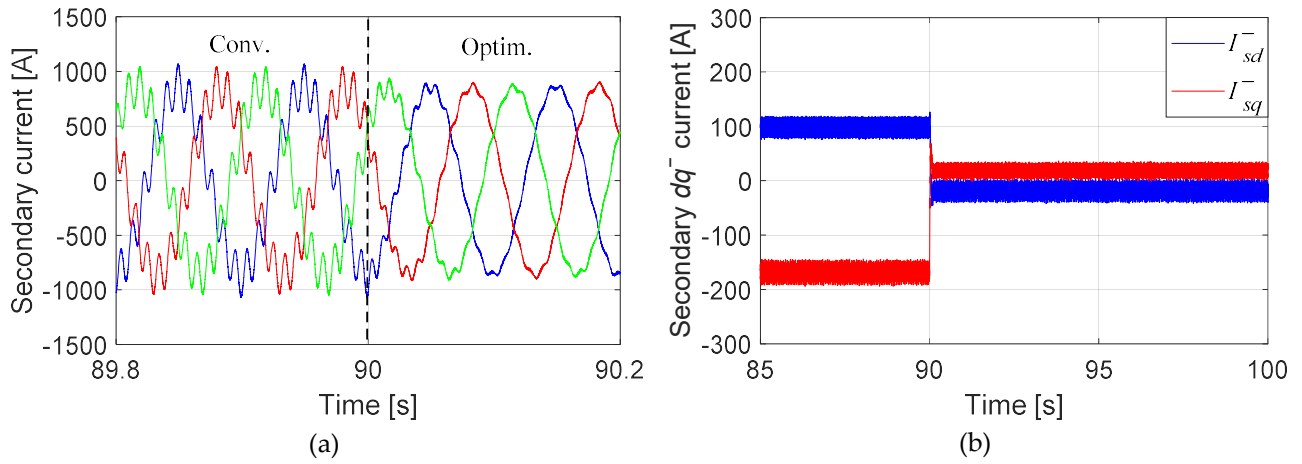
Figure 4.20. Simulation results with the proposed optimal algorithm: (a) secondary current; (b) *dq* components of negative sequence secondary current

A comparison of the different control targets with the proposed optimal control method is summarized in Table 4.3.

Table 4.3. Comparison of the different control targets with the proposed optimal control algorithm

Target	I	II	III	V	Optimum	conventional
I_p unbalance (%)	0.8	11.3	10.3	5	2	24
I_s distortion (%)	4.5	10.3	13.8	0.7	3	22
T_e pulsations (%)	11.2	0.6	24	10.7	5.7	±27
P_p pulsations (%)	14.5	22	0.7	13	11	±28
Q_p pulsations (%)	28	0.4	34	26	9	±42

Chapter 5

Design of a Large Scale BDFRG

5.1 **Introduction**

The rotor flux modulation process makes the BDFRM quite a complex machine to design, probably more than most of the traditional ones [107]. One possible drawback with the BDFRM is the relatively high leakage flux resulting from the flux modulation process by the rotor. The performance of the BDFRM highly depends on the capability of the rotor to modulate stator magnetic fields, by establishing magnetic coupling between the stator windings that otherwise would not interact. Therefore, the rotor design is the most critical and important constraint to be taken care of. Though the salient pole rotor (Figure 5.1) is simple and useful for understanding the BDFRM operating principles, its performance is inferior to an axially and radially laminated rotor [108, 109]. Some of the fundamental design issues such as designing different rotor structures, electromagnetic design issues, stator and rotor pole combinations, loss considerations, etc. have been addressed in[110].

This chapter will provide a brief introduction concerning the BDFRM design aspects. The main dimensions of 8-4-6 poles combination of a 1.5 MW BDFRG will be estimated according to parameters of a small-scale machine, and then the accuracy and effectiveness of the theoretical analysis will be investigated using ANSYS Maxwell software.

| (a) Salient pole rotor | (b) Axially laminated rotor | (c) Radially laminated rotor |
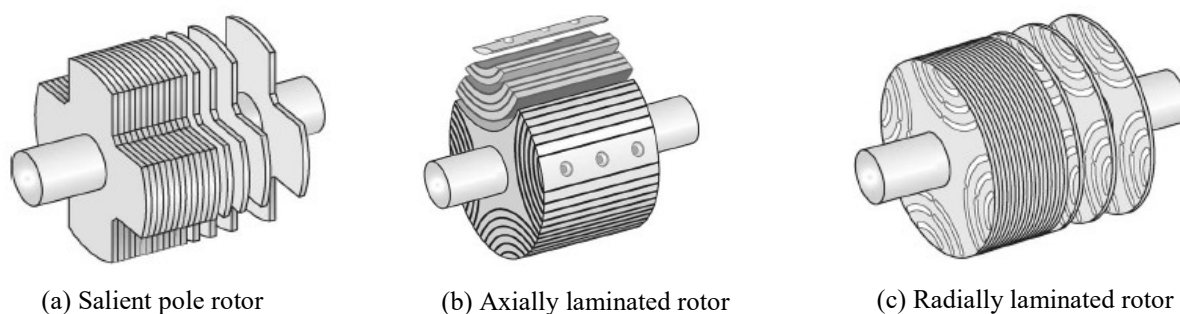
Figure 5.1. Different types of reluctance rotors for the BEDRM (adapted from [111])

5.2 **Air Gap Flux Density**

The air-gap flux density can be obtained using the procedure presented by [112-114] . The flux modulation process is represented assuming that all the flux entering the rotor at a given point θ_1 in the air gap, must leave the rotor at the corresponding opposite flux path end at angle θ_2, without any leakage, as in the geometry shown in Figure 5.2.
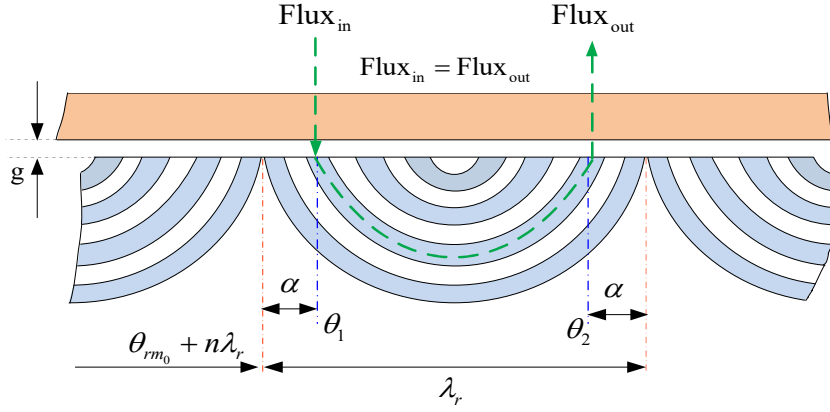
Figure 5.2. Linearized ideal ducted rotor geometry and angles definition

The air-gap flux density may be calculated using the following expression,

$$B(\theta_1) = \frac{\mu_0}{2g}(F_{total}(\theta_1) - F_{total}(\theta_2)),$$

(5.1)

where F_{total} is the total three-phase magnetomotive force and the angles are defined by:

$$\theta_2 = \theta_1 + \lambda_r - 2\alpha,$$

(5.2)

and λ_r is the rotor pole pitch defined as:

$$\lambda_r = \frac{2\pi}{P_r}$$

(5.3)

The angle α is a periodic function with respect to the rotor pole pitch, calculated using:

$$\alpha = \text{mod}(\theta_1 - \theta_{rm_0}, \lambda_r)$$

(5.4)

where θ_{rm0}, is the initial mechanical position of the rotor d-axis (at t=0).

In order to evaluate the coupling factors, the normalized air gap flux density is defined in [112-114] as:

$$\beta(\theta_1) = \frac{B(\theta_1)}{\frac{\mu_0}{g}\hat{F}} = \frac{(F_{total}(\theta_1) - F_{total}(\theta_2))}{2\hat{F}}$$

(5.5)

The normalized air-gap flux density is plotted in Figure 5.3 for the 8/4/6 poles combination

68
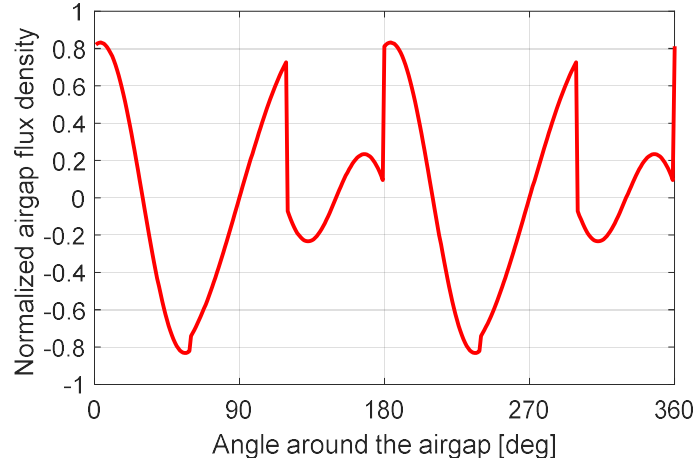
Figure 5.3. Normalized air gap flux density; P_p=8, P_s=4, P_r=6

5.3 **Criteria for Choosing the Number of Poles and Slots**

Selection of the suitable combination of the number of poles depends on many aspects. The most important one is to achieve the coupling conditions for torque production. The authors in [112, 113] proposed a solution to determine coupling factors for different combinations of the pole numbers.

The amplitude of a flux density harmonic of space order *i*, produced as a result of the modulation of the MMF harmonic of space order *j* by the rotor structure, can be defined in terms of a coupling factor C_{ij} between the three phase winding sets:

$$\hat{B}_i = C_{ij} \frac{\mu_0}{g} \hat{F}_j , \qquad (5.6)$$

where C_{ij} is the coupling factor obtained from Fourier analysis:

$$C_{ij} = \sqrt{a_{ij}^2 + b_{ij}^2} , \qquad (5.7)$$

$$a_{ij} = \frac{1}{\pi} \int_0^{2\pi} \beta_j(\theta_m) \cos(\frac{P_i}{2}\theta_m) d\theta_m , \qquad (5.8)$$

$$b_{ij} = \frac{1}{\pi} \int_0^{2\pi} \beta_j(\theta_m) \sin(\frac{P_i}{2}\theta_m) d\theta_m . \qquad (5.9)$$

The resulting coupling factors for several number of poles combinations are presented in Table 5.1

69

Table 5.1. Ideal coupling factors [112]

Number of Poles			Coupling Factors			$\omega_{rm\text{-}sync}$
P_p	P_s	P_r	C_{ss}	$C_{ps} = C_{sp}$	C_{pp}	[rpm]
8	4	2	0.0000	0.0000	0.0000	1500
6	2	4	0.1817	0.3183	0.6061	750
6	4	5	0.3831	0.4677	0.5780	600
10	2	6	0.0865	0.2067	0.5827	500
8	4	6	0.2933	0.4135	0.6034	500
14	2	8	0.0498	0.1501	0.5643	375
12	4	8	0.1817	0.3183	0.6061	375
10	6	8	0.3499	0.4502	0.5900	375
18	2	10	0.0323	0.1169	0.5220	300
16	4	10	0.1216	0.2523	0.5946	300
14	6	10	0.2477	0.3784	0.6081	300
12	8	10	0.3831	0.4677	0.5780	300
22	18	20	0.4454	0.4918	0.5447	150

The results in the above-mentioned references have shown that a 4-pole rotor design has a reduced coupling factor compared to other alternatives. In addition, any saturation induced by the 3rd harmonic of the 2-pole stator winding will cause an unwanted coupling to the 6-pole winding. For these reasons, this design has been avoided by many authors, and the preferred reasonable rotor pole number is commonly taken to be 6.

On the other hand, an inappropriate selection of stator and rotor slot number combinations produce undesirable torque and voltage harmonics in electrical machines. To minimize these unwanted effects, suggested values of rotor duct and stator slot number for synchronous reluctance machines are presented in [109]. Additional constraints for the BDFRM are discussed in [112] due to the fact that there are two MMF sources with different pole numbers. The authors proposed the following equations to assess the slotting harmonics:

$$\left.\begin{array}{l} h_{s_p} = P_p(1 \pm m\dfrac{N_s}{P_p}) \\[2mm] h_{s_q} = P_s(1 \pm m\dfrac{N_s}{P_s}) \end{array}\right\}, \tag{5.10}$$

$$h_{r_p} = P_p(1 \pm n \frac{N_r}{P_p}) \left.\begin{matrix} \\ \\ \\ \\ \end{matrix}\right\}$$

$$h_{r_q} = P_s(1 \pm n \frac{N_r}{P_s})$$

$$\tag{5.11}$$

where h_{sp}, h_{sq}, h_{rp} and h_{rq} are space harmonics in primary and secondary winding due to stator and rotor slots, respectively, N_s is the number of stator slots, N_r is the number of rotor ducts, and m and n are arbitrary positive integers. Another important consideration is that the number of rotor ducts (N_r) should be an integer multiple of the rotor pole number.

Table 5.2 shows the parameters chosen based on the discussion in the preceding section. These parameters are fixed and will not be considered as optimization variables.

Table 5.2. Variables chosen by the designer

Description	Value
Number of stator slots N_s	72
Number of rotor ducts N_r	66
Stator poles primary winding P_p	8
Stator poles secondary winding P_s	4
Rotor poles P_r	6
Synchronous speed [rpm]	500
Slots per pole per phase primary winding $N_{s\text{-}p}$	3
Slots per pole per phase secondary winding $N_{s\text{-}s}$	6

5.4 Dimension Scaling

The main dimensions of the designed 1.5 MW BDFRG are estimated based on the dimensions of a base small-scale design according to the following procedure.

- The air gap δ of a 50Hz asynchronous machine can be calculated in mm as a function of power p using the equation [115]:

$$\delta = 0.18 + 0.006 p^{0.4} \text{mm} \tag{5.12}$$

- The air-gap flux density is assumed to be the same for the base ($B_{\delta b}$) and designed ($B_{\delta d}$) machines ($B_{\delta d} = B_{\delta b}$)

$$B_\delta \approx \frac{NI}{\delta} \Rightarrow N_d = \frac{\delta_d I_b}{\delta_b I_d} N_b \tag{5.13}$$

It is worth noting that scaling with constant flux and current density requires improved cooling in the new design, as losses are proportional to machine volume, while the cooling surface is proportional to the machine area.

- The current density J is assumed to be unchanged ($J_d = J_b$)

$$J = \frac{NI}{S_{slot}} \Rightarrow S_{slot\_d} = \frac{N_d}{N_b}\frac{I_d}{I_b}S_{slot\_b} \tag{5.14}$$

Figure 5.4 shows a cross-section of the slots with the main slot and conductor dimensions denoted.
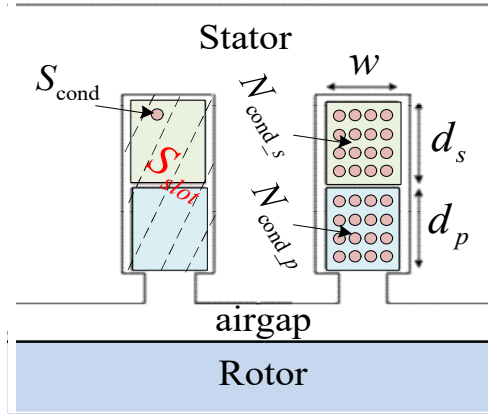
Figure 5.4. Cross-section view of the slots

- If the induced voltage is assumed to be sinusoidal, the RMS value of the air-gap voltage is obtained according to (5.15):

$$V \sim B_\delta D\ell N \tag{5.15}$$

Considering the assumption $B_{\delta d} = B_{\delta b} = B_\delta$, the product of the inner diameter (D) and the effective length (ℓ) of the stator is obtained:

$$(D\ell)_d = \frac{V_d}{V_b} \times \frac{N_b}{N_d}(D\ell)_b \tag{5.16}$$

The value of $D^2\ell$ can also be estimated using (5.17) [116]:

$$\overbrace{P_p + P_s}^{P_{rated}} = \pi(D^2\ell)\frac{\omega_p}{\sqrt{2}}[\frac{A_{lp}B_p}{p_p}\cos\phi_p + \frac{\omega_s A_{ls} B_s}{\omega_p p_s}\cos\phi_p]\eta, \tag{5.17}$$

where $B_{p,s}$ and $A_{lp,s}$ represent peak flux density and rms electric loading (A/m) of the primary and secondary windings, respectively.

The average of total tangential stress (σ_{tan}) for both windings can be obtained as:

$$\sigma_{tan} = \frac{A_{lp}B_p}{\sqrt{2}} + \frac{A_{ls}B_s}{\sqrt{2}} \tag{5.18}$$

The torque produced by the rotor may be written as:

$$T_e = \pi \frac{D^2}{2} \ell \sigma_{tan} \tag{5.19}$$

Equation (5.19) gives an initial estimation for the volume of the rotor required to produce a certain torque T_e.

The Specific electrical loading (linear current density) A_l of the windings, as well as the conductor current density J, must also be assessed, since these quantities describe the electrical loading of the machine [115].

$$J = \frac{I_{rms}}{S_{cond}} \quad [\text{A/mm}^2], \tag{5.20}$$

$$A_l = \frac{I_{rms} N_s N_{cond}}{\pi D_{gap}}, \tag{5.21}$$

where N_{cond} is the number of conductors per slot, D_{gap} is the air-gap diameter.

The calculated values of the specific electric loading, current density, and average tangential stress are presented in Table 5.3.

Table 5.3. Specific electric loading and current density

Parameter	Description	Value
J_p	Current density of the primary [A/mm2]	7
J_s	Current density of the secondary [A/mm2]	4
A_{lp}	Linear current density(primary) [kA/m]	33
A_{ls}	Linear current density (secondary) [kA/m]	26
σ_{tan}	Average tangential stress [kPa]	25

According to (5.1)-(5.5), the air-gap flux density of the machine is calculated at rated conditions, where the flux modulation process by the rotor can be observed as in Figure 5.5.
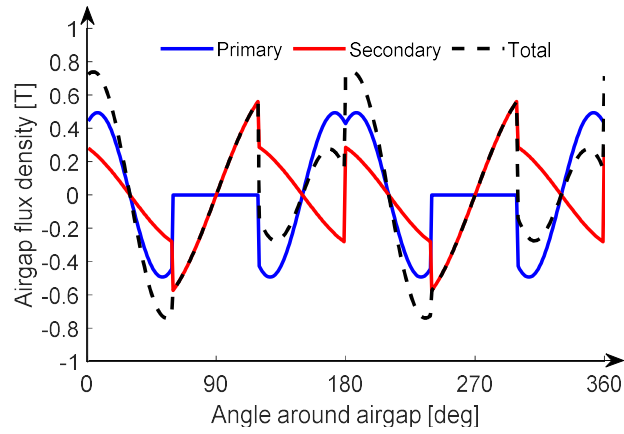
Figure 5.5. Airgap flux density due to primary and secondary currents

5.5 **Finite Element Analysis Results**

Special machines can be modeled using the ANSYS Maxwell platform. This software package provides a graphical interface to display machine models and simulation results, as well as parametric evaluation and optimization. It is possible to download the model into other platforms such as Simplorer for system simulation, vibration and noise analysis, or thermal analysis of a machine. It is also possible to develop electric circuits using a circuit editor. Looking into availability, operational simplicity, and other features, ANSYS Maxwell 2D is a preferable choice for the development of numerical models and simulation studies of BDFRM.

The model is developed with two independent windings embedded in 72 stator slots. The model geometry is constructed in Ansys Maxwell 2D considering design dimensions, specific materials, motion setup, and mesh operations, etc. The excitation voltage is assigned to the stator winding terminals using an external circuit editor as shown Figure 5.6.
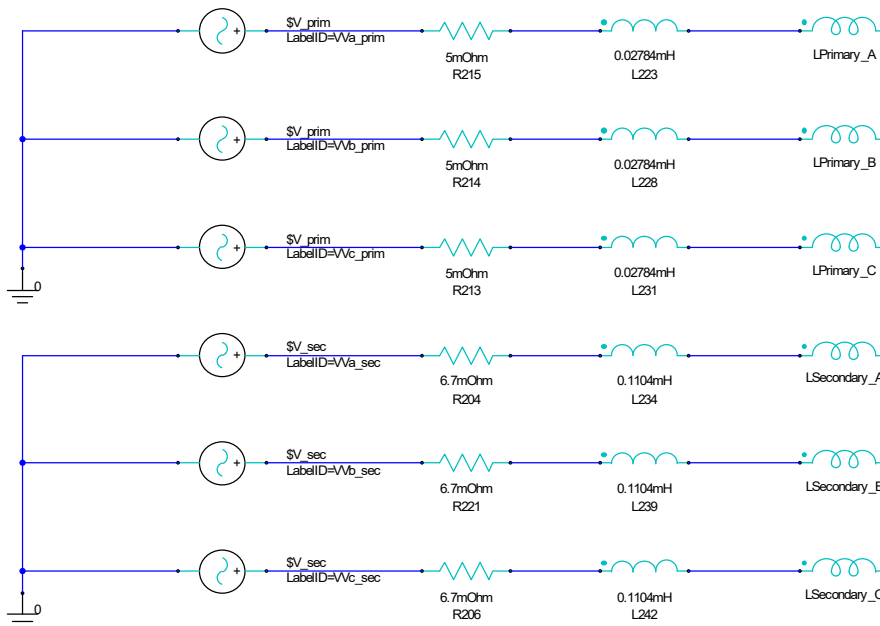
Figure 5.6. Primary and secondary end connections using Maxwell Circuit Editor

The performance of the BDFRM can be evaluated from different plots such as flux distribution, flux density distribution, voltage, current waveforms, moving torque, etc.

Figure 5.7 and Figure 5.8 show a cross-sectional view of the design with flux lines, density, and distribution. The flux density shown in Figure 5.8 indicates that the maximum flux density in the stator teeth, stator yoke, and rotor yoke flux densities are less than 2 T.
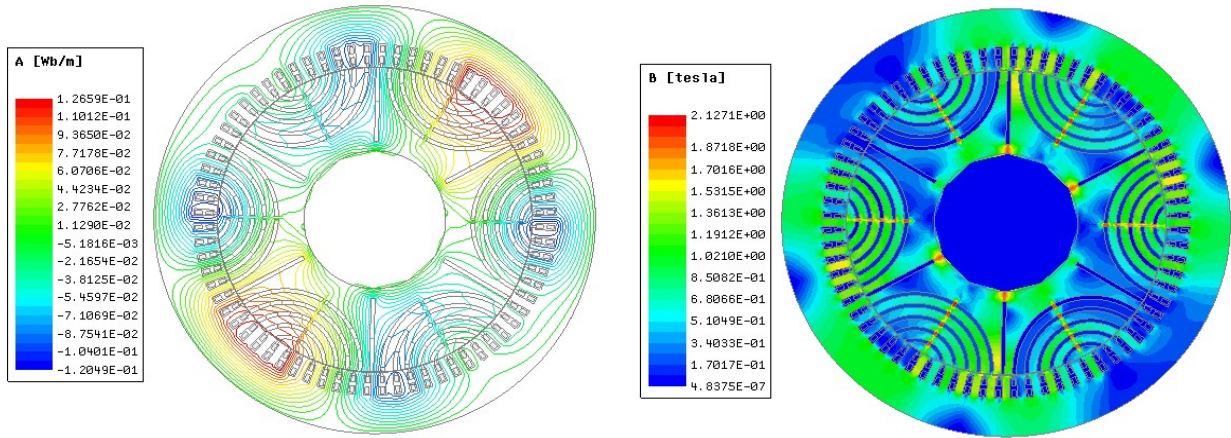
Figure 5.7. Flux distribution under dual excitation

Figure 5.8. Flux density distribution under dual excitation

The primary and secondary winding currents when both windings are excited with 50 Hz sinusoidal voltages and different phase shifts are shown in Figure 5.9, while the corresponding moving torque developed by the generator is presented in Figure 5.10.
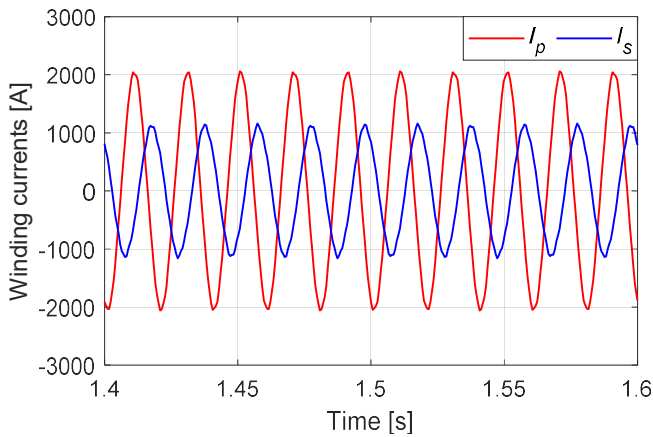
Figure 5.9. Winding current waveforms
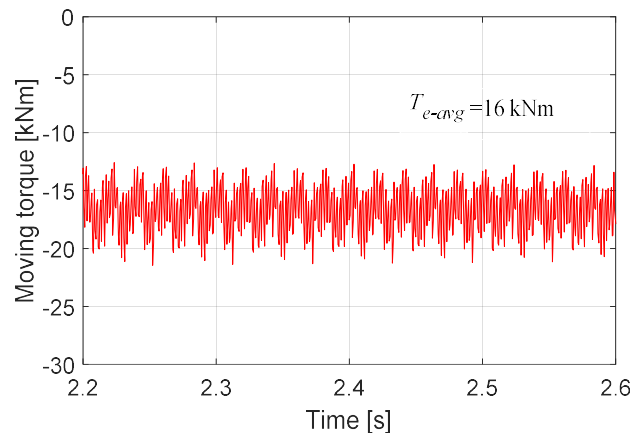
Figure 5.10. Moving torque developed by the generator

The produced moving torque contains a certain amount of ripple (Figure 5.10), which can be reduced by optimizing the rotor structure and parameters of the stator core and windings. However, the main target of the optimal design is not to reduce the torque ripple but rather to satisfy other requirements, most notably the output power and efficiency.

Table 5.4 presents initial design dimensions for a 1.5 MW BDFRG that are calculated according the previous discussion.

Table 5.4. Initial design dimensions

Parameter	Description	Value (mm)
D_o	Outer diameter of stator (mm)	1400
D	Inner diameter of stator (mm)	1000
ℓ	Length of stator core (mm)	1000
δ	Length of air gap (mm)	2
D_{ri}	Inner diameter of rotor (mm)	450
Sl_o	Slot opening (mm)	8
S_y	Stator yoke length (mm)	250
S_{tw}	Stator tooth width (mm)	25

5.6 Electrical parameters

The phase resistances for each winding are calculated based on the machine dimensions and the number of turns considering copper conductors as follows:

$$R_{p,s} = \rho(1+\alpha_t(t_{stat}-t_{amb}))\frac{L_{wire_{p,s}}}{S_{cu_{p,s}}}, \tag{5.22}$$

wher; α_t is the temperature coefficient, t_{stat} is the considered temperature in stator windings, ρ is the copper resistivity, t_{amb} is the ambient temperature, L_{wire} is the total wire length and S_{cu} is the conductor cross-sectional area [115].

The winding inductances are calculated using the winding function theory [26]. Details on the calculation of inductances, as well as resistances, are outlined in the Appendix A. The calculated values of electrical parameters are reported in Table 5.5.

Table 5.5. Electrical parameters value of the BDFRG

Parameter	Description	Value
R_p	Primary resistance (mΩ)	5.103
R_s	Secondary resistance (mΩ)	6.827
L_p	Primary inductance (mH)	2.237
L_s	Secondary inductance (mH)	4.4334
L_{ps}	Mutual inductance (mH)	2.924

Chapter 6

Maxwell/ Simplorer /Simulink Co-Simulation and Experimental Verification

6.1 **Maxwell/ Simplorer /Simulink co-simulation**

In order to examine and validate the optimized control, a FEM model of a small-scale BDFRG which has been built using Ansys Maxwell is imported to Simplorer for coupling to the Simulink control system. The control system model built in Simulink is then added to Simplorer. The interface between Ansys and Simulink was established and implemented using a special S-Function known as "AnsoftSFunction".

6.1.1 Coupling of FEM Model and Control System with Simplorer

Once the generator is built in Maxwell and analyzed, it is then prepared for co-simulation with Simplorer as follows:

- On the design Setting pop-up window and under Advanced Product Coupling tab, Transient-Transient link with Simplorer should be enabled.
- In Simplorer, transient cosimulation is added (Simplorer Circuit→SubCircuit→Maxwell Component→Add Transient Cosimulation)
- In the Transient-Transient coupling window that appears, the Maxwell project that was saved before is selected.

The next step is to link the control system that was verified using Simulink to the Simplorer. The interface between Ansys and Simulink was established and implemented using a special *S-Function* known as "*AnsoftSFunction*". The *S*-function's objective is to receive the currents, voltages, and generator speed from the Maxwell model, and to transfer the control signals to the Simplorer [117, 118].

The design parameters of a 1.5 kW BDFRG that is used in the co-simulation are listed in Table 6.1.

Table 6.1. Design parameters used in co simulation

Parameter	Description	Value
D_o	Outer diameter of stator (mm)	235
D	Inner diameter of stator (mm)	144
ℓ	Length of stator core (mm)	85
δ	Length of air gap (mm)	0.5
D_{ri}	Inner diameter of rotor (mm)	65
$N_{t\text{-}p}$	Number of turns per slot (primary)	56
$N_{t\text{-}s}$	Number of turns per slot (secondary)	39

The complete model of Ansys and Simulink control structure is shown in Figure 6.1
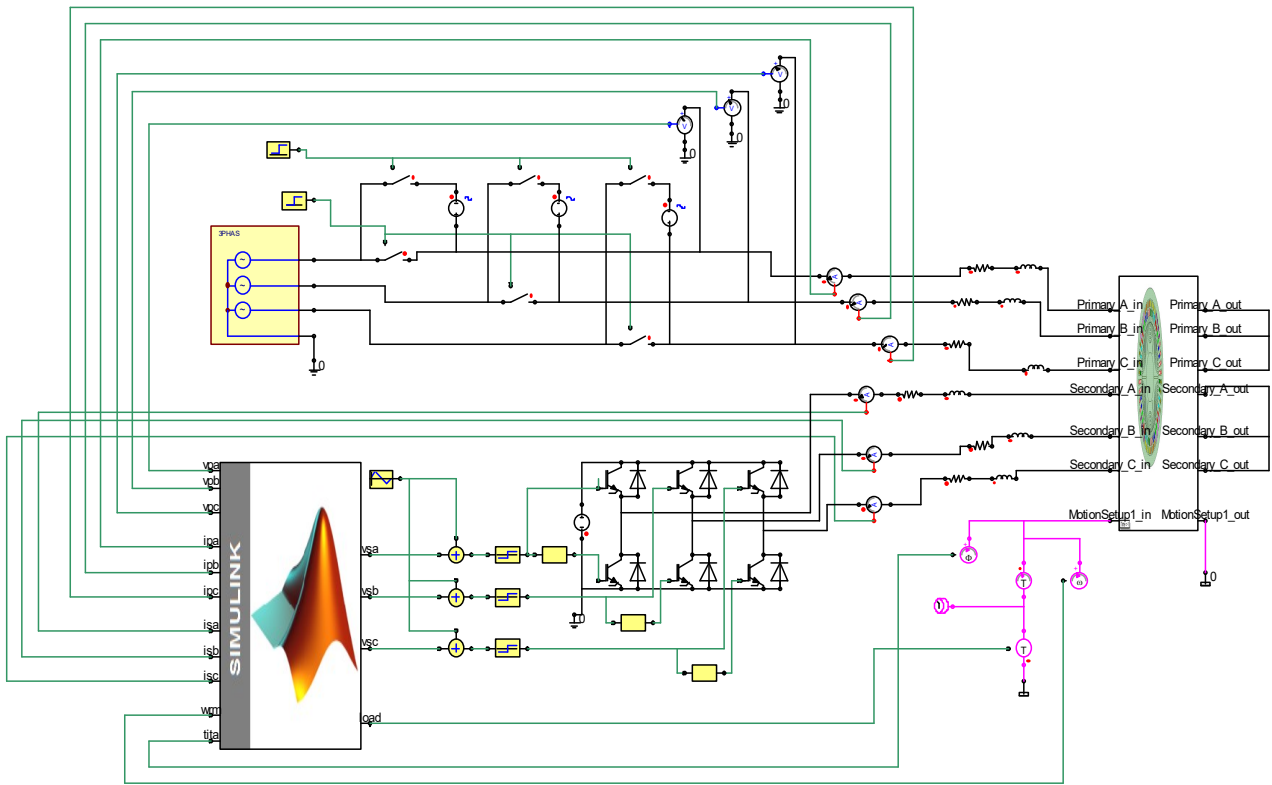
Figure 6.1. Coupling of Ansys Maxwell model with Simulink using Simplorer

Despite many advantages of co-simulation, long simulation time is the main drawback [119, 120], especially when considering the transient behavior of large machines with high moment of inertia which are commonly used in wind power applications. In order to get an accurate simulation, the time step should be as low as possible. However, the lower the time step gets, the longer time the simulation will take. Therefore, a trade-off between accuracy and computation time should be taken into consideration.

The simulation time and step size of simulation model in this article are coherent with Simplorer, whereas the step size in Maxwell is smaller than in Simplorer.

6.1.2 Co-Simulation Results

In order to demonstrate the performance of the optimized control under unbalanced grid conditions, the connection between Simulink and Simplorer is completed by the *S*-Function module in Simulink. The measured signals in Simplorer (such as rotor speed, rotation angle, primary/secondary currents, and grid voltage) are transmitted to Simulink. After being processed by the control algorithm, the reference voltage for the secondary side is transmitted back to the Simplorer as shown in Figure 6.1.

The following test is performed on a 1.5 kW BDFRG: Initially, the system runs under balanced conditions with the BDFRG being started as a slip ring induction machine (i.e. with the shorted secondary winding). After reaching the steady-state, the conventional FOC is enabled; the reference speed of 600 rmp in super-synchronous generator mode is required. After reaching steady state, 10% of negative sequence voltage is instigated at 2 s, while the auxiliary one (i.e. negative sequence

current controller) is disabled. The auxiliary controller is enabled at 2.5 s and consequently the negative sequence reference currents are generated.

The system response for the optimized control design to a given period of unbalanced operation is shown in Figure 6.2
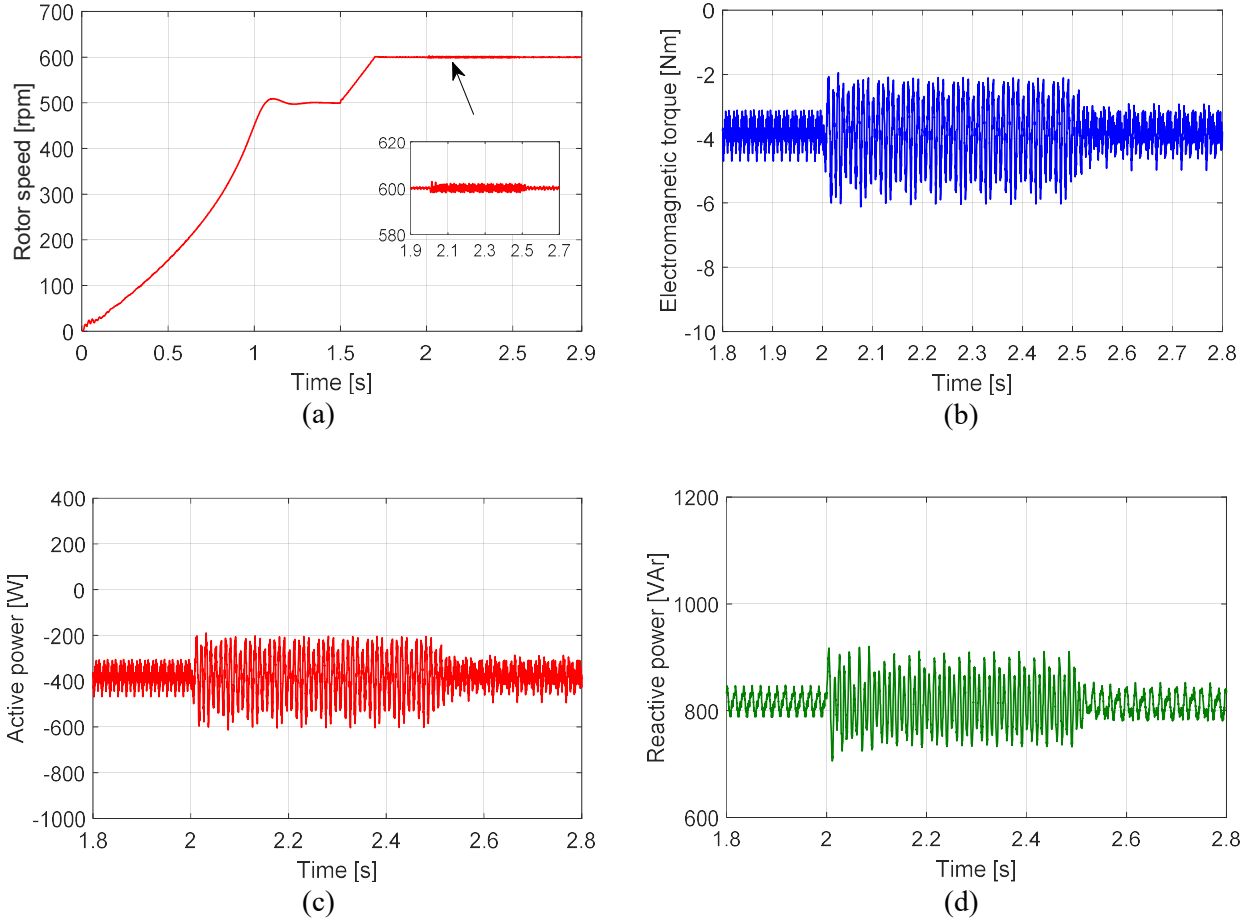
Figure 6.2. Performances of the control system for 10% grid voltage unbalance with optimized control: (a) Speed profile, (b) Electromagnetic torque, (c) Active power, and (d) Reactive power

Obviously, with the optimized control, the electromagnetic torque and active /reactive power pulsations are simultaneously eliminated as shown in Figure 6.2.

It can also be seen that the proposed optimal control algorithm improves the performance of the BDFRG by mitigating the negative sequence components of the primary and secondary currents and maintaining acceptable limits for the currents' waveform as clearly observed in Figure 6.3.

(a)

(b)
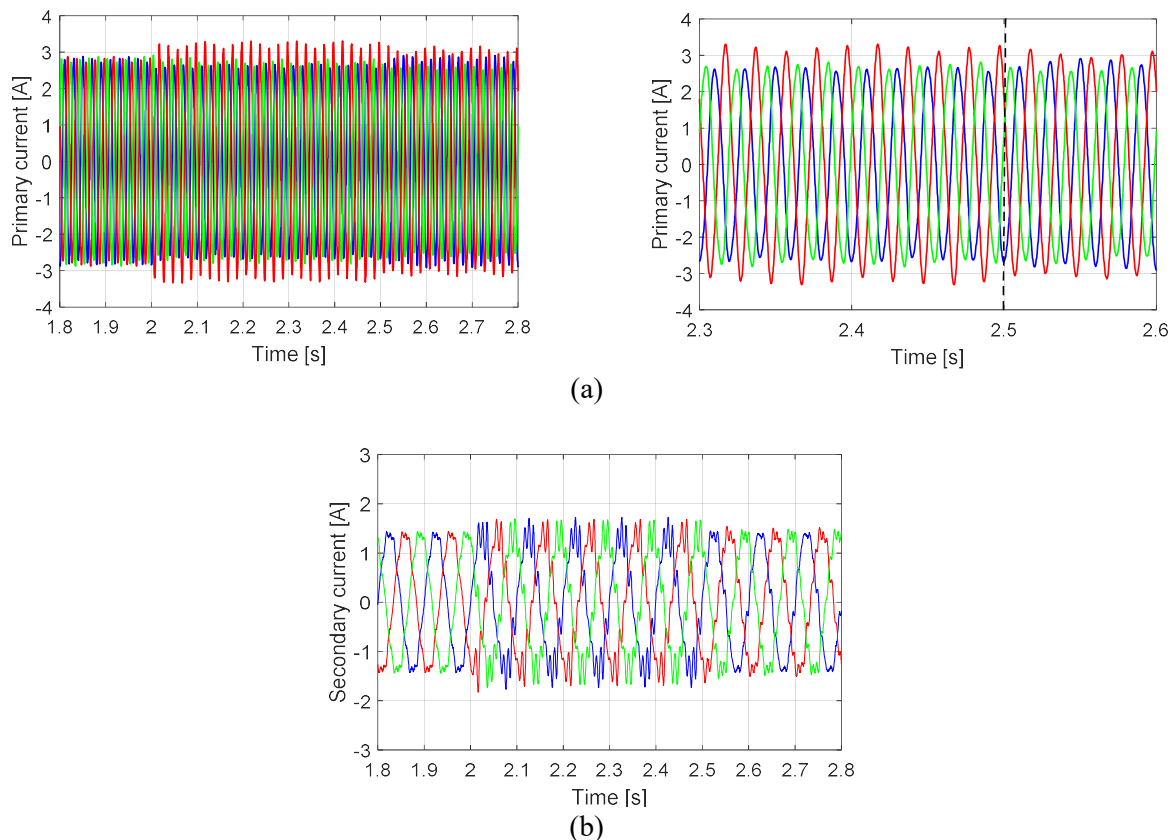
Figure 6.3. Simulation results of co-simulated BDFRG for 10% grid voltage unbalance with optimized control: (a) Primary current, and (b) Secondary current

6.2 **Experimental Verification**

In order to validate the control algorithm in a more practical way, a Hardware-In-the-Loop (HIL) test platform has been developed and used. The block diagram of a HIL-based setup is displayed in Figure 6.4.

Thorough and reliable tests are necessary to verify and validate the improved control. HIL testing is a technique where real signals from a controller are connected to a test system that simulates actual physical systems in real time, essentially "tricking" the controller into thinking it is in the assembled product. A great number of possible scenarios can be easily and safely run through to properly test and adjust the controller without the cost and time associated with actual physical tests.

Generally, HIL can provide many advantages such as [121]:

- Reduced testing cost: the high cost of executing tests on complex machinery can justify substantial investment in HIL.
- Reduce risks associated with failure: control system failure can lead to destroying equipment or presenting safety hazards. HIL can be used to validate controllers before running with real physical equipment. This can be used at the start of the project to validate a new controller.
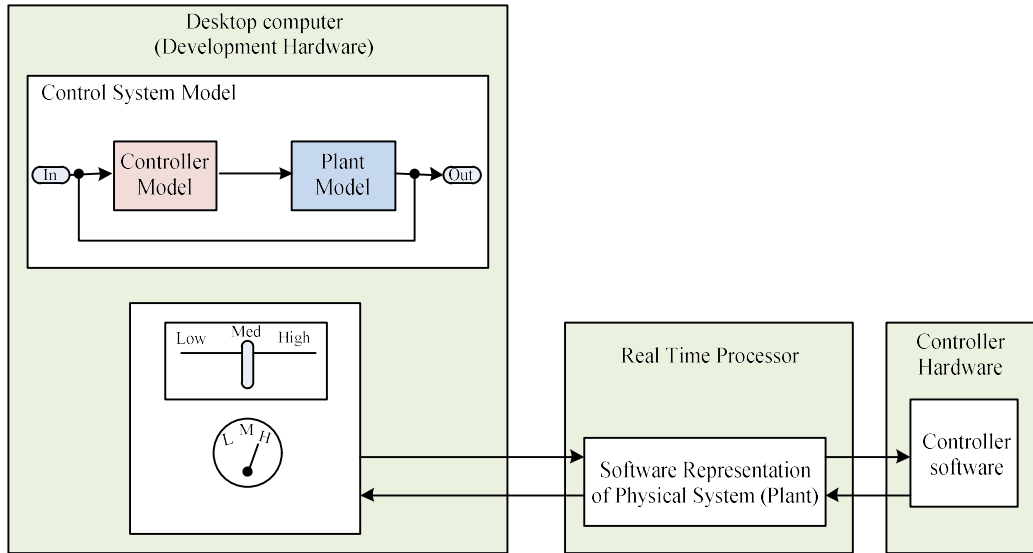
Figure 6.4. Basics of Hardware-In-The-Loop simulation

The real-time performance of the developed control algorithm of the 1.5 MW BDFRG shown in Figure 6.6 has been examined on the HIL system shown in Figure 6.5, where the C-code generated from the Simulink® model is compiled in dSPACE® [122] using the Real-Time Workshop® and run at 10 kHz switching rate of the space-vector-pulse-width-modulated (SVPWM) power converter.
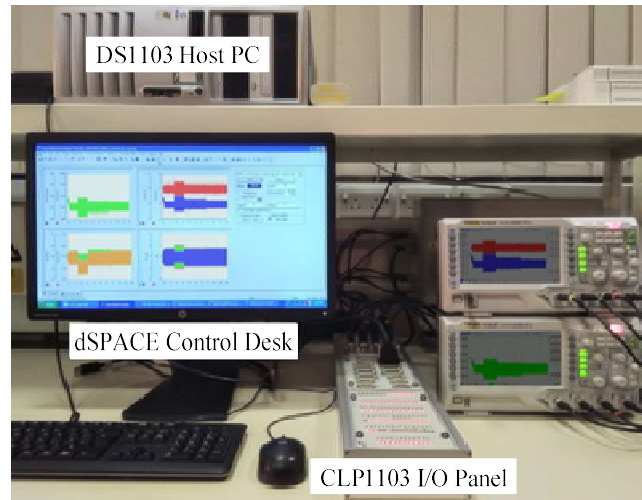
Figure 6.5. HIL laboratory setup for the BDFRG control real-time simulation

The dynamic model of the BDFRG-based WECS shown Figure 6.6 is implemented in the PowerPC 750GX® processor at 100 µs sampling time.

The auxiliary controller is added to the positive sequence controller to improve the BDFRG operational characteristics by generating appropriate negative sequence *dq* secondary current references. The following results demonstrate the characteristics of the primary/secondary currents, electromagnetic torque, and active/reactive powers. Initially, the system runs under balanced conditions with the BDFRG being started as a slip ring induction machine (i.e. with the shorted secondary winding).
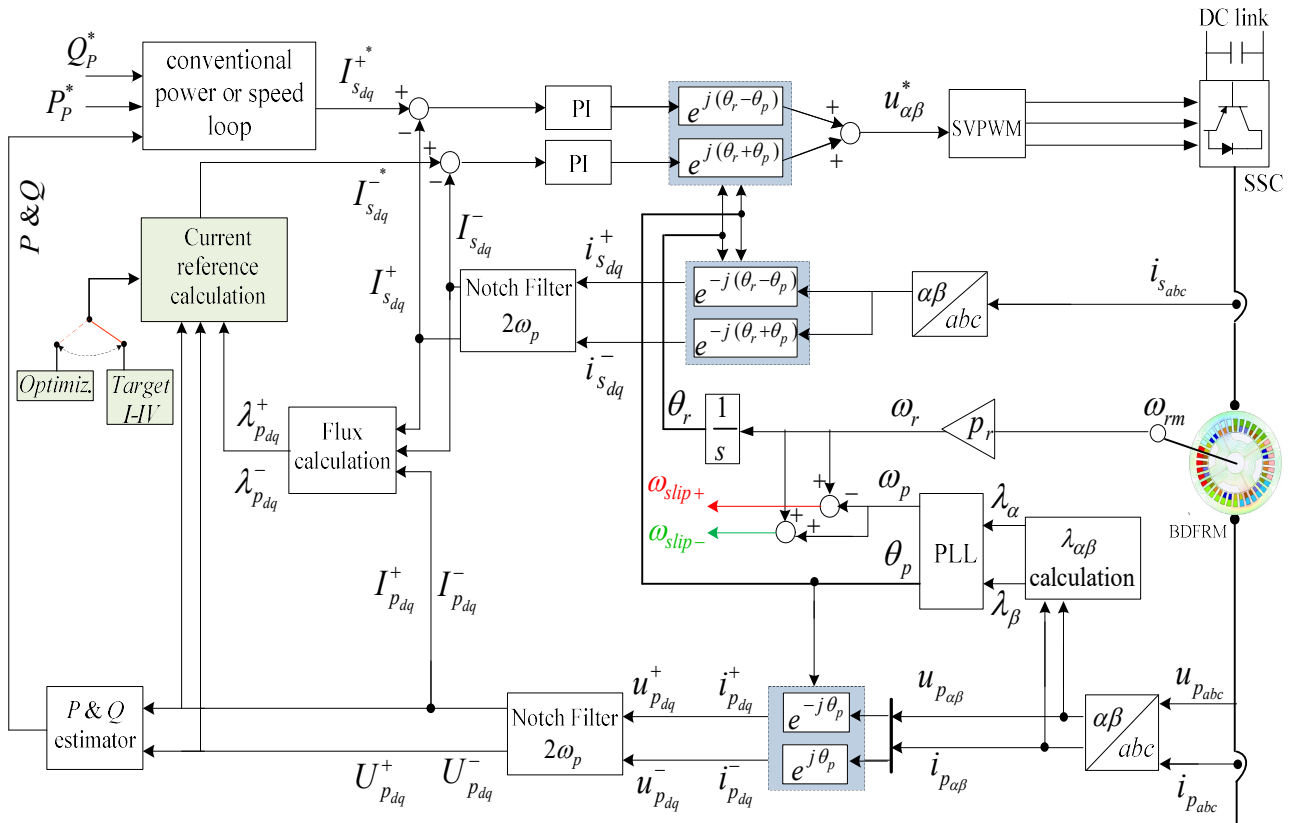
Figure 6.6. A block diagram of the control strategies under unbalanced grid voltage conditions

After reaching steady-state, the period with implemented control algorithm is divided into four stages:

- Between 40 and 50s: grid voltage is balanced with a positive sequence controller applied.
- Between 50 and 60s: grid voltage is unbalanced with a positive sequence controller.
- Between 60 and 80s: grid voltage is unbalanced with the simultaneous presence of negative sequence controller with different targets.
- Between 80 and 100s: grid voltage unbalance is terminated, and the negative sequence control still existing.

The performance of the system using the auxiliary controller that is aimed to eliminate negative sequence primary current is shown in Figure 6.7. It can be seen from Figure 6.7(b) that the negative sequence currents are completely controlled. From Figure 6.7(d-f) it can be also observed that the BDFRG generation system during voltage unbalances is improved by choosing appropriate PI controller gains, where the amplitude of negative sequence secondary current is decreased and the oscillatory components of torque active/reactive powers are reduced.
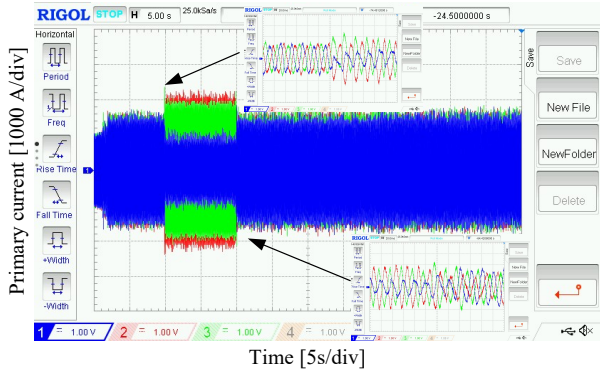
(a)
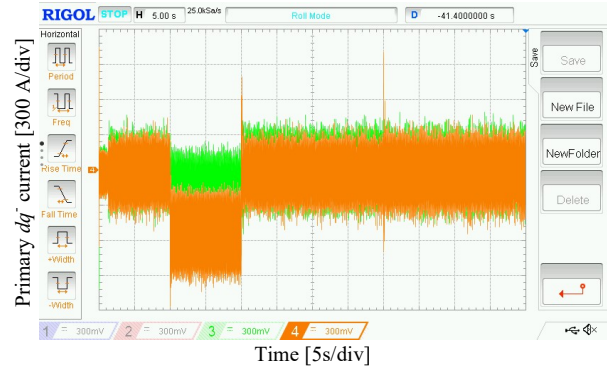
(b)
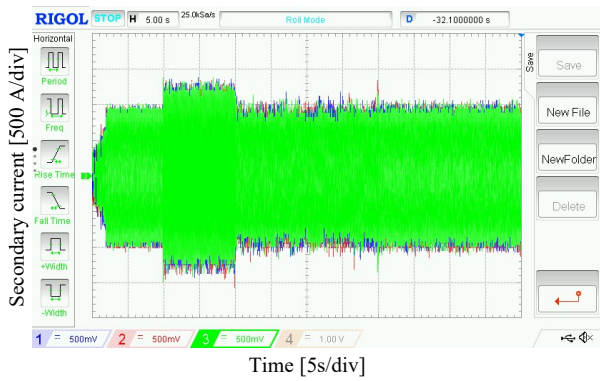
(c)
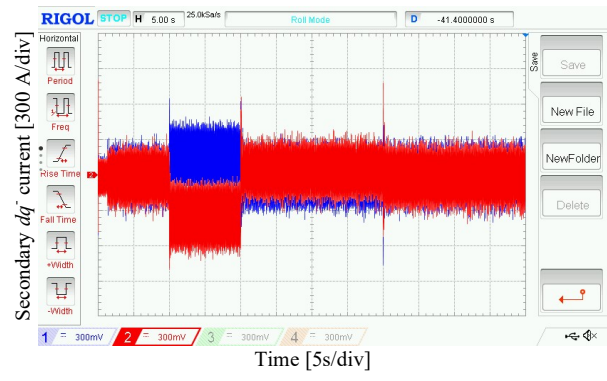
(d)
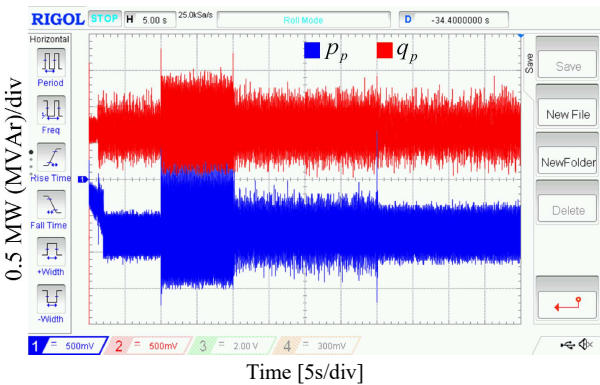
(e)
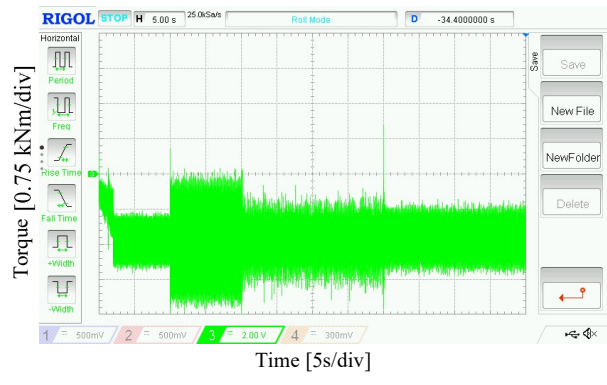
(f)

Figure 6.7. Real-time performance of the designed controller to eliminate the negative sequence primary current: (a) Primary current; (b) Primary negative dq current components; (c) secondary current; (d) secondary negative dq current components; (e) Primary active and reactive power ; (f) Electromagnetic torque

Under unbalanced conditions, the secondary current contains both the 10 Hz fundamental component (positive slip 60–50 Hz) and the 110 Hz harmonic component (negative slip 60 Hz + 50 Hz). The performance of the system using the designed auxiliary controller which is aimed at eliminating negative sequence secondary currents is shown in Figure 6.8. As illustrated in Figure 6.8(d), the secondary current immediately becomes harmonic free. Nevertheless, the effect of the negative sequence components of the grid voltage still appears on the primary current and consequently on the electromagnetic torque and active power, as illustrated in Figure 6.8 (c-f).
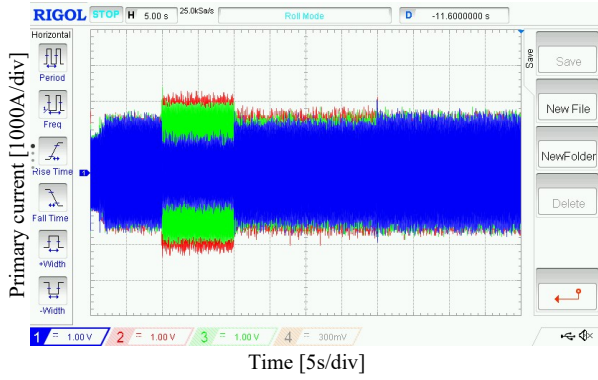
(a)
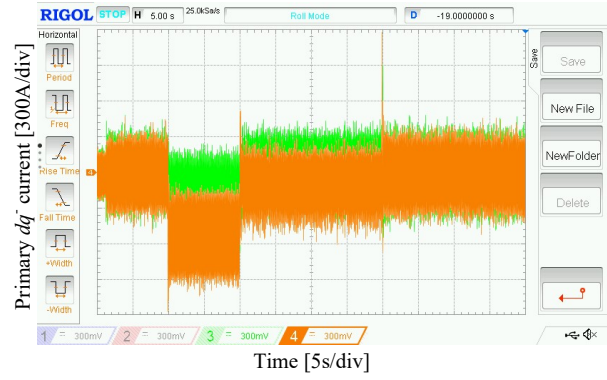
(b)
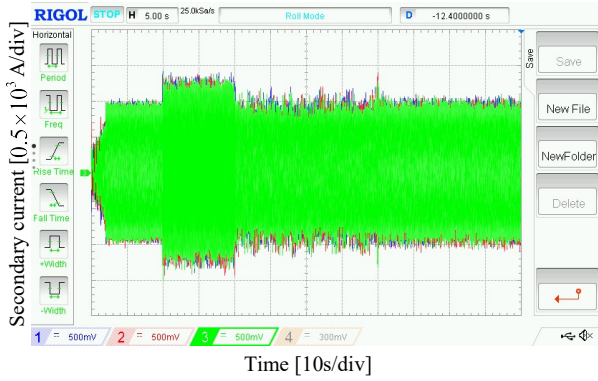
(c)
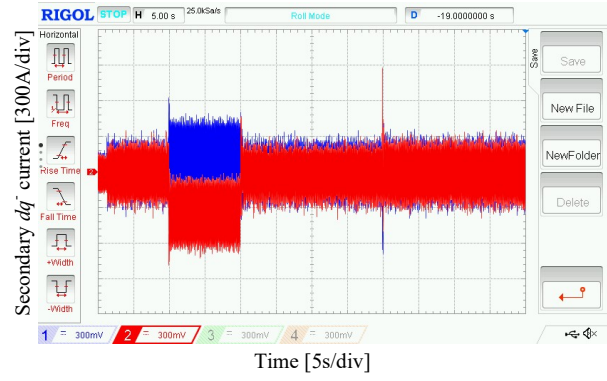
(d)
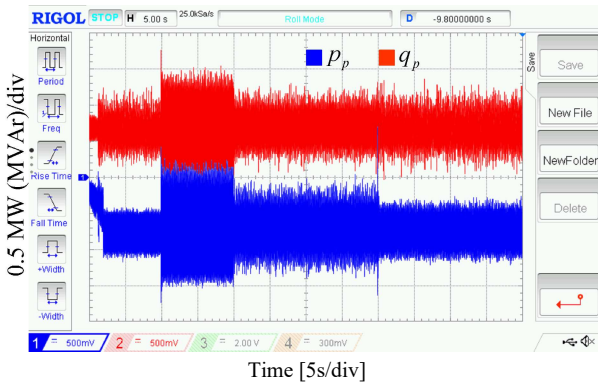
(e)
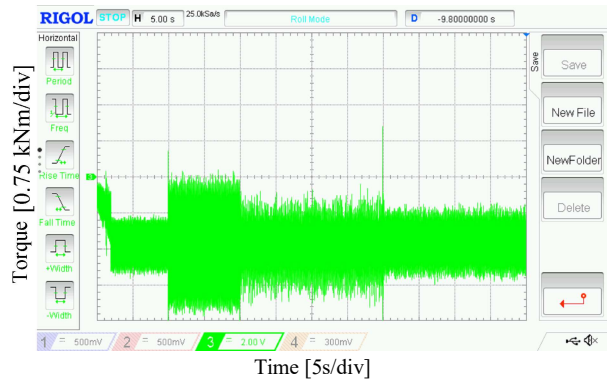
(f)

Figure 6.8. Real-time performance of the designed controller to eliminate the negative sequence secondary current: (a) Primary current; (b) Primary negative dq current components; (c) secondary current; (d) secondary negative dq current components; (e) Primary active and reactive power ; (f) Electromagnetic torque

Figure 6.9 illustrates the performance of the system using the designed auxiliary controller that is aimed to eliminate torque oscillatory components. It can be observed that the BDFRG generation system is improved by reducing the torque oscillations, which are the most concerning issue during grid voltage unbalance [67]. According to (4.21) and (4.23), the primary reactive power pulsations would also be suppressed. On the other hand, the effect of the negative sequence on the other components (i.e. primary current, secondary current, active and reactive power) could not be eliminated as shown in Figure 6.9 (a-e).
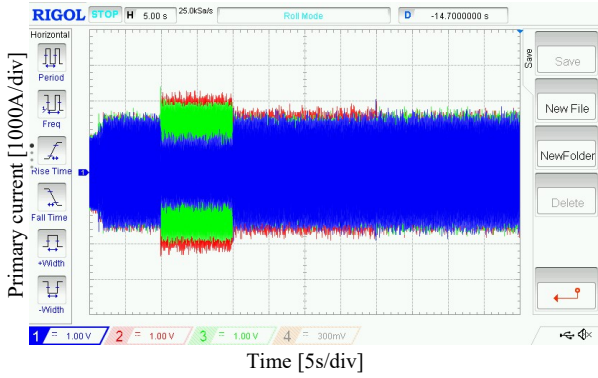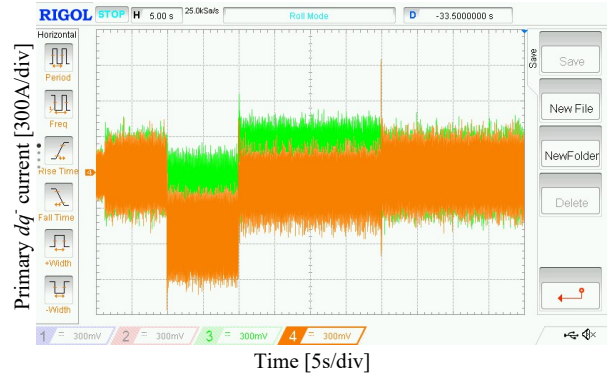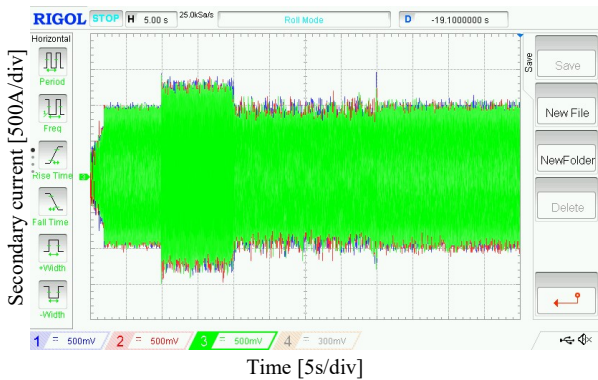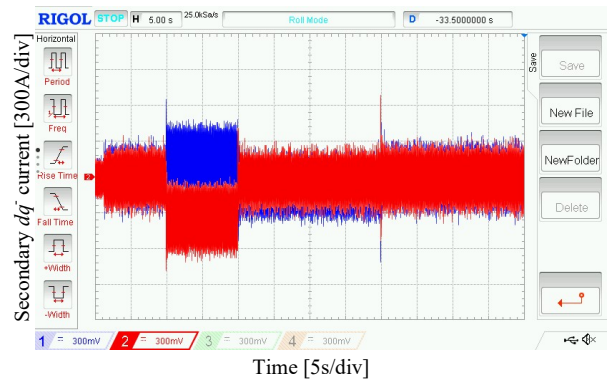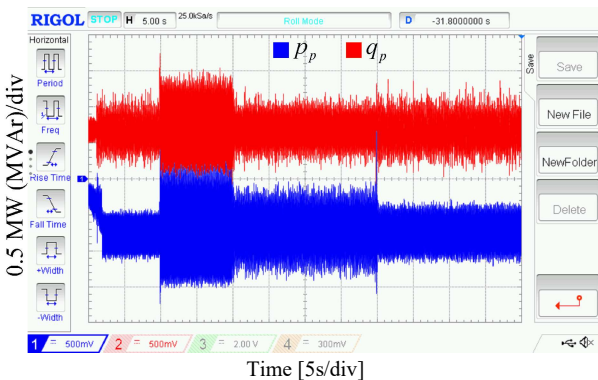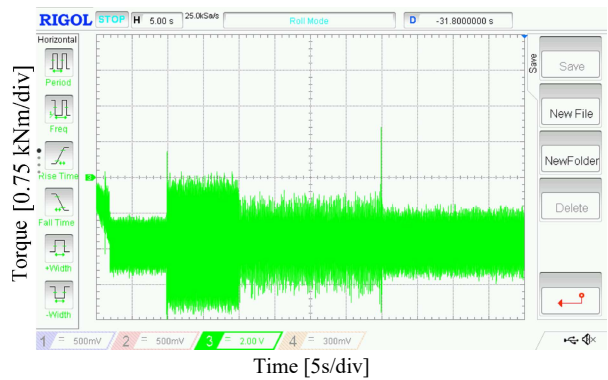
Figure 6.9. Real-time performance of the designed controller to eliminate torque pulsations: (a) Primary current; (b) Primary negative dq current components; (c) secondary current; (d) secondary negative dq current components; (e) Primary active and reactive power ; (f) Electromagnetic torque

Reducing the primary active power pulsations is achieved by using the auxiliary controller that is aimed to eliminate the primary active power pulsations as shown in Figure 6.10(e). It can be seen from Figure 6.10 that the influence of the negative voltage sequence still existed on the torque, reactive power, primary and secondary currents
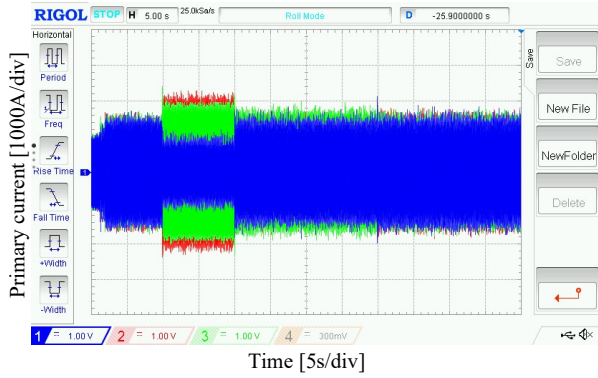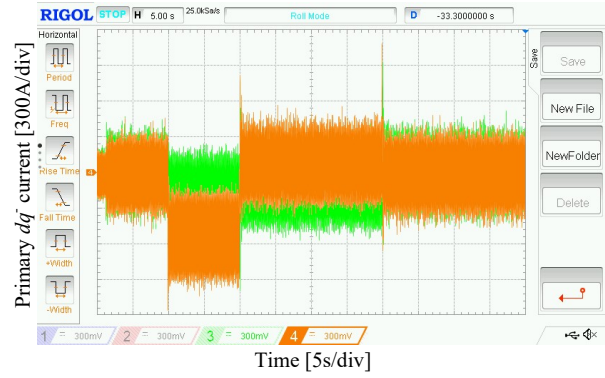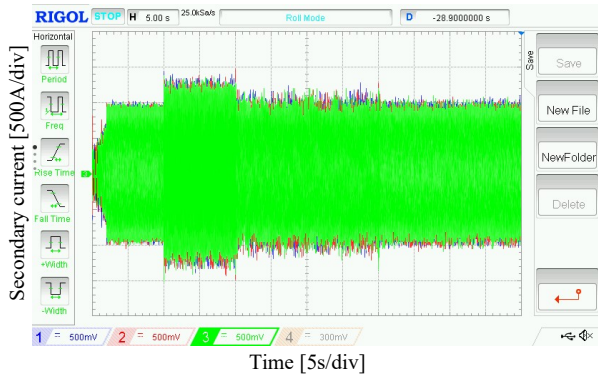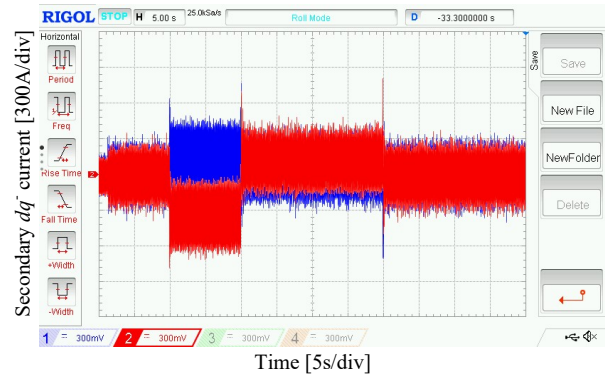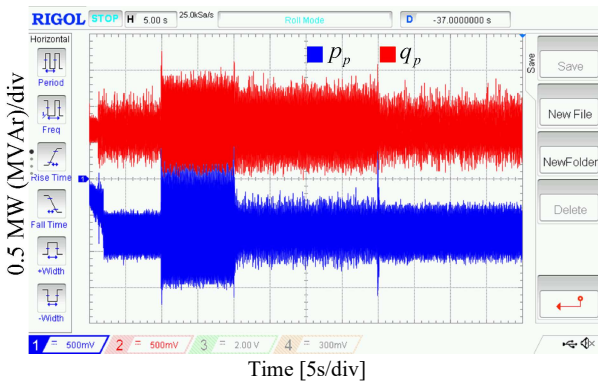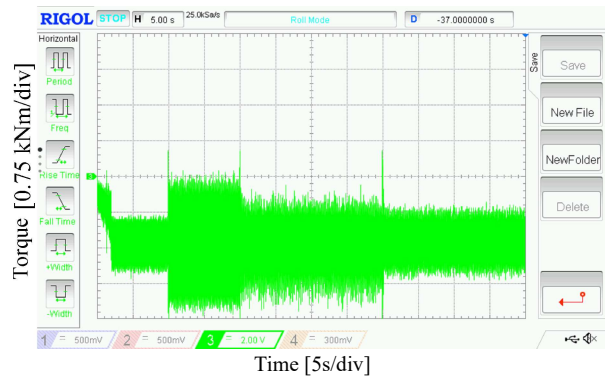
Figure 6.10. Real-time performance of the designed controller to eliminate primary active power oscillatory components: (a) Primary current; (b) Primary negative dq current components; (c) secondary current; (d) secondary negative dq current components; (e) Primary active and reactive power ; (f) Electromagnetic torque

From the previous results, one can conclude that using these different control design targets, it is not possible to achieve more than a single control objective simultaneously. This is in accordance with the results obtained from simulations in Chapter 4

Therefore, to achieve optimal performance under unbalanced grid voltage conditions, coordinated control of the aforementioned control objectives is improved. This control approach was described and verified through simulations in Chapter 4

The negative sequence components of primary and secondary currents, oscillatory components of torque and active and reactive power, can be reduced simultaneously as shown in Figure 6.11 using the reference values for negative sequence *dq* secondary currents, as described in (4.55) and (4.56).

(a)

(b)

(c)

(d)

(d)
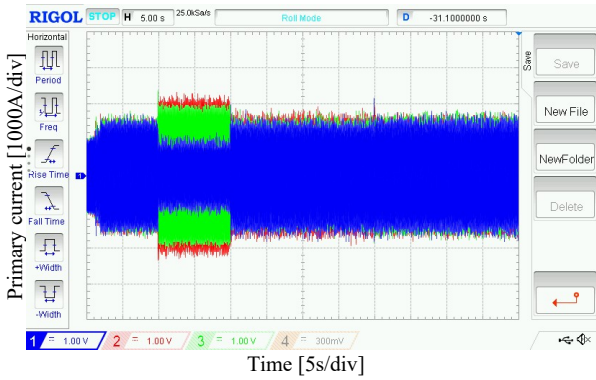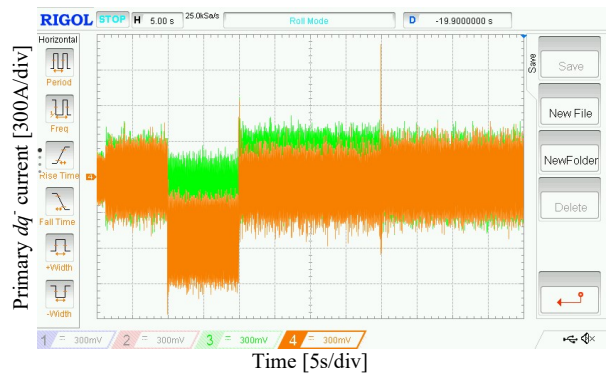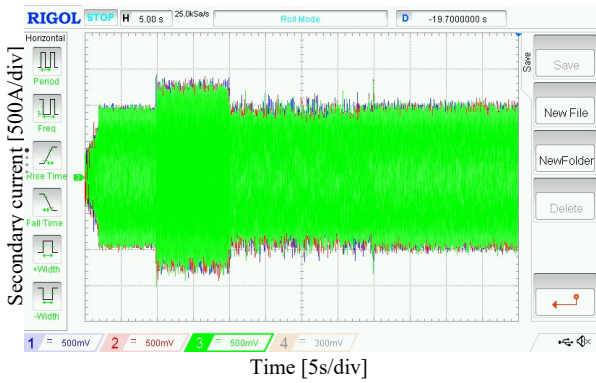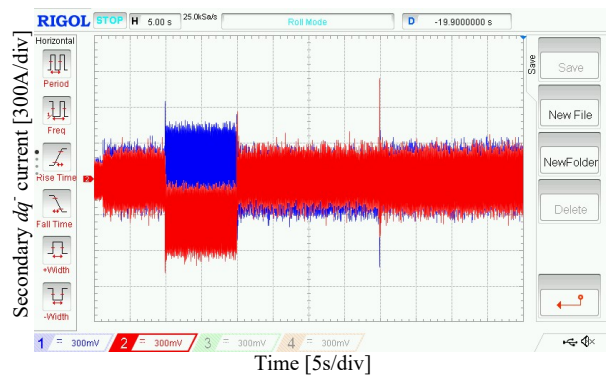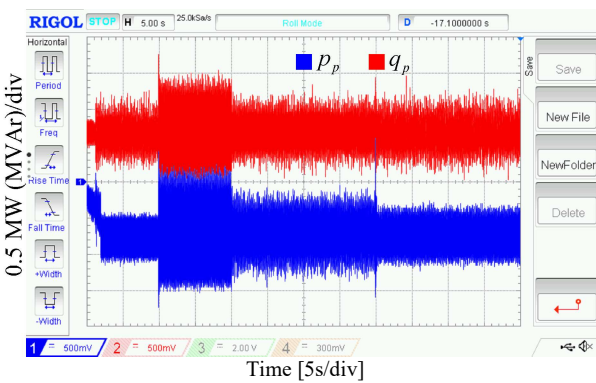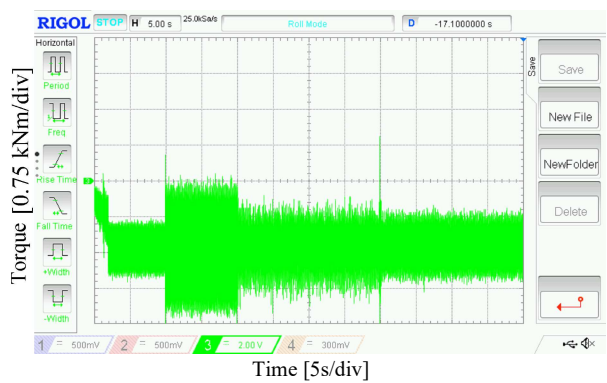
(f)

Figure 6.11. Real-time performance of designed auxiliary controller using the proposed optimal algorithm: (a) Primary current; (b) Primary negative dq current components; (c) secondary current; (d) secondary negative dq current components; (e) Primary active and reactive power ; (f) Electromagnetic torque

All reported research concerning the BDFRG has been limited to testing prototypes in the kW range. However, it is necessary to test the viability of any topology at the MW level to understand the stability and robustness of the system.

With no possibility to perform an experimental test on a large-scale BDFRG, the HIL testing is considered the best option to verify the performance of the BDFRG under UGVCs with the proposed vector control algorithm.

For the aforementioned control targets, Table 6.2 summarizes the following metrics: relative amplitude of the primary negative sequence current to the amplitude of the primary positive sequence current, amplitude of the secondary negative sequence current to the amplitude of the secondary positive sequence current, pulsations of the generator torque, and pulsations of the primary active and reactive power.

According to the results in the Table 6.2, one can conclude that the proposed controller ensures the best overall performance, even though it does not provide best results for any individual criterion.

Table 6.2. Comparisons of the different control targets with the proposed optimal design

Control method	Amplitude of $(\bar{i}_p)$ %	Amplitude of $(\bar{i}_s)$ %	Amplitude of torque oscillations %	Amplitude of active power oscillations %	Amplitude of reactive power oscillations %
Eliminate $(\bar{i}_p)$ Figure 6.7(a, b)	0.7	7	12.5	13.5	15.4
Eliminate $(\bar{i}_s)$ Figure6.8(c, d)	6.25	0.71	10.9	15	12.6
Eliminate $(T_1,T_2/ Q_1,Q_2)$ Figure6.9(e,f)	10.12	10	0.8	24	0.7
Eliminate (P_1,P_2) Figure6.10(e)	11	14	26	1.1	29
Proposed optimal controller Figure 6.11	4.5	5.3	8	12	9

Chapter 7

Conclusion

7.1 **Summary**

The share of wind energy with respect to total installed power capacity is increasing worldwide. The DFIG-based wind turbine with a partially scaled power converter is the most widespread wind power generator in wind power applications. However, due to its favorable operational characteristics, the BDFRG has been receiving increasing attention from the scientific community and it has been proposed as a potential alternative to the existing solutions for wind power applications since it retains most of the DFIG's merits while offering better reliability and lower maintenance cost.

Wind turbines are often installed in remote rural areas characterized by weak, unbalanced grid voltage. The presence of negative-sequence components in the grid voltage poses serious problems for wind generators, including unbalanced primary currents, current harmonics at the secondary side, and unequal heating or hot spots in the windings which degrade the insulation and reduce winding life expectancy. The interaction between negative-sequence voltage and positive-sequence current also causes power and torque pulsations, which inflict additional mechanical stress on the drive train and gearbox and increase acoustic noise, too. Hence, studying the performance of wind generators under UGVCs and designing a suitable control algorithm is very important.

A thorough understanding of the modeling, control, and dynamics as well as the steady-state analysis of the BDFRG is necessary to accurately predict its performance. A steady-state model of the BDFRG-based wind turbine system with variable speed was presented and used to analyze its mechanical and electrical operating characteristics in both super and sub-synchronous modes of operation. Derived from the steady-state model, the secondary voltage required for controlling the machine's operating mode was calculated and the machine's power flows are also analyzed under varying wind speeds.

The main aim of this dissertation was to develop control strategies and analyze the performance of a large-scale BDFRG-based WECS under UGVCs. To meet this objective, the first step was to improve a detailed dynamic model of a BDFRG-based WECS under unbalanced grid conditions using positive and negative sequence equations which are later used to design a proper control algorithm.

Regarding the WECS, various control techniques to extract maximum power from the wind turbine have been reported in the literature. In this thesis, three commonly used control algorithms, i.e. scalar control, vector control, and DTC were discussed in detail in Chapter 3.

The main aspects, mathematical model of a BDFRG under UGVCs and the advanced vector control strategy developed for UGVCs were presented in Chapter 5. An extended vector control algorithm is used to control both the positive and negative sequence components of the secondary currents independently. The model of the machine under UGVCs is used to derive the control form relationships between torque, real and reactive power, including positive and negative sequence components.

The simulation results show that by using the conventional vector control strategy, the positive sequence components are well-regulated by common PI controllers, while the negative sequence

component cannot be fully regulated due to the controller's limited bandwidth. Therefore, the extended vector control strategy has been used to overcome the negative sequence voltage effects resulting in the development of a new and original control algorithm, which presents one of the main contributions of this thesis. The secondary reference current was set to achieve one of the following control objectives: balancing primary currents, eliminating the torque and reactive power pulsating terms, eliminating the double-frequency pulsations of the primary active power, and eliminating the secondary currents pulsations.

The simulation results showed that by using the extended vector control strategy, it is not possible to achieve more than a single control objective simultaneously. Therefore, to achieve optimal performance under UGVCs, a new optimal control strategy was developed by considering all objectives simultaneously in order to comprise all the aforementioned objectives simultaneously. In the newly proposed optimal control algorithm, the controller's reference values are selected using a multi-objective optimization (MOO) method. A weighted-sum approach is used to convert multiple objectives into a parametric single-objective cost function. This is second new and original control algorithm developed within the proposed research work, presenting the other significant contribution of this thesis.

For examination purposes, a FEM model of the BDFRG using ANSYS Maxwell software is provided. In addition, the main BDFRM design aspects and difficulties are discussed. The main dimensions of a 1.5 MW BDFRG were estimated according to the parameters of a small-scale machine, and then the accuracy and effectiveness of the theoretical analysis were investigated using ANSYS Maxwell software.

The improved control has been evaluated and validated in two manners, using Maxwell/Simplorer/Simulink co-simulation (for a small-scale machine) and the Hardware-In-the-Loop (HIL) system (for a large-scale machine). The results show that the performance of the BDFRG-based WECS can be improved under UVGCs using the proposed vector control strategy for different control objectives. Moreover, the optimal controller can mitigate the pulsations for all the operational characteristics simultaneously, which improves the performance of the BDFRG based WECS.

The original contribution of this thesis is the development of vector control strategies for large-scale BDFRG under UGVCs. Besides, the thesis presents the original design of a large-scale BDFRG which was used to evaluate the performance of the improved control algorithm.

7.2 Plans for Future Work

The following topics are proposed for future work and the continuance of this work:

1. Experimental implementation of the proposed strategies in a laboratory environment for a small-scale BDFRG prototype;

2. Implementation of other techniques proposed in the literature and advanced control techniques such as, for example, neural network and fuzzy logic;

3. Comparison of control techniques, paying attention to accuracy and performance, as well as comparison between the implementation costs of each control technique.

4. Development of low voltage ride-through (LVRT) technology for a BDFRG to meet the grid codes standard, especially for wind power applications

5. Optimization a 1.5 MW BDFRG design with high performance for industrial applications.

Appendix A
Design calculations

Parameters (fixed):

$Pp := 8$ primary poles

$p := \dfrac{Pp}{2} = 4$ primary pole pairs

$Ps := 4$ secondary poles

$q := \dfrac{Ps}{2} = 2$ secondary pole pairs

$Pr := p + q = 6$ Rotor poles

$Nsl := 72$ number of slots

$Nrd := 66$ number of rotor ducts

$Np := 12$ number of turns of primary (one phase)

$Ns := 12$ number of turns of secondary (one phase)

$Np_s := \dfrac{Np}{\left(\dfrac{Nsl}{3 \cdot 2}\right)} = 1$ number of primary turns per slots

$Ns_s := \dfrac{Ns}{\left(\dfrac{Nsl}{3 \cdot 2}\right)} = 1$ number of secondary turns per slots

$np := \dfrac{Np}{p} = 3$ number of turns per pole (primary)

$ns := \dfrac{Ns}{q} = 6$ number of turns per pole (secondary)

$npp := \dfrac{Nsl}{3 \cdot Pp} = 3$ number of slots per phase per pole (primary)

$nsp := \dfrac{Nsl}{3 \cdot Ps} = 6$ number of slots per phase per pole (secondary)

Appendix A. Design calculations

Definitions for the model

$\theta rm0 := 0deg$ — Initial rotor position

$\gamma 1 := Pr \cdot \theta rm0 = 0 \cdot deg$ — Initial torque angle proportional to the initial rotor position

$\alpha c := \phi torque - \gamma 1 = 90 \cdot deg$ — Difference between the current phases of the
$\alpha c = 1.571 \cdot rad$ — primary and secondary windings

Dimensions

$Dso := 1.4m$ — stator outer diameter

$Dsl := 1.2m$ — slot outer diameter

$Dsi := 0.95m$ — stator inner diameter

$Lstack := 1m$ — machine axial lengtt
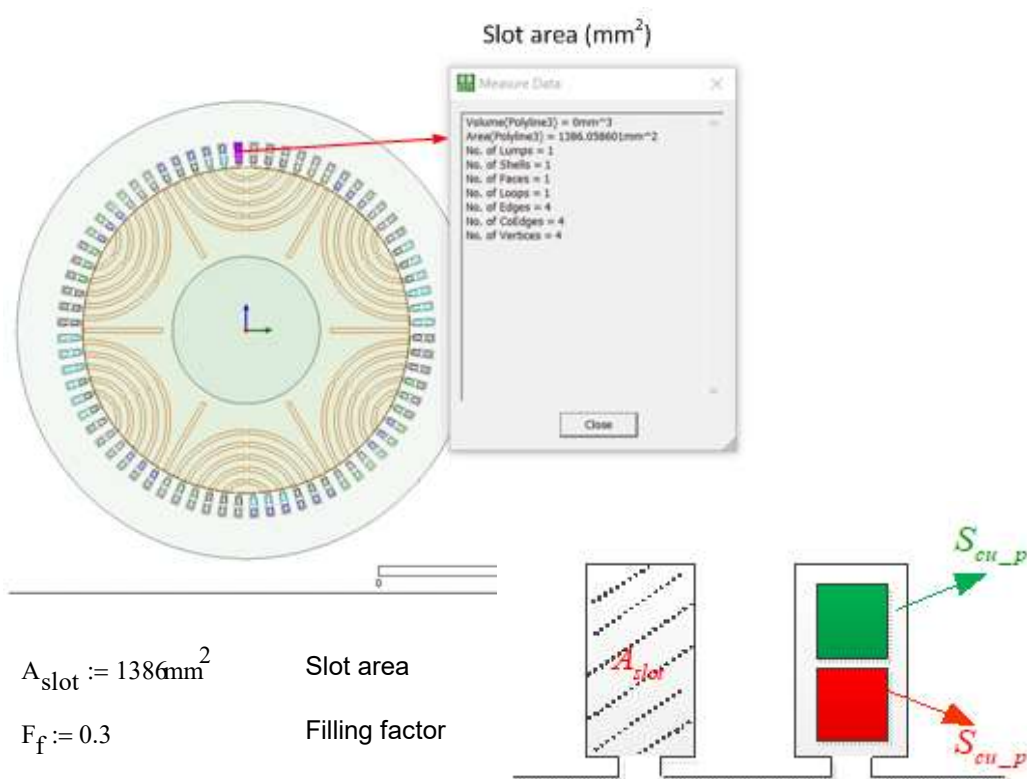
Slot area (mm²)

$A_{slot} := 1386mm^2$ — Slot area

$F_f := 0.3$ — Filling factor

$$S_{cu\_p} := \frac{\frac{A_{slot}}{2} \cdot F_f}{Np_s} = 2.079 \times 10^{-4} m^2$$ — conductor area (primary)

$$S_{cu\_s} := \frac{\frac{A_{slot}}{2} \cdot F_f}{Ns_s} = 2.079 \times 10^{-4} m^2$$ — conductor area (secondary)

Appendix A. Design calculations

Phase winding resistance

$\text{unit\_corr} := m \cdot \Omega$

$\text{Kwir} := 1.2$ correction factor

$\alpha t := 0.0038$ copper resistivity as a function of the temperature

$\text{tst} := 130$ considered temperature in stator windings

$\text{rho} := 1.7 \cdot 10^{-8}$ copper resisitivety

$\text{rhot} := \text{rho} \cdot [1 + \alpha t \cdot (\text{tst} - 20)] \cdot \text{unit\_corr} = 2.411 \times 10^{-8} \dfrac{kg \cdot m^3}{s^3 \cdot A^2}$
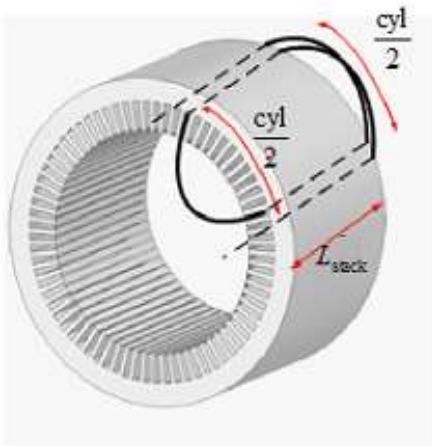
$\text{csl} := 2 \cdot \text{Lstack} = 2\,m$ coil side length

$\text{cylp} := 2 \cdot \left(\dfrac{\frac{\text{Dso} + \text{Dsl}}{2}}{2} \right) \cdot \left(2 \cdot \dfrac{\pi}{\text{Pp}} \right) = 1.021m$ coil yoke length(primary)

$\text{cyls} := 2 \cdot \left(\dfrac{\frac{\text{Dso} + \text{Dsl}}{2}}{2} \right) \cdot \left(2 \cdot \dfrac{\pi}{\text{Ps}} \right) = 2.042m$ coil yoke length(secondary

$\text{Ltp} := \text{csl} + \text{cylp} = 3.021m$ total winding length (primary)

$\text{Lts} := \text{csl} + \text{cyls} = 4.042m$ total winding length (secondary)

$\text{Rp} := \text{rhot} \cdot \dfrac{\left(\text{Kwir} \cdot \text{Ltp} \cdot \frac{\text{Pp}}{2} \cdot \text{npp} \cdot \text{Np}_s \right)}{\text{S}_{\text{cu\_p}}} = 5.044 \times 10^{-3} \cdot \Omega$ Primary resistance

$\text{Rs} := \text{rhot} \cdot \dfrac{\left(\text{Kwir} \cdot \text{Lts} \cdot \frac{\text{Ps}}{2} \cdot \text{nsp} \cdot \text{Ns}_s \right)}{\text{S}_{\text{cu\_s}}} = 6.749 \times 10^{-3} \cdot \Omega$ Secondary resistance

Appendix A. Design calculations

Leakage inductance in slot:

$b_{slot} := 19 \cdot 10^{-3} m$

$h_4 := 35 \cdot 10^{-3} m$

$b_1 := 8 \cdot 10^{-3} m$

$h_1 := 10 \cdot 10^{-3} m$
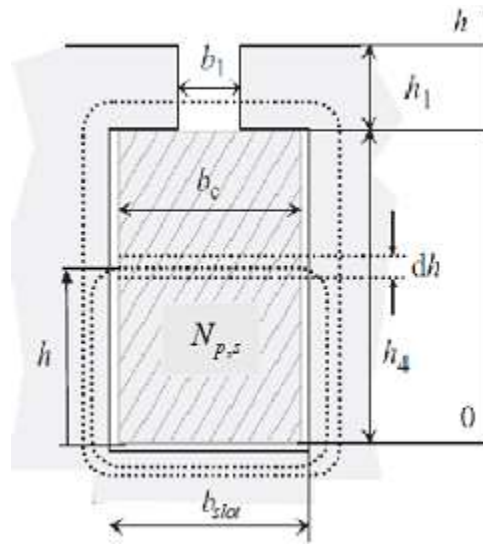
$L_{slotp} := \mu 0 \cdot N p_s^2 \cdot L stack \cdot \left(0.66 + \dfrac{h_1}{b_1} + \dfrac{h_4}{3 \cdot b_{slot}}\right) = 3.172 \times 10^{-6} H$ slot leakage inductance (primary)

$L_{slots} := \mu 0 \cdot N s_s^2 \cdot L stack \cdot \left(0.66 + \dfrac{h_1}{b_1} + \dfrac{h_4}{3 \cdot b_{slot}}\right) = 3.172 \times 10^{-6} H$ slot leakage inductance (secondary)

$L_{slotp\_total} := L_{slotp} \cdot \dfrac{Nsl}{3} = 7.612 \times 10^{-5} H$

$L_{slots\_total} := L_{slots} \cdot \dfrac{Nsl}{3} = 7.612 \times 10^{-5} H$

     Total slot leakage inductance

End winding Leakage inductance

$hew := 0.342$

           permeance factors

$hw := 0.243$

$Tip\_p := \pi \cdot \dfrac{Dsl}{Pp} = 0.471 m$ Coil span (primary)

$Tip\_s := \pi \cdot \dfrac{Dsl}{Ps} = 0.942 m$ Coil span (primary)

$Td := \pi \cdot \dfrac{Dsl}{Nsl} = 0.052 m$ one slot pitch

$w_p := Tip\_p - Td = 0.419 m$ width of the end winding (primary)

$w_s := Tip\_s - Td = 0.89 m$ width of the end winding (secondary)

$L_{w\_p} := 0.5 \cdot (cylp - w_p) = 0.301 m$ axial length of the end winding measured from the end of the stack (primary)

$L_{w\_s} := 0.5 \cdot (cyls - w_s) = 0.576 m$ axial length of the end winding measured from the end of the stack (secondary)
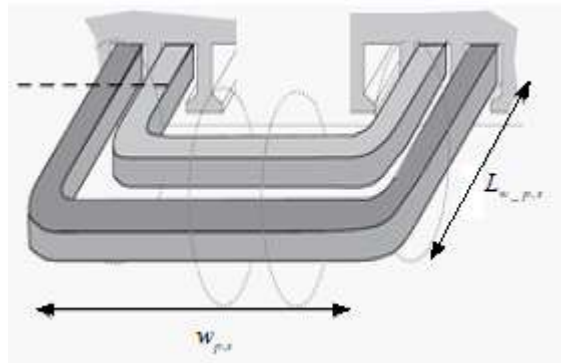
Appendix A. Design calculations

The use of the winding function theory to calculate inductances

$\text{Ip} := 1200\text{A}$ $\text{Is} := 1200\text{A}$ excitation currents used in each winding to inductance calculation

1. Spatial MMF distribution (single phase)

1.1- Primary windings

$$\text{Fpa}(\theta ag) := \frac{2}{\pi} \cdot \text{Np} \cdot \frac{\text{Kw}}{p} \cdot \text{Ip} \cdot \cos(p \cdot \theta ag)$$

$$\text{Fpb}(\theta ag) := \frac{2}{\pi} \cdot \text{Np} \cdot \frac{\text{Kw}}{p} \cdot \text{Ip} \cdot \cos\left(p \cdot \theta ag - 2 \cdot \frac{\pi}{3}\right)$$

$$\text{Fpc}(\theta ag) := \frac{2}{\pi} \cdot \text{Np} \cdot \frac{\text{Kw}}{p} \cdot \text{Ip} \cdot \cos\left(p \cdot \theta ag + 2 \cdot \frac{\pi}{3}\right)$$
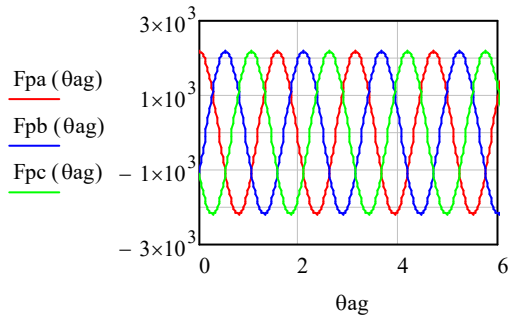
1.2- Secondary windings

$\alpha \text{temp} := 0\text{deg}$ angles which defines the position between grid and control a phase

$$\text{Fsa}(\theta ag) := \frac{2}{\pi} \cdot \text{Ns} \cdot \frac{\text{Kw}}{q} \cdot \text{Is} \cdot \cos(q \cdot \theta ag - q \cdot \alpha \text{temp})$$

$$\text{Fsb}(\theta ag) := \frac{2}{\pi} \cdot \text{Ns} \cdot \frac{\text{Kw}}{q} \cdot \text{Is} \cdot \cos\left(q \cdot \theta ag - q \cdot \alpha \text{temp} - 2 \cdot \frac{\pi}{3}\right)$$

$$\text{Fsc}(\theta ag) := \frac{2}{\pi} \cdot \text{Ns} \cdot \frac{\text{Kw}}{q} \cdot \text{Is} \cdot \cos\left(q \cdot \theta ag - q \cdot \alpha \text{temp} + 2 \cdot \frac{\pi}{3}\right)$$

98
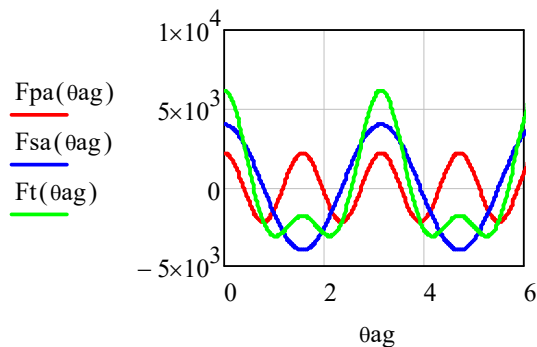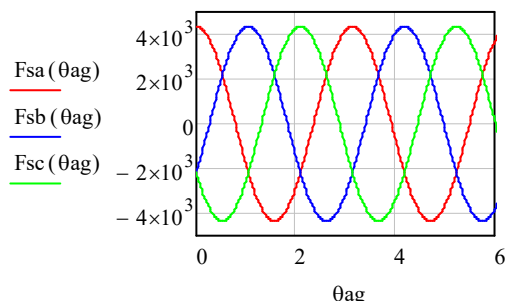
2- Calculation of airgap flux density in air gap considering an ideal airgap

$\text{rgap} := \dfrac{\text{Dsi}}{2} = 0.475\text{m}$ airggap radius

$\text{gap} := 2\text{mm}$ air gap length

$\text{slot}_{op} := 8\text{mm}$ slot openning

$\text{Tus} := \pi \cdot \dfrac{\text{Dsi}}{\text{Nsl}} = 0.041\text{m}$ stator tooth pitch including slot openning

$ks := \dfrac{2}{\pi} \cdot \left[\text{atan}\left(\dfrac{\text{slot}_{op}}{2 \cdot \text{gap}} \right) - 2 \cdot \dfrac{\text{gap}}{\text{slot}_{op}} \cdot \ln\left[\sqrt{1 + \left(\dfrac{\text{slot}_{op}}{2 \cdot \text{gap}} \right)^2} \right] \right] = 0.449$

$\text{Kcs} := \dfrac{\text{Tus}}{\text{Tus} - \text{slot}_{op} \cdot ks} = 1.095$ Carter's coefficient for the stator

$\text{Tur} := \pi \cdot \dfrac{\text{Dsi}}{\text{Nrd}} = 0.045\text{m}$ rotor tooth pitch including slot openning

$\text{SlrWidth} := 0.013\text{m}$ rotor slot width

$kr := \dfrac{2}{\pi} \cdot \left[\text{atan}\left(\dfrac{\text{SlrWidth}}{2 \cdot \text{gap}} \right) - 2 \cdot \dfrac{\text{gap}}{\text{SlrWidth}} \cdot \ln\left[\sqrt{1 + \left(\dfrac{\text{SlrWidth}}{2 \cdot \text{gap}} \right)^2} \right] \right] = 0.57$

$\text{Kcr} := \dfrac{\text{Tur}}{\text{Tur} - \text{SlrWidth} \cdot kr} = 1.196$ Carter's coefficient for the rotor

$\text{Kct} := \text{Kcs} \cdot \text{Kcr} = 1.309$ total Carter's coefecient

$\text{gap}_{ef} := \text{Kct} \cdot \text{gap} = 2.619 \times 10^{-3}\text{ m}$ efctive air-gap length

$\lambda r := \dfrac{2 \cdot \pi}{\text{Pr}} = 60 \cdot \text{deg}$ rotor pole arc angle

2.1- Primary windings

$\text{Bpa}(\theta\text{ag}) := \dfrac{\mu 0}{2 \cdot \text{gap}_{ef}} \cdot (\text{Fpa}(\theta\text{ag}) - \text{Fpa}(\theta\text{ag} + \lambda r - 2 \cdot \text{mod}(\text{mod}(\theta\text{ag} - \theta\text{ag}0, \lambda r) + \lambda r, \lambda r)))$

$\text{Bpb}(\theta\text{ag}) := \dfrac{\mu 0}{2 \cdot \text{gap}_{ef}} \cdot (\text{Fpb}(\theta\text{ag}) - \text{Fpb}(\theta\text{ag} + \lambda r - 2 \cdot \text{mod}(\text{mod}(\theta\text{ag} - \theta\text{ag}0, \lambda r) + \lambda r, \lambda r)))$

$\text{Bpc}(\theta\text{ag}) := \dfrac{\mu 0}{2 \cdot \text{gap}_{ef}} \cdot (\text{Fpc}(\theta\text{ag}) - \text{Fpc}(\theta\text{ag} + \lambda r - 2 \cdot \text{mod}(\text{mod}(\theta\text{ag} - \theta\text{ag}0, \lambda r) + \lambda r, \lambda r)))$
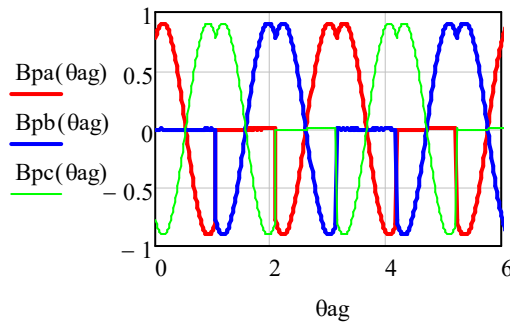
2.2- Secondary windings

$$Bsa(\theta ag) := \frac{\mu 0}{2 \cdot gap_{ef}} \cdot (Fsa(\theta ag) - Fsa(\theta ag + \lambda r - 2 \cdot mod(mod(\theta ag - \theta ag0, \lambda r) + \lambda r, \lambda r)))$$

$$Bsb(\theta ag) := \frac{\mu 0}{2 \cdot gap_{ef}} \cdot (Fsb(\theta ag) - Fsb(\theta ag + \lambda r - 2 \cdot mod(mod(\theta ag - \theta ag0, \lambda r) + \lambda r, \lambda r)))$$

$$Bsc(\theta ag) := \frac{\mu 0}{2 \cdot gap_{ef}} \cdot (Fsc(\theta ag) - Fsc(\theta ag + \lambda r - 2 \cdot mod(mod(\theta ag - \theta ag0, \lambda r) + \lambda r, \lambda r)))$$
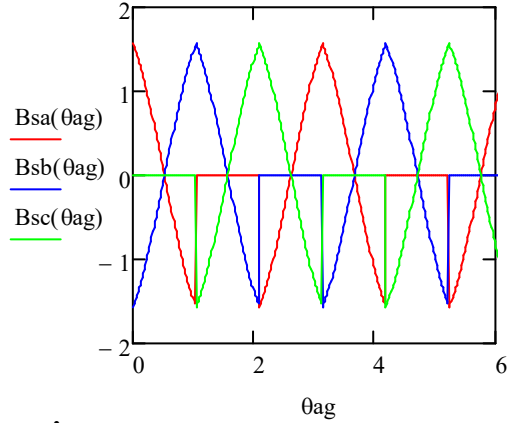
3-Winding function

3.1- Primary windings

$$Npa(\theta ag) := \frac{Fpa(\theta ag)}{Ip} \qquad Npb(\theta ag) := \frac{Fpb(\theta ag)}{Ip} \qquad Npc(\theta ag) := \frac{Fpc(\theta ag)}{Ip}$$
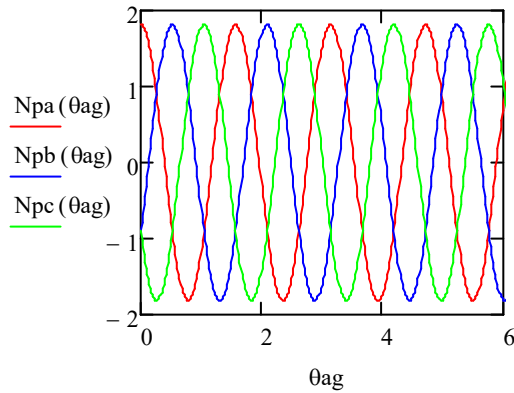
3.2- Secondary windings

$$Nsa(\theta ag) := \frac{Fsa(\theta ag)}{Is} \qquad Nsb(\theta ag) := \frac{Fsb(\theta ag)}{Is} \qquad Nsc(\theta ag) := \frac{Fsc(\theta ag)}{Is}$$

100
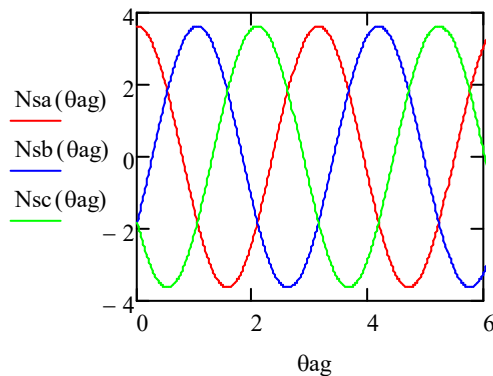
Appendix A. Design calculations

4-Self flux linkage

4.1- Primary windings

$$\lambda papa := rgap \cdot Lstack \cdot \int_0^{2\cdot\pi} Npa(\theta ag) \cdot Bpa(\theta ag) \, d\theta ag = 1.707 Wb$$

$$\lambda pbpb := rgap \cdot Lstack \cdot \int_0^{2\cdot\pi} Npb(\theta ag) \cdot Bpb(\theta ag) \, d\theta ag = 1.707 Wb \qquad \text{self fluxe linkage}$$

$$\lambda pcpc := rgap \cdot Lstack \cdot \int_0^{2\cdot\pi} Npc(\theta ag) \cdot Bpc(\theta ag) \, d\theta ag = 1.707 Wb$$

$$Lpapa := \frac{\lambda papa}{Ip} = 1.422 \times 10^{-3} H$$

$$Lpbpb := \frac{\lambda pbpb}{Ip} = 1.422 \times 10^{-3} H \qquad \text{self inductances}$$

$$Lpcpc := \frac{\lambda pcpc}{Ip} = 1.422 \times 10^{-3} H$$

4.2- Secondary windings

$$\lambda sasa := rgap \cdot Lstack \cdot \int_0^{2\cdot\pi} Nsa(\theta ag) \cdot Bsa(\theta ag) \, d\theta ag = 3.318 Wb$$

$$\lambda sbsb := rgap \cdot Lstack \cdot \int_0^{2\cdot\pi} Nsb(\theta ag) \cdot Bsb(\theta ag) \, d\theta ag = 3.318 Wb$$

$$\lambda scsc := rgap \cdot Lstack \cdot \int_0^{2\cdot\pi} Nsc(\theta ag) \cdot Bsc(\theta ag) \, d\theta ag = 3.318 Wb$$

$$Lsasa := \frac{\lambda sasa}{Is} = 2.765 \times 10^{-3} H$$

$$Lsbsb := \frac{\lambda sbsb}{Is} = 2.765 \times 10^{-3} H$$

$$Lscsc := \frac{\lambda scsc}{Is} = 2.765 \times 10^{-3} H$$

4.3- Mutual flux linkage between phases of DIFFERENT winding

$$\lambda pasa := rgap \cdot Lstack \cdot \int_0^{2\cdot\pi} Npa(\theta ag) \cdot Bsa(\theta ag) \, d\theta ag = 2.339 Wb$$

$$\lambda pasb := rgap \cdot Lstack \cdot \int_0^{2\cdot\pi} Npa(\theta ag) \cdot Bsb(\theta ag) \, d\theta ag = -1.17 Wb$$

$$\lambda pasc := rgap \cdot Lstack \cdot \int_0^{2\cdot\pi} Npa(\theta ag) \cdot Bsc(\theta ag) \, d\theta ag = -1.17 Wb$$

$$Lpasa := \frac{\lambda pasa}{Is} = 1.949 \times 10^{-3} H$$

$$Lpasb := \frac{\lambda pasb}{Is} = -9.746 \times 10^{-4} H$$

$$Lpasc := \frac{\lambda pasc}{Is} = -9.746 \times 10^{-4} H$$

5- Primary and secondary inductances

$$Lp := 1.5 \cdot Lpapa + L_{slotp\_total} + L_{ew\_p} = 2.237 \times 10^{-3} \, H$$

$$Ls := 1.5 \cdot Lsasa + L_{slots\_total} + L_{ew\_s} = 4.334 \times 10^{-3} \, H$$

$$Lps := 1.5 \cdot Lpasa = 2.924 \times 10^{-3} \, H$$

Normalaized flux density

$$Bp(\theta ag) := \left[\cos(4 \cdot \theta ag) - \cos\left[4 \cdot \left(\theta ag + \frac{\pi}{3} - 2 \cdot \text{mod}\left(\theta ag, \frac{\pi}{3} \right) \right) \right] \right]$$

$$Bs(\theta ag) := \left[\cos\left(2 \cdot \theta ag + \frac{\pi}{2} \right) - \cos\left[2 \cdot \left(\theta ag + \frac{\pi}{3} - 2 \cdot \text{mod}\left(\theta ag, \frac{\pi}{3} \right) \right) + \frac{\pi}{2} \right] \right]$$
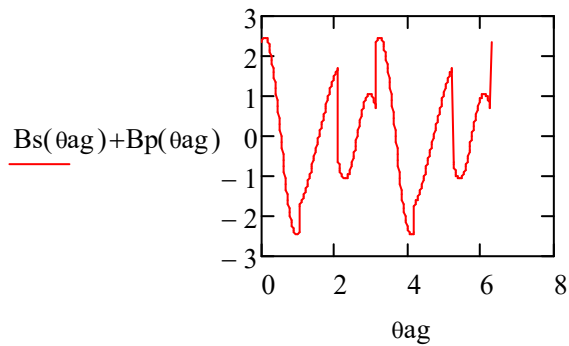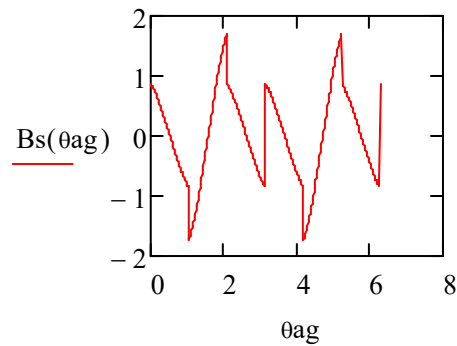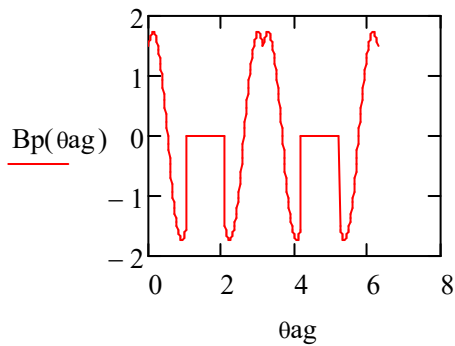
Appendix B
Steady state analysis

$P_n := 1.5 MW$ rated power

$V_{sn} := \dfrac{690}{\sqrt{3}} V$ rated voltage

$V_p := \dfrac{690}{\sqrt{3}} V$ primary voltage

$PF := \dfrac{1.5}{1.58}$ Power factor

$I_n := \dfrac{P_n}{3 V_{sn} \cdot PF}$ rated current

$f_{sn} := 50 \cdot Hz$ grid frequency

$\omega_{sn} := 2 \cdot \pi \cdot f_{sn}$ $\omega_{sn} = 314.159 \dfrac{rad}{s}$

$Pr := 6$ rotor poles

$V_s := 0V$

Frequency in general can be different than 50Hz.

$f_p := f_{sn}$ $\omega_p := 2 \cdot \pi \cdot f_p$ $\Omega_p := \dfrac{\omega_p}{Pr}$

$n_s := \Omega_p$

$n_s = 500 \, rpm$ synchronous speed

$R_p := 0.005103 ohm$ $L_p := 0.002237 H$ primary resistance and inducatance

$R_s := 0.006827 ohm$ $L_s := 0.0044334 H$ secondary resistance and inducatanc

$L_{ps} := 0.0029241 H$ $V_s = 0 V$

$n_r := 492.7 rpm$ rotor speed (motor mode)
$I := 30.92$ Gearbox ratio

$\sigma := \dfrac{\pi}{2} rad$ Torque angle

$\Omega_{rw} := \dfrac{n_r}{I}$ Turbine speed

$\Omega_{rw} = 1.669 \dfrac{rad}{s}$

$\Omega_r := n_r$ $\omega_p = 314.159 \dfrac{rad}{s}$

$\Omega_r = 51.595 \dfrac{rad}{s}$

$\omega_r := Pr \cdot \Omega_r$ electrical rotor speed

$s\_rel := \dfrac{n_s - n_r}{n_s}$ $n_{s\_new} := \dfrac{n_r}{1 - s\_rel}$

$s\_rel = 0.015$ $n_{s\_new} = 52.36 \dfrac{1}{s} \cdot rad$ $s_{new\_rel} := \dfrac{n_s - n_{s\_new}}{n_s}$

Equivalent circuit

$i := \sqrt{-1}$

$Z_p(\omega_p) := R_p + i\omega_p \cdot (L_p - L_{ps})$ primary impedance

$Z_s(\omega_p, s\_rel) := \dfrac{R_s}{s\_rel} + i\omega_p \cdot (L_s - L_{ps})$ secondary impedance

$Z_m(\omega_p) := \omega_p \cdot i L_{ps}$ mutual impedance

$Z_p(\omega_p) = \left(5.103 \times 10^{-3} - 0.216i\right) \Omega$

$Z_m(\omega_p) = 0.919i \,\Omega$

$Z_s(\omega_p, s\_rel) = (0.468 + 0.474i) \,\Omega$

$Z_{in1}(\omega_p, s\_rel) := Z_p(\omega_p) + \dfrac{Z_m(\omega_p) \cdot Z_s(\omega_p, s\_rel)}{Z_m(\omega_p) + Z_s(\omega_p, s\_rel)}$

$Z_{in1}(\omega_p, s\_rel) = (0.188 + 0.158i) \,\Omega$

By solving equivalent circuits with short ciruited secondary and short ciruited primary, currents Is1 and Is2 are got, as well as Ip1 and Ip2, respectivelly.

$I_{p1}(V_p, \omega_p, s\_rel) := \dfrac{V_p}{Z_{in1}(\omega_p, s\_rel)}$

$I_{s1}(V_p, \omega_p, s\_rel) := \overline{\left(\dfrac{V_p \cdot e^{-i \cdot \sigma}}{Z_{in1}(\omega_p, s\_rel)} \cdot \dfrac{Z_m(\omega_p)}{Z_m(\omega_p) + Z_s(\omega_p, s\_rel)} \right)}$

$I_{p1}(V_p, \omega_p, s\_rel) = \left(1.24 \times 10^3 - 1.045i \times 10^3\right) A$

$I_{s1}(V_p, \omega_p, s\_rel) = (-372.427 + 942.908i) \, A$

$Z_{in2}(\omega_p, s\_rel) := Z_s(\omega_p, s\_rel) + \dfrac{Z_m(\omega_p) \cdot Z_p(\omega_p)}{Z_m(\omega_p) + Z_p(\omega_p)}$

$Z_{in2}(\omega_p, s\_rel) = (0.476 + 0.192i) \,\Omega$

$I_{s2}(V_s, \omega_p, s\_rel) := \overline{\left(\dfrac{\dfrac{\overline{V_s}}{s\_rel}}{Z_{in2}(\omega_p, s\_rel)} \right)}$

$I_{p2}(V_s, \omega_p, s\_rel) := \dfrac{\dfrac{\overline{V_s}}{s\_rel} \cdot e^{i \cdot \sigma}}{Z_{in2}(\omega_p, s\_rel)} \cdot \dfrac{Z_m(\omega_p)}{Z_m(\omega_p) + Z_p(\omega_p)}$

$I_{s2}(V_s, \omega_p, s\_rel) = 0 \cdot A$

$I_{p2}(V_s, \omega_p, s\_rel) = 0 \cdot A$

$I_s(V_p, V_s, \omega_p, s\_rel) := \left(I_{s1}(V_p, \omega_p, s\_rel)\right) - I_{s2}(V_s, \omega_p, s\_rel)$

$I_s(V_p, V_s, \omega_p, s\_rel) = (-372.427 + 942.908i) \, A$

$I_p(V_p, V_s, \omega_p, s\_rel) := I_{p1}(V_p, \omega_p, s\_rel) - I_{p2}(V_s, \omega_p, s\_rel)$

$I_p(V_p, V_s, \omega_p, s\_rel) = \left(1.24 \times 10^3 - 1.045i \times 10^3\right) A$

$$M_{en} := \frac{P_n}{\Omega_r} \qquad M_{en} = 2.907 \times 10^4 \cdot N \cdot m$$

$n_s = 500 \cdot rpm$

$n_{rn} := n_r$

$n_{rn} = 492.7 \cdot rpm$

$s\_reln := s\_rel$

$s\_rel = 0.015$

$I_{pn} := I_p(V_p, V_s, \omega_p, s\_reln)$

$I_{pn} = (1.24 \times 10^3 - 1.045i \times 10^3) A \quad |I_{pn}| = 1.621 \times 10^3 A \qquad arg(I_{pn}) = -40.111 \cdot deg$

$I_{sn} := I_s(V_p, V_s, \omega_p, s\_reln)$

$I_{sn} = (-372.427 + 942.908i) A \qquad |I_{sn}| = 1.014 \times 10^3 A \qquad arg(I_{sn}) = 111.553 deg$

$S_{p\_power}(V_p, V_s, \omega_p, s\_rel) := 3V_p \cdot \overline{I_p(V_p, V_s, \omega_p, s\_rel)}$

$S_{p\_powern} := S_{p\_power}(V_p, V_s, \omega_p, s\_reln)$ primary apparent power

$S_{p\_powern} = (1.482 \times 10^6 + 1.248i \times 10^6) W$

$P_p(V_p, V_s, \omega_p, s\_rel) := Re(S_{p\_power}(V_p, V_s, \omega_p, s\_rel))$ primary active power

$P_{pn} := (P_p(V_p, V_s, \omega_p, s\_reln)) = 1.482 \times 10^6 W$

$Q_p(V_p, V_s, \omega_p, s\_rel) := Im(S_{p\_power}(V_p, V_s, \omega_p, s\_rel))$ primary reactive power

$Q_{pn} := Q_p(V_p, V_s, \omega_p, s\_reln) = 1.248 \times 10^6 W$

$\omega_p = 314.159 \frac{1}{s} \cdot rad$

$S_{s\_power}(V_p, V_s, \omega_p, s\_rel) := 3V_s \cdot \overline{I_s(V_p, V_s, \omega_p, s\_rel)}$ secondary apparent power

$S_{s\_powern} := S_{s\_power}(V_p, V_s, \omega_p, s\_reln)$

$S_{s\_powern} = 0 W$

$P_s(V_p, V_s, \omega_p, s\_rel) := Re(S_{s\_power}(V_p, V_s, \omega_p, s\_reln))$ secondary active power

$P_{sn} := P_s(V_p, V_s, \omega_p, s\_reln) = 0 \cdot W$

$Q_s(V_p, V_s, \omega_p, s\_reln) := Im(S_{s\_power}(V_p, V_s, \omega_p, s\_reln))$ secondary reactive power

$Q_{sn} := Q_s(V_p, V_s, \omega_p, s\_reln) = 0 W$

$P_{Cup}(V_p, V_s, \omega_p, s\_rel) := 3 \cdot R_p \cdot (|I_p(V_p, V_s, \omega_p, s\_rel)|)^2$ primary cupper losses

$P_{Cupn} := P_{Cup}(V_p, V_s, \omega_p, s\_reln) \qquad P_{Cupn} = 4.025 \times 10^4 W$

$P_{Cus}(V_p, V_s, \omega_p, s\_rel) := 3 \cdot R_s \cdot (|I_s(V_p, V_s, \omega_p, s\_rel)|)^2$ secondary cupper losses

$P_{Cusn} := P_{Cus}(V_p, V_s, \omega_p, s\_reln) \qquad P_{Cusn} = 2.105 \times 10^4 W$

The power balace means that Pp+Ps=Pcup+Pcus+Pm

$$P_p\left(V_p, V_s, \omega_p, s\_reln\right) + P_s\left(V_p, V_s, \omega_p, s\_rel\right) = 1.482\times 10^6\,W$$

$$P_m\left(V_p, V_s, \omega_p, s\_reln\right) := \left(P_p\left(V_p, V_s, \omega_p, s\_reln\right) + P_s\left(V_p, V_s, \omega_p, s\_reln\right)\right) - P_{Cupn} - P_{Cusn}$$

$$P_{mn} := P_m\left(V_p, V_s, \omega_p, s\_reln\right) = 1.421\times 10^6\,W \qquad \text{mechanical power}$$

$$\left|I_{pn}\right| = 1.621\times 10^3\,A \qquad\qquad \arg\left(I_{pn}\right) = -40.111\cdot deg$$

$$\cos\left(\arg\left(I_{pn}\right)\right) = 0.765$$

$$\cos\varphi_n := \cos\left(\arg\left(I_{pn}\right)\right)$$

$$\eta_n := \frac{P_{mn}}{P_p\left(V_p, V_s, \omega_p, s\_reln\right) + P_s\left(V_p, V_s, \omega_p, s\_reln\right)} \qquad \text{efficiency}$$

$$\eta_n = 0.95864$$

This is the end of calculation fot motor mode of BDFRM operation. Now, the same calculation should be completed for the generator mode of operation for the same M.n, cos ? and ?.

Now machine generates the rated power (-P.n) for wind speed v= m/s. with cos?=- (generator mode). The machine working as generator will produce Ps=-P.n and by solving BDFRG equivalent circuit, the corresponding rotor speed could be calculated as follows:

$$\varphi_g := acos\left(-0.765\right)$$

$$\varphi_g = 139.907\,deg \qquad\qquad \theta_u := 0\,deg$$

$$\theta_i := \theta_u - \varphi_g = -139.907\,deg$$

$$P_{pg} := -P_{mn} \qquad\qquad P_{pg} = -1.421\times 10^6\,W$$

$$I_{pg} := \frac{P_{pg}}{3\cdot V_p\cdot \cos\left(\varphi_g\right)} \qquad\qquad I_{pg} = 1.554\times 10^3\,A$$

$$i_{pg} := I_{pg}\cdot\left(\cos\left(\theta_i\right) + i\cdot\sin\left(\theta_i\right)\right) \qquad\qquad i_{pg} = \left(-1.189\times 10^3 - 1.001i\times 10^3\right)A$$

From the expression for Ip=Ip1-Ip2, for short circuited rotor, Us=0, Ip2=0: Zs will be calculated from the expression from Ip2.

$$V_{pn} := V_p \qquad\qquad \omega_{pn} := \omega_p$$

$$Z_s := \frac{V_{pn}\cdot Z_m\left(\omega_{pn}\right) - i_{pg}\cdot Z_p\left(\omega_{pn}\right)\cdot Z_m\left(\omega_{sn}\right)}{i_{pg}\cdot\left(Z_p\left(\omega_{pn}\right) + Z_m\left(\omega_{pn}\right)\right) - V_p} \qquad Z_s = \left(-0.515 + 0.458i\right)\Omega$$

$$s\_relg := \frac{R_s}{Re\left(Z_s\right)}$$

$$s\_relg = -0.013$$

$$n_{rg} := \left(1 - s\_relg\right)\cdot n_s$$

$$n_{rg} = 506.626\,rpm$$

$$V_{pn} = 398.372\,V$$

$$I_{sn} := I_s\left(V_p, V_s, \omega_p, s\_relg\right)$$

$$I_{sn} = (-347.489 - 896.249i)\,A \qquad \left|I_{sn}\right| = 961.254A \qquad \arg\left(I_{sn}\right) = -111.192deg$$

$$I_{pn} := I_p\left(V_p, V_s, \omega_p, s\_relg\right)$$

$$I_{pn} = \left(-1.164\times 10^3 - 1.03i\times 10^3\right)A \qquad \left|I_{pn}\right| = 1.554\times 10^3\,A \qquad \arg\left(I_{pn}\right) = -138.509deg$$

$$S_{p\_power}\left(V_p, V_s, \omega_p, s\_relg\right) := 3V_p \cdot \overline{I_p\left(V_p, V_s, \omega_p, s\_relg\right)}$$

$$S_{p\_powern} := S_{p\_power}\left(V_p, V_s, \omega_p, s\_relg\right)$$

$$S_{p\_powern} = \left(-1.391\times 10^6 + 1.23i\times 10^6\right)W$$

$$P_p\left(V_p, V_s, \omega_p, s\_relg\right) := Re\left(S_{p\_power}\left(V_p, V_s, \omega_p, s\_relg\right)\right)$$

$$P_{pn} := \left(P_p\left(V_p, V_s, \omega_p, s\_relg\right)\right) = -1.391\times 10^6\,W$$

$$Q_p\left(V_p, V_s, \omega_p, s\_relg\right) := Im\left(S_{p\_power}\left(V_p, V_s, \omega_p, s\_relg\right)\right)$$

$$Q_{pn} := Q_p\left(V_p, V_s, \omega_p, s\_relg\right) = 1.23\times 10^6\,W$$

$$S_{s\_power}\left(V_p, V_s, \omega_p, s\_relg\right) := 3V_s \cdot \overline{I_s\left(V_p, V_s, \omega_p, s\_relg\right)}$$

$$S_{s\_powern} := S_{s\_power}\left(V_p, V_s, \omega_p, s\_relg\right) \qquad S_{s\_powern} = 0\,W$$

$$P_s\left(V_p, V_s, \omega_p, s\_relg\right) := Re\left(S_{s\_power}\left(V_p, V_s, \omega_p, s\_relg\right)\right)$$

$$P_{sn} := P_s\left(V_p, V_s, \omega_p, s\_relg\right) = 0\cdot W$$

$$Q_s\left(V_p, V_s, \omega_p, s\_relg\right) := Im\left(S_{s\_power}\left(V_p, V_s, \omega_p, s\_relg\right)\right)$$

$$Q_{sn} := Q_s\left(V_p, V_s, \omega_p, s\_relg\right) = 0\,W$$

$$P_{Cup}\left(V_p, V_s, \omega_p, s\_relg\right) := 3\cdot R_p\cdot\left(\left|I_p\left(V_p, V_s, \omega_p, s\_relg\right)\right|\right)^2$$

$$P_{Cupn} := P_{Cup}\left(V_p, V_s, \omega_p, s\_relg\right)$$

$$P_{Cupn} = 3.697\times 10^4\,W$$

$$P_{Cus}\left(V_p, V_s, \omega_p, s\_relg\right) := 3\cdot R_s\cdot\left(\left|I_s\left(V_p, V_s, \omega_p, s\_relg\right)\right|\right)^2$$

$$P_{Cusn} := P_{Cus}\left(V_p, V_s, \omega_p, s\_relg\right) \qquad P_{Cusn} = 1.892\times 10^4\,W$$

The power balace means that Pp+Ps=Pcup+Pcus+Pm

$$P_p\left(V_p, V_s, \omega_p, s\_relg\right) + P_s\left(V_p, V_s, \omega_p, s\_relg\right) = -1.391\times 10^6\,W$$

$$P_m\left(V_p, V_s, \omega_p, s\_relg\right) := \left(P_p\left(V_p, V_s, \omega_p, s\_relg\right) + P_s\left(V_p, V_s, \omega_p, s\_relg\right)\right) - P_{Cupn} - P_{Cusn}$$

$$P_{mn} := P_m\left(V_p, V_s, \omega_p, s\_relg\right) = -1.447\times 10^6\,W$$

$$\left|I_{pn}\right| = 1.554\times 10^3\,A \qquad \arg\left(I_{pn}\right) = -138.509deg \qquad \cos\left(\arg\left(I_{pn}\right)\right) = -0.749$$

$$\cos\varphi_{ng} := \cos\left(\arg\left(I_{pn}\right)\right)$$

$$\eta_{ng} := \frac{P_p\left(V_p, V_s, \omega_p, s\_relg\right)}{P_{mn} + P_s\left(V_p, V_s, \omega_p, s\_relg\right)}$$

$\eta_{ng} = 0.96137$

$s\_relg = -0.01325$

This is the end of calculation for the generator mode of operation of BDFRM for the short circuated secondary

The third case is when the speed of wind is lowered, giving the speed of turbine ?.t, with gear ratio I=30.92, that will provide the use a six pole machine with rated load slip *s*=-1.325% :

Turbine parameters

$\rho := 1.225 \dfrac{kg}{m^3}$ air density

$I := 30.92$ gearbox ratio

$R := 42m$ turbine radius

$C_p := 0.4$ power coefficient
$TSR := 7$ tip speed ratio

$v := 9.8 \cdot \dfrac{m}{s}$ wind speed

$P_w := 0.5 \cdot \rho \cdot \pi \cdot R^2 \cdot v^3 \cdot C_p$ wind power

$P_w = 1.278 \times 10^6 \, W$

$\omega_t := TSR \cdot \dfrac{v}{R}$ $\omega_t = 1.633 \dfrac{1}{s} \cdot rad$ turbine speed

$\omega_{rg} := \omega_t \cdot I$ $\omega_{rg} = 50.503 \dfrac{rad}{s}$ generator speed

$n_{rg} := \omega_{rg} = 482.26494 rpm$

The synchronous speed can be virtually lowered below, that can be achieved by supplied a proper secondary voltages. With the same slip (s_relg), the new synchronous speed has to be: $s\_relg = -0.013$

$n_{snew} := \dfrac{n_{rg}}{1 - s\_relg}$ $n_{snew} = 475.958 rpm$

$s\_new := \dfrac{n_s - n_{snew}}{n_s}$ $s\_new = 0.048$

The new value of s_new is used to calculate the needed value of secondary voltage to cancel secondary currents (to simulate synchronous speed):

$$V_{snew} := \left[\frac{s\_new \cdot Z_m\left(\omega_p\right)}{\left(Z_p\left(\omega_p\right) + Z_m\left(\omega_p\right)\right)} \cdot V_p \cdot e^{-i \cdot \sigma}\right]$$

$V_{snew} = (0.182 + 25.037i) \, V$

$\left|V_{snew}\right| = 25.038 V$

$arg\left(V_{snew}\right) = 89.584 deg$

The following calculation should be completed for the s_relg:

$n_{rg} = 482.265 rpm$ $V_{pn} = 398.372 V$ $V_{snew} = (0.182 + 25.037i) \, V$

$s\_rel\_new := \dfrac{n_s - n_{rg}}{n_s}$

$s\_rel\_new = 0.035$

$s\_relg := s\_rel\_new$

$Z_s\left(\omega_p, s\_relg\right) := \dfrac{R_s}{s\_relg} + \omega_p \cdot \left(L_s - L_{ps}\right) \cdot i$

$Z_{in1}\left(\omega_p, s\_relg\right) := Z_p\left(\omega_p\right) + \dfrac{Z_m\left(\omega_p\right) \cdot Z_s\left(\omega_p, s\_relg\right)}{Z_m\left(\omega_p\right) + Z_s\left(\omega_p, s\_relg\right)}$

$Z_{in2}\left(\omega_p, s\_relg\right) := Z_s\left(\omega_p, s\_relg\right) + \dfrac{Z_m\left(\omega_p\right) \cdot Z_p\left(\omega_p\right)}{Z_m\left(\omega_p\right) + Z_p\left(\omega_p\right)}$

$Z_{in1}\left(\omega_p, s\_relg\right) = (0.087 + 0.108i)\,\Omega$

$Z_{in2}\left(\omega_p, s\_relg\right) = (0.201 + 0.192i)\,\Omega$

$I_{p1}\left(V_p, \omega_p, s\_relg\right) := \dfrac{V_p}{Z_{in1}\left(\omega_p, s\_relg\right)}$

$I_{p1}\left(V_p, \omega_p, s\_relg\right) = \left(1.798 \times 10^3 - 2.231i \times 10^3\right) A$

$I_{s1}\left(V_p, \omega_p, s\_relg\right) := \overline{\left(\dfrac{V_p \cdot e^{-i \cdot \sigma}}{Z_{in1}\left(\omega_p, s\_relg\right)} \cdot \dfrac{Z_m\left(\omega_p\right)}{Z_m\left(\omega_p\right) + Z_s\left(\omega_p, s\_relg\right)}\right)}$

$I_{s1}\left(V_p, \omega_p, s\_relg\right) = \left(-1.283 \times 10^3 + 1.363i \times 10^3\right) A$

$I_{p2}\left(V_{snew}, \omega_p, s\_relg\right) := \dfrac{\dfrac{\overline{V_{snew}}}{s\_relg} \cdot e^{i \cdot \sigma}}{Z_{in2}\left(\omega_p, s\_relg\right)} \cdot \dfrac{Z_m\left(\omega_p\right)}{Z_m\left(\omega_p\right) + Z_p\left(\omega_p\right)}$

$I_{p2}\left(V_{snew}, \omega_p, s\_relg\right) = \left(2.431 \times 10^3 - 2.255i \times 10^3\right) A$

$I_{s2}\left(V_{snew}, \omega_p, s\_relg\right) := \overline{\left(\dfrac{\dfrac{V_{snew}}{s\_relg}}{Z_{in2}\left(\omega_p, s\_relg\right)}\right)}$

$I_{s2}\left(V_{snew}, \omega_p, s\_rel\right) = \left(-1.227 \times 10^3 + 3.105i \times 10^3\right) \cdot A$

$I_p\left(V_p, V_{snew}, \omega_p, s\_relg\right) := \left(I_{p1}\left(V_p, \omega_p, s\_relg\right)\right) - I_{p2}\left(V_{snew}, \omega_p, s\_relg\right)$

$I_p\left(V_p, V_{snew}, \omega_p, s\_relg\right) = (-633.72 + 24.866i)\,A$

$\left|I_p\left(V_p, V_{snew}, \omega_p, s\_relg\right)\right| = 634.20773 A$

$I_s\left(V_p, V_{snew}, \omega_p, s\_relg\right) := I_{s1}\left(V_p, \omega_p, s\_relg\right) - I_{s2}\left(V_{snew}, \omega_p, s\_relg\right)$

$I_s\left(V_p, V_{snew}, \omega_p, s\_relg\right) = (456.216 - 484.688i)\,A$

$\left|I_s\left(V_p, V_{snew}, \omega_p, s\_relg\right)\right| = 665.62409 A$

$S_{p\_power}\left(V_p, V_{snew}, \omega_p, s\_relg\right) := 3 V_p \cdot \overline{I_p\left(V_p, V_{snew}, \omega_p, s\_relg\right)}$

$S_{p\_powerg} := S_{p\_power}\left(V_p, V_{snew}, \omega_p, s\_relg\right)$

$S_{p\_powerg} = \left(-7.574 \times 10^5 - 2.972i \times 10^4\right) W$

$P_p\left(V_p, V_{snew}, \omega_p, s\_relg\right) = -7.574 \times 10^5 \, W$

$Q_p\left(V_p, V_{snew}, \omega_p, s\_relg\right) = -2.972 \times 10^4 \, W$

$$S_{s\_power}(V_p, V_{snew}, \omega_p, s\_relg) := 3V_{snew} \cdot \overline{I_s(V_p, V_{snew}, \omega_p, s\_relg)}$$

$$S_{s\_powerg} := S_{s\_power}(V_p, V_{snew}, \omega_p, s\_relg)$$

$$S_{s\_powerg} = \left(-3.616 \times 10^4 + 3.453i \times 10^4\right) W$$

$$P_s(V_p, V_{snew}, \omega_p, s\_relg) = -3.616 \times 10^4 \, W$$

$$Q_s(V_p, V_{snew}, \omega_p, s\_relg) = 3.453 \times 10^4 \, W$$

$$P_{Cup}(V_p, V_{snew}, \omega_p, s\_relg) := 3 \cdot R_p \cdot \left(\left|I_p(V_p, V_{snew}, \omega_p, s\_relg)\right|\right)^2$$

$$P_{Cup} := P_{Cup}(V_p, V_{snew}, \omega_p, s\_relg)$$

$$P_{Cup} = 6.158 \times 10^3 \, W$$

$$P_{Cus}(V_p, V_{snew}, \omega_p, s\_relg) := 3 \cdot R_s \cdot \left(\left|I_s(V_p, V_{snew}, \omega_p, s\_relg)\right|\right)^2$$

$$P_{Cus} := P_{Cus}(V_p, V_{snew}, \omega_p, s\_relg)$$

$$P_{Cus} = 9.074 \times 10^3 \, W$$

$$P_{Cu\_total} := P_{Cup} + P_{Cus}$$

$$P_{Cu\ total} = 1.523 \times 10^4 \, W$$

Bibliography

[1]   T. Ackermann, *Wind power in power systems* vol. 200: Wiley New York, 2005.

[2]   T. Burton, N. Jenkins, D. Sharpe, and E. Bossanyi, *Wind energy handbook*: John Wiley & Sons, 2011.

[3]   J. F. Manwell, J. G. McGowan, and A. L. Rogers, *Wind energy explained: theory, design and application*: John Wiley & Sons, 2010.

[4]   Y. Zhou, P. Bauer, J. A. Ferreira, and J. Pierik, "Operation of Grid-Connected DFIG Under Unbalanced Grid Voltage Condition," *IEEE Transactions on Energy Conversion,* vol. 24, pp. 240-246, 2009, doi:10.1109/TEC.2008.2011833

[5]   H. Li and Z. Chen, "Overview of different wind generator systems and their comparisons," *IET Renewable Power Generation,* vol. 2, pp. 123-138, 2008,

[6]   O. Anaya-Lara, N. Jenkins, J. B. Ekanayake, P. Cartwright, and M. Hughes, *Wind energy generation: modelling and control*: John Wiley & Sons, 2011.

[7]   O. Anaya-Lara, J. O. Tande, K. Uhlen, and K. Merz, *Offshore Wind Energy Technology*: John Wiley & Sons, 2018.

[8]   J. S. Thongam and M. Ouhrouche, "MPPT control methods in wind energy conversion systems," *Fundamental and advanced topics in wind power,* vol. 15, pp. 339-360, 2011, doi:10.5772/21657

[9]   Z. Chen, J. M. Guerrero, and F. Blaabjerg, "A review of the state of the art of power electronics for wind turbines," *IEEE Transactions on power electronics,* vol. 24, pp. 1859-1875, 2009, doi:10.1109/TPEL.2009.2017082

[10]   R. Pena, J. Clare, and G. Asher, "Doubly fed induction generator using back-to-back PWM converters and its application to variable-speed wind-energy generation," *IEE Proceedings-Electric power applications,* vol. 143, pp. 231-241, 1996, doi:10.1049/ip-epa:19960454

[11]   P. C. Roberts, "A study of brushless doubly-fed (induction) machines," *PhD, University of Cambridge, Cambridge, UK,* 2004,

[12]   H. Gorginpour, H. Oraee, and R. A. McMahon, "Performance description of brushless doubly-fed induction machine in its asynchronous and variable speed synchronous modes," *Journal of Electromagnetic Analysis and Applications,* vol. 3, pp. 490-511, 2011, doi:10.4236/jemaa.2011.312077

[13]   T. Staudt, "Brushless doubly-fed reluctance machine modeling, design and optimization," Université Grenoble Alpes (ComUE), 2015.

[14]   B. Guan, "Design and control of a high-efficiency doubly-fed brushless machine for power generation applications," Doctor of Philosophy DISSERTATION, The Ohio State University, 2014.

[15]   L. Xu, B. Guan, H. Liu, L. Gao, and K. Tsai, "Design and control of a high-efficiency Doubly-Fed Brushless machine for wind power generator application," in *2010 IEEE Energy Conversion Congress and Exposition*, 2010, pp. 2409-2416, doi:10.1109/ECCE.2010.5617911

111

[16] L. J. Hunt, "The "cascade" induction motor," *Journal of the Institution of Electrical Engineers,* vol. 52, pp. 406-426, 1914, doi:10.1049/jiee-1.1914.0031

[17] F. Creedy, "Some developments in multi-speed cascade induction motors," *Journal of the Institution of Electrical Engineers,* vol. 59, pp. 511-532, 1921, doi:10.1049/jiee-1.1921.0036

[18] A. Broadway and L. Burbridge, "Self-cascaded machine: a low-speed motor or high-frequency brushless alternator," in *Proceedings of the Institution of Electrical Engineers*, 1970: IET, pp. 1277-1290, doi:10.1049/piee.1970.0247

[19] A. Broadway, "Cageless induction machine," in *Proceedings of the Institution of Electrical Engineers*, 1971: IET, pp. 1593-1600, doi:10.1049/piee.1971.0290

[20] A. Broadway, B. Cook, and P. Neal, "Brushless cascade alternator," in *Proceedings of the Institution of Electrical Engineers*, 1974: IET, pp. 1529-1535, doi:10.1049/piee.1974.0317

[21] A. Kusko and C. B. Somuah, "Speed control of a single-frame cascade induction motor with slip-power pump back," *IEEE transactions on industry applications,* pp. 97-105, 1978, doi:10.1109/TIA.1978.4503502

[22] L. Xu, F. Liang, and T. A. Lipo, "Transient model of a doubly excited reluctance motor," *IEEE Transactions on Energy Conversion,* vol. 6, pp. 126-133, 1991, doi:10.1109/60.73799

[23] F. Liang, L. Xu, and T. A. Lipo, "d-q ANALYSIS OF A VARIABLE SPEED DOUBLY AC EXCITED RELUCTANCE MOTOR," *Electric Machines & Power Systems,* vol. 19, pp. 125-138, 1991/03/01 1991, doi:10.1080/07313569108909511

[24] Y. Liao, L. Xu, and L. Zhen, "Design of a doubly fed reluctance motor for adjustable-speed drives," *IEEE Transactions on Industry Applications,* vol. 32, pp. 1195-1203, 1996, doi:10.1109/28.536883

[25] R. E. Betz and M. Jovanovic, "Introduction to Brushless Doubly Fed Reluctance Machines – The Basic Equations," 1998, doi:10.13140/RG.2.1.2646.4483

[26] R. E. Betz and M. Jovanovic, "Introduction to the Space Vector Modeling of the Brushless Doubly Fed Reluctance Machine," *Electric Power Components and Systems - ELECTR POWER COMPON SYST,* vol. 31, pp. 729-755, 08/01 2003, doi:10.1080/15325000390219785

[27] R. E. Betz and M. G. Jovanovic, "The brushless doubly fed reluctance machine and the synchronous reluctance machine-a comparison," *IEEE Transactions on Industry Applications,* vol. 36, pp. 1103-1110, 2000, doi:10.1109/28.855966

[28] M. G. Jovanovic, R. E. Betz, and Y. Jian, "The use of doubly fed reluctance machines for large pumps and wind turbines," *IEEE Transactions on Industry Applications,* vol. 38, pp. 1508-1516, 2002, doi:10.1109/TIA.2002.804749

[29] R. E. Betz and M. G. Jovanovic, "Theoretical analysis of control properties for the brushless doubly fed reluctance machine," *IEEE Transactions on Energy Conversion,* vol. 17, pp. 332-339, 2002, doi:10.1109/TEC.2002.801997

[30] M. Jovanovic. (2009, Sensored and sensorless speed control methods for brushless doubly fed reluctance motors. *IET Electric Power Applications 3(6),* 503-513. Available: https://digital-library.theiet.org/content/journals/10.1049/iet-epa.2008.0227

[31] A. Ibrahim, M. Marei, and H. El-Goharey, "Dynamic Responses Comparison of Control Techniques of BDFRG based WECS," *International Journal of Scientific & Engineering Research,* vol. 9, pp. 1, 672-1, 678, 2018,

[32]   M. Hassan and M. Jovanovic, "Improved scalar control using flexible DC-Link voltage in Brushless Doubly-Fed Reluctance Machines for wind applications," in *2012 2nd International Symposium On Environment Friendly Energies And Applications*, 2012, pp. 482-487, doi:10.1109/EFEA.2012.6294037

[33]   M. G. Mousa, S. M. Allam, and E. M. Rashad, "Sensored and sensorless scalar-control strategy of a wind-driven BDFRG for maximum wind-power extraction," *Journal of Control and Decision,* vol. 5, pp. 209-227, 2018/04/03 2018, doi:10.1080/23307706.2017.1353930

[34]   T. Taluo, L. Ristić, and M. Jovanović, "Performance analysis of brushless doubly fed reluctance machines," in *2019 20th International Symposium on Power Electronics (Ee)*, Novi Sad, Serbia, 2019: IEEE, pp. 1-6, doi:10.1109/PEE.2019.8923437

[35]   S. Ademi and M. G. Jovanović, "Vector Control Methods for Brushless Doubly Fed Reluctance Machines," *IEEE Transactions on Industrial Electronics,* vol. 62, pp. 96-104, 2015, doi:10.1109/TIE.2014.2327564

[36]   M. G. Mousa, S. M. Allam, and E. M. Rashad, "A comparative study of vector-control strategies for maximum wind-power extraction of a grid-connected wind-driven brushless doubly-fed reluctance generator," *Australian Journal of Electrical and Electronics Engineering,* vol. 14, pp. 1-11, 2017, doi:10.1080/1448837X.2017.1410964

[37]   M. Kumar, S. Das, and K. Kiran, "Sensorless Speed Estimation of Brushless Doubly-Fed Reluctance Generator Using Active Power Based MRAS," *IEEE Transactions on Power Electronics,* vol. 34, pp. 7878-7886, 2019, doi:10.1109/TPEL.2018.2882473

[38]   H. Chaal and M. Jovanovic, "Practical Implementation of Sensorless Torque and Reactive Power Control of Doubly Fed Machines," *IEEE Transactions on Industrial Electronics,* vol. 59, pp. 2645-2653, 2012, doi:10.1109/TIE.2011.2161065

[39]   H. Chaal and M. Jovanovic, "Toward a Generic Torque and Reactive Power Controller for Doubly Fed Machines," *IEEE Transactions on Power Electronics,* vol. 27, pp. 113-121, 2012, doi:10.1109/TPEL.2011.2160731

[40]   S. Ademi and M. Jovanović, "A novel sensorless speed controller design for doubly-fed reluctance wind turbine generators," *Energy Conversion and Management,* vol. 120, pp. 229-237, 2016/07/15/ 2016, doi:10.1016/j.enconman.2016.04.084

[41]   K. Kiran and S. Das, "Implementation of reactive power-based MRAS for sensorless speed control of brushless doubly fed reluctance motor drive," *IET Power Electronics,* vol. 11, pp. 192-201, 2018, doi:10.1049/iet-pel.2017.0104

[42]   M. R. Agha-Kashkooli and M. Jovanović, "Sensorless MRAS control of emerging doubly-fed reluctance wind generators," *IET Renewable Power Generation,* vol. 15, pp. 2007-2021, 2021, doi:10.1049/rpg2.12123

[43]   M. R. Agha Kashkooli and M. G. Jovanović, "Parameter independent control of doubly-fed reluctance wind generators without a rotor position sensor," *International Journal of Electrical Power & Energy Systems,* vol. 137, p. 107778, 2022/05/01/ 2022, doi:https://doi.org/10.1016/j.ijepes.2021.107778

[44]   H. Chaal, M. Jovanovic, and K. Busawon, "Sliding Mode Observer based direct torque control of a Brushless Doubly-Fed Reluctance Machine," in *2009 IEEE Symposium on Industrial Electronics & Applications*, 2009, pp. 866-871, doi:10.1109/ISIEA.2009.5356345

[45]   M. G. Mousa, S. M. Allam, and E. M. Rashad, "Maximum power extraction under different vector-control schemes and grid-synchronization strategy of a wind-driven Brushless

Doubly-Fed Reluctance Generator," *ISA Transactions,* vol. 72, pp. 287-297, 2018/01/01/ 2018, doi:10.1016/j.isatra.2017.10.005

[46]   H. Chaal and M. Jovanovic, "Power control of brushless doubly-fed reluctance drive and generator systems," *Renewable Energy,* vol. 37, pp. 419-425, 2012/01/01/ 2012, doi:10.1016/j.renene.2011.06.011

[47]   M. Moazen, R. Kazemzadeh, and M.-R. Azizian, "Model-based predictive direct power control of brushless doubly fed reluctance generator for wind power applications," *Alexandria Engineering Journal,* vol. 55, pp. 2497-2507, 2016/09/01/ 2016, doi:10.1016/j.aej.2016.08.004

[48]   F. Zhang, L. Zhu, S. Jin, X. Su, S. Ademi, and W. Cao, "Controller Strategy for Open-Winding Brushless Doubly Fed Wind Power Generator With Common Mode Voltage Elimination," *IEEE Transactions on Industrial Electronics,* vol. 66, pp. 1098-1107, 2019, doi:10.1109/TIE.2018.2811370

[49]   S. Jin, L. Shi, L. Zhu, W. Cao, T. Dong, and F. Zhang, "Dual Two-Level Converters Based on Direct Power Control for an Open-Winding Brushless Doubly-Fed Reluctance Generator," *IEEE Transactions on Industry Applications,* vol. 53, pp. 3898-3906, 2017, doi:10.1109/TIA.2017.2693959

[50]   H. Chaal and M. Jovanovic, "Direct Power Control of Brushless Doubly-Fed Reluctance Machines," in *5th IET International Conference on Power Electronics, Machines and Drives (PEMD 2010)*, 2010, pp. 1-6, doi:10.1049/cp.2010.0148

[51]   J. Shi, Z. Fengge, F. Shibo, Z. Liancheng, and C. Wenping, "Power Decoupling Control of Open-Winding Brushless Doubly-Fed Reluctance Machine for Wind Power Generator Application," *International Journal of Control and Automation,* vol. 8, pp. 173-182, 09/30 2015, doi:10.14257/ijca.2015.8.9.17

[52]   F. Zhang, L. Zhu, S. Jin, W. Cao, D. Wang, and J. L. Kirtley, "Developing a New SVPWM Control Strategy for Open-Winding Brushless Doubly Fed Reluctance Generators," *IEEE Transactions on Industry Applications,* vol. 51, pp. 4567-4574, 2015, doi:10.1109/TIA.2015.2461614

[53]   A. Sahu, K. Kiran, and S. Das, "Particle Swarm Optimization based tuning of brushless doubly-fed reluctance machine drive for speed control applications," in *2016 IEEE 1st International Conference on Power Electronics, Intelligent Control and Energy Systems (ICPEICES)*, 2016, pp. 1-6, doi:10.1109/ICPEICES.2016.7853163

[54]   O. Sadeghian, S. Tohidi, B. Mohammadi-Ivatloo, and F. Mohammadi, "A Comprehensive Review on Brushless Doubly-Fed Reluctance Machine," *Sustainability,* vol. 13, p. 842, 2021, doi:10.3390/su13020842

[55]   E. Muljadi, D. Yildirim, T. Batan, and C. P. Butterfield, "Understanding the unbalanced-voltage problem in wind turbine generation," in *Conference Record of the 1999 IEEE Industry Applications Conference. Thirty-Forth IAS Annual Meeting (Cat. No.99CH36370)*, 1999, pp. 1359-1365 vol.2, doi:10.1109/IAS.1999.801678

[56]   T. Brekken, N. Mohan, and T. Undeland, "Control of a doubly-fed induction wind generator under unbalanced grid voltage conditions," in *2005 European Conference on Power Electronics and Applications*, 2005: IEEE, pp. 10 pp.-P. 10, doi:10.1109/EPE.2005.219315

[57] R. Cardenas, R. Peña, S. Alepuz, and G. Asher, "Overview of control systems for the operation of DFIGs in wind energy applications," *IEEE Transactions on Industrial Electronics,* vol. 60, pp. 2776-2798, 2013, doi:10.1109/TIE.2013.2243372

[58] M. Moazen, R. Kazemzadeh, and M. R. Azizian, "A model-based PDPC method for control of BDFRG under unbalanced grid voltage condition using power compensation strategy," *Journal of Operation and Automation in Power Engineering,* vol. 8, pp. 128-140, 2020, doi:10.22098/joape.2020.5286.1392

[59] Y. El Karkri, A. B. Rey-Boué, H. El Moussaoui, J. Stöckl, and T. I. Strasser, "Improved Control of Grid-connected DFIG-based Wind Turbine using Proportional-Resonant Regulators during Unbalanced Grid," *Energies,* vol. 12, p. 4041, 2019, doi:10.3390/en12214041

[60] J. Chhor, P. Tourou, and C. Sourkounis, "Mitigation of oscillations in DFIG-based WECS operating in unbalanced networks," in *2015 23rd Mediterranean Conference on Control and Automation (MED)*, 2015, pp. 465-471, doi:10.1109/MED.2015.7158792

[61] M. Moazen, R. Kazemzadeh, and M.-R. Azizian, "Mathematical modeling and analysis of brushless doubly fed reluctance generator under unbalanced grid voltage condition," *International Journal of Electrical Power & Energy Systems,* vol. 83, pp. 547-559, 2016/12/01/ 2016, doi:10.1016/j.ijepes.2016.04.050

[62] I. Khan, K. Zeb, W. U. Din, S. U. Islam, M. Ishfaq, S. Hussain*, et al.*, "Dynamic Modeling and Robust Controllers Design for Doubly Fed Induction Generator-Based Wind Turbines under Unbalanced Grid Fault Conditions," *Energies,* vol. 12, p. 454, 2019, doi:10.3390/en12030454

[63] D. Sun, Y. Wang, T. Jiang, X. Wang, J. Sun, and H. Nian, "Multi-Target Control Strategy of DFIG Using Virtual Synchronous Generator Based on Extended Power Resonance Control under Unbalanced Power Grid," *Energies,* vol. 13, p. 2232, 2020, doi:10.3390/en13092232

[64] G. F. Gontijo, T. C. Tricarico, B. W. França, L. F. Da Silva, E. L. Van Emmerik, and M. Aredes, "Robust model predictive rotor current control of a DFIG connected to a distorted and unbalanced grid driven by a direct matrix converter," *IEEE Transactions on Sustainable Energy,* vol. 10, pp. 1380-1392, 2018, doi:10.1109/TSTE.2018.2868406

[65] S. Das and B. Singh, "Enhanced Control of DFIG Based Wind Energy Conversion System Under Unbalanced Grid Voltages Using Mixed Generalized Integrator," *IEEE Journal of Emerging and Selected Topics in Industrial Electronics,* vol. 3, pp. 308-320, 2022, doi:10.1109/JESTIE.2022.3143821

[66] B. I. Nass, T. M. Undeland, and T. Gjengedal, "Methods for reduction of voltage unbalance in weak grids connected to wind plants," in *IEEE/CIGRE Workshop on Wind Power and the Impacts on Power Systems*, 2002: Citeseer, pp. 1-7,

[67] J. Hu and Y. He, "Modeling and enhanced control of DFIG under unbalanced grid voltage conditions," *Electric Power Systems Research,* vol. 79, pp. 273-281, 2009/02/01/ 2009, doi:10.1016/j.epsr.2008.06.017

[68] J. Hu, Y. He, L. Xu, and B. W. Williams, "Improved control of DFIG systems during network unbalance using PI–R current regulators," *IEEE Transactions on Industrial Electronics,* vol. 56, pp. 439-451, 2008, doi:10.1109/TIE.2008.2006952

[69]   A. Luna, K. Lima, F. Corcoles, E. Watanabe, P. Rodriguez, and R. Teodorescu, "Control of DFIG-WT under unbalanced grid voltage conditions," in *2009 IEEE Energy Conversion Congress and Exposition*, 2009: IEEE, pp. 370-377, doi:10.1109/ECCE.2009.5316125

[70]   M. R. Rathi, P. P. Jose, and N. Mohan, "A novel h/sub/spl infin//based controller for wind turbine applications operating under unbalanced voltage conditions," in *Proceedings of the 13th International Conference on, Intelligent Systems Application to Power Systems*, 2005: IEEE, p. 6 pp., doi:10.1109/ISAP.2005.1599289

[71]   T. Brekken and N. Mohan, "A novel doubly-fed induction wind generator control scheme for reactive power control and torque pulsation compensation under unbalanced grid voltage conditions," in *IEEE 34th Annual Conference on Power Electronics Specialist, 2003. PESC'03.*, 2003: IEEE, pp. 760-764, doi:10.1109/PESC.2003.1218151

[72]   T. K. A. Brekken and N. Mohan, "Control of a Doubly Fed Induction Wind Generator Under Unbalanced Grid Voltage Conditions," *IEEE Transactions on Energy Conversion,* vol. 22, pp. 129-135, 2007, doi:10.1109/TEC.2006.889550

[73]   L. Xu and Y. Wang, "Dynamic Modeling and Control of DFIG-Based Wind Turbines Under Unbalanced Network Conditions," *IEEE Transactions on Power Systems,* vol. 22, pp. 314-323, 2007, doi:10.1109/TPWRS.2006.889113

[74]   L. Xu, "Coordinated Control of DFIG's Rotor and Grid Side Converters During Network Unbalance," *IEEE Transactions on Power Electronics,* vol. 23, pp. 1041-1049, 2008, doi:10.1109/TPEL.2008.921157

[75]   L. Xu, "Enhanced control and operation of DFIG-based wind farms during network unbalance," *IEEE Transactions on Energy Conversion,* vol. 23, pp. 1073-1081, 2008, doi:10.1109/TEC.2008.2001452

[76]   M. Moazen, R. Kazemzadeh, and M.-R. Azizian, "Mathematical proof of BDFRG model under unbalanced grid voltage condition," *Sustainable Energy, Grids and Networks,* vol. 21, p. 100327, 2020/03/01/ 2020, doi:https://doi.org/10.1016/j.segan.2020.100327

[77]   T. Taluo, L. Ristić, and M. Jovanović, "Dynamic Modeling and Control of BDFRG under Unbalanced Grid Conditions," *Energies,* vol. 14, p. 4297, 2021, doi:10.3390/en14144297

[78]   F. Zhang, S. Yu, Y. Wang, S. Jin, and M. G. Jovanovic, "Design and Performance Comparisons of Brushless Doubly Fed Generators With Different Rotor Structures," *IEEE Transactions on Industrial Electronics,* vol. 66, pp. 631-640, 2019, doi:10.1109/TIE.2018.2811379

[79]   A. Khan, X. M. Hu, M. A. Khan, and P. Barendse, "Doubly Fed Induction Generator Open Stator Synchronized Control during Unbalanced Grid Voltage Condition," *Energies,* vol. 13, p. 3155, 2020, doi:10.3390/en13123155

[80]   M. G. Jovanovic, "Power factor and inverter rating. A compromise in doubly fed reluctance machine drives," in *2000 Eighth International Conference on Power Electronics and Variable Speed Drives (IEE Conf. Publ. No. 475)*, 2000, pp. 311-316, doi:10.1049/cp:20000264

[81]   M. G. Jovanovic, J. Yu, and E. Levi, "A review of control methods for brushless doubly-fed reluctance machines," in *2002 International Conference on Power Electronics, Machines and Drives (Conf. Publ. No. 487)*, 2002, pp. 528-533, doi:10.1049/cp:20020172

[82] M. Jovanovic and R. E. Betz, "Optimal performance of brushless doubly fed reluctance machines," in *1999. Ninth International Conference on Electrical Machines and Drives (Conf. Publ. No. 468)*, 1999, pp. 386-390, doi:10.1049/cp:19991056

[83] T. Staudt, F. Wurtz, N. J. Batistela, and P. Kuo-Peng, "Influence of rotor design and geometric parameter variation on global performance of Brushless Doubly-Fed Reluctance Machines," in *2014 International Conference on Electrical Machines (ICEM)*, 2014, pp. 537-543, doi:10.1109/ICELMACH.2014.6960232

[84] J. Carroll, A. McDonald, and D. McMillan, "Reliability Comparison of Wind Turbines With DFIG and PMG Drive Trains," *IEEE Transactions on Energy Conversion,* vol. 30, pp. 663-670, 2015, doi:10.1109/TEC.2014.2367243

[85] S. Ademi and M. Jovanovic, "High-efficiency control of brushless doubly-fed machines for wind turbines and pump drives," *Energy Conversion and Management,* vol. 81, pp. 120-132, 2014/05/01/ 2014, doi:10.1016/j.enconman.2014.01.015

[86] M. G. Jovanovic and D. G. Dorrell, "Sensorless Control of Brushless Doubly-Fed Reluctance Machines using an Angular Velocity Observer," in *2007 7th International Conference on Power Electronics and Drive Systems*, 2007, pp. 717-724, doi:10.1109/PEDS.2007.4487782

[87] L. Morel, H. Godfroid, A. Mirzaian, and J. Kauffmann, "Double-fed induction machine: converter optimisation and field oriented control without position sensor," *IEE Proceedings-Electric Power Applications,* vol. 145, pp. 360-368, 1998, doi:10.1049/ip-epa:19981982

[88] B. Bird and R. Burbidge, "Analysis of doubly fed slip-ring machines," in *Proceedings of the Institution of Electrical Engineers*, 1966: IET, pp. 1016-1020, doi:10.1049/piee.1966.0167

[89] M. G. Jovanovic, R. E. Betz, J. Yu, and E. Levi, "Aspects of vector and scalar control of brushless doubly fed reluctance machines," in *4th IEEE International Conference on Power Electronics and Drive Systems. IEEE PEDS 2001-Indonesia. Proceedings (Cat. No. 01Th8594)*, 2001: IEEE, pp. 461-467, doi:10.1109/PEDS.2001.975360

[90] M. Arifujjaman, M. Iqbal, and J. E. Quaicoe, "Vector control of a DFIG based wind turbine," *IU-Journal of Electrical & Electronics Engineering,* vol. 9, pp. 1057-1066, 2009,

[91] S. Muller, M. Deicke, and R. W. De Doncker, "Doubly fed induction generator systems for wind turbines," *IEEE Industry applications magazine,* vol. 8, pp. 26-33, 2002, doi:10.1109/2943.999610

[92] H. Akagi and H. Sato, "Control and performance of a doubly-fed induction machine intended for a flywheel energy storage system," *IEEE Transactions on Power Electronics,* vol. 17, pp. 109-116, 2002, doi:10.1109/63.988676

[93] M. Yamamoto and O. Motoyoshi, "Active and reactive power control for doubly-fed wound rotor induction generator," *IEEE Transactions on Power Electronics,* vol. 6, pp. 624-629, 1991, doi:10.1109/63.97761

[94] S. Ademi and M. Jovanovic, "Vector control strategies for brushless doubly-fed reluctance wind generators," in *2012 2nd International Symposium On Environment Friendly Energies And Applications*, 2012: IEEE, pp. 44-49, doi:10.1109/EFEA.2012.6294084

[95] T. Lei, "Doubly-fed induction generator wind turbine modelling, control and reliability," Phd thesis, The University of Manchester (United Kingdom), 2014.

[96] L. Dai and D. Tung, "Modeling for Development of Simulation Tool: A Case Study of Grid Connected Doubly Fed Induction Generator Based on Wind Energy Conversion System," *International Journal of Applied Engineering Research,* vol. 12, pp. 2981-2996, 2017,

[97] M. G. Jovanovic, Y. Jian, and E. Levi, "Encoderless direct torque controller for limited speed range applications of brushless doubly fed reluctance motors," *IEEE Transactions on Industry Applications,* vol. 42, pp. 712-722, 2006, doi:10.1109/TIA.2006.872955

[98] H. Chaal and M. Jovanovic, "A new sensorless torque and reactive power controller for doubly-fed machines," in *The XIX International Conference on Electrical Machines-ICEM 2010*, 2010: IEEE, pp. 1-6, doi:10.1109/ICELMACH.2010.5608111

[99] M. G. Jovanovic, J. Yu, and E. Levi, "Encoderless direct torque controller for limited speed range applications of brushless doubly fed reluctance motors," *IEEE Transactions on Industry Applications,* vol. 42, pp. 712 - 722, May-June 2006,

[100] E. Muljadi, R. Schiferl, and T. A. Lipo, "Induction machine phase balancing by unsymmetrical thyristor voltage control," *IEEE transactions on industry applications,* pp. 669-678, 1985, doi:10.1109/TIA.1985.349484

[101] E. Ozsoy, S. Padmanaban, L. Mihet-Popa, V. Fedák, F. Ahmad, R. Akhtar*, et al.*, "Control Strategy for a Grid-Connected Inverter under Unbalanced Network Conditions—A Disturbance Observer-Based Decoupled Current Approach," *Energies,* vol. 10, p. 1067, 2017, doi:10.3390/en10071067

[102] K. Lee, T. M. Jahns, T. A. Lipo, and V. Blasko, "New Control Method Including State Observer of Voltage Unbalance for Grid Voltage-Source Converters," *IEEE Transactions on Industrial Electronics,* vol. 57, pp. 2054-2065, 2010, doi:10.1109/TIE.2009.2033488

[103] S. Shao, T. Long, E. Abdi, and R. A. McMahon, "Dynamic Control of the Brushless Doubly Fed Induction Generator Under Unbalanced Operation," *IEEE Transactions on Industrial Electronics,* vol. 60, pp. 2465-2476, 2013, doi:10.1109/TIE.2012.2211313

[104] K. Miettinen, F. Ruiz, and A. P. Wierzbicki, "Introduction to Multiobjective Optimization: Interactive Approaches," in *Multiobjective Optimization: Interactive and Evolutionary Approaches*, J. Branke, K. Deb, K. Miettinen, and R. Słowiński, Eds., ed Berlin, Heidelberg: Springer Berlin Heidelberg, 2008, pp. 27-57, doi:10.1007/978-3-540-88908-3_2

[105] R. T. Marler and J. S. Arora, "The weighted sum method for multi-objective optimization: new insights," *Structural and Multidisciplinary Optimization,* vol. 41, pp. 853-862, 2010/06/01 2010, doi:10.1007/s00158-009-0460-7

[106] F. K. Moghadam, S. Ebrahimi, A. Oraee, and J. M. Velni, "Vector control optimization of DFIGs under unbalanced conditions," *International Transactions on Electrical Energy Systems,* vol. 28, p. e2583, 2018, doi:https://doi.org/10.1002/etep.2583

[107] E. M. Schulz and R. E. Betz, "Optimal torque per amp for brushless doubly fed reluctance machines," in *Fourtieth IAS Annual Meeting. Conference Record of the 2005 Industry Applications Conference, 2005.*, 2005, pp. 1749-1753 Vol. 3, doi:10.1109/IAS.2005.1518683

[108] I. Boldea, Z. Fu, and S. Nasar, "Performance evaluation of axially-laminated anisotropic (ALA) rotor reluctance synchronous motors," *IEEE transactions on industry applications,* vol. 30, pp. 977-985, 1994, doi:10.1109/28.297915

[109]   A. Vagati, M. Pastorelli, G. Francheschini, and S. C. Petrache, "Design of low-torque-ripple synchronous reluctance motors," *IEEE Transactions on Industry Applications,* vol. 34, pp. 758-765, 1998, doi:10.1109/28.703969

[110]   D. G. Dorrell, A. M. Knight, and R. E. Betz, "Issues with the design of brushless doubly-fed reluctance machines: Unbalanced magnetic pull, skew and iron losses," in *2011 IEEE International Electric Machines & Drives Conference (IEMDC),* 2011: IEEE, pp. 663-668, doi:10.1109/IEMDC.2011.5994890

[111]   T. Fukami, M. Momiyama, K. Shima, R. Hanaoka, and S. Takata, "Steady-State Analysis of a Dual-Winding Reluctance Generator With a Multiple-Barrier Rotor," *IEEE Transactions on Energy Conversion,* vol. 23, pp. 492-498, 2008, doi:10.1109/TEC.2008.918656

[112]   A. M. Knight, R. E. Betz, and D. G. Dorrell, "Design and Analysis of Brushless Doubly Fed Reluctance Machines," *IEEE Transactions on Industry Applications,* vol. 49, pp. 50-58, 2013, doi:10.1109/TIA.2012.2229451

[113]   A. M. Knight, R. E. Betz, and D. Dorrell, "Design principles for brushless doubly fed reluctance machines," in *IECON 2011 - 37th Annual Conference of the IEEE Industrial Electronics Society*, 2011, pp. 3602-3607, doi:10.1109/IECON.2011.6119894

[114]   A. M. Knight, R. E. Betz, W. K. Song, and D. G. Dorrell, "Brushless doubly-fed reluctance machine rotor design," in *2012 IEEE Energy Conversion Congress and Exposition (ECCE)*, 2012, pp. 2308-2315, doi:10.1109/ECCE.2012.6342466

[115]   T. Jokinen, V. Hrabovcova, and J. Pyrhonen, *Design of rotating electrical machines*: John Wiley & Sons, 2013.

[116]   S. Agrawal, A. Banerjee, and R. F. Beach, "Brushless Doubly-Fed Reluctance Machine Drive for Turbo- Electric Distributed Propulsion Systems," in *2018 AIAA/IEEE Electric Aircraft Technologies Symposium (EATS)*, 2018, pp. 1-17, doi:10.2514/6.2018-4987

[117]   T. K. Mersha and C. Du, "Co-Simulation and Modeling of PMSM Based on Ansys Software and Simulink for EVs," *World Electric Vehicle Journal,* vol. 13, p. 4, 2022, doi:10.3390/wevj13010004

[118]   P. Nagarajan, "ELECTROMAGNETIC SIGNATURE STUDY OF A CLOSED LOOP SPEED CONTROLLED THREE-PHASE INDUCTION MOTOR UNDER BROKEN ROTOR BAR FAULT USING FINITE ELEMENT METHOD," *Journal of Engineering Science and Technology,* vol. 14, pp. 2731-274, 10/01 2019,

[119]   M. Salman, "Analysis, design and control aspects of linear machines using co-simulation," Master Thesis Master of Science, Royal Institute of Technology (KTH), 2012.

[120]   L. D. Leonardo, M. Popescu, M. Tursini, and M. Villani, "Finite Elements Model Co-Simulation of an Induction Motor Drive for Traction Application," in *IECON 2019 - 45th Annual Conference of the IEEE Industrial Electronics Society*, 2019, pp. 1059-1065, doi:10.1109/IECON.2019.8926853

[121]   G. Ellis, "Chapter 13 - Model Development and Verification," in *Control System Design Guide (Fourth Edition)*, G. Ellis, Ed., ed Boston: Butterworth-Heinemann, 2012, pp. 261-282, doi:https://doi.org/10.1016/B978-0-12-385920-4.00013-8

[122]   (2014). *DS1103 PPC Controller Board: Hardware Installationand Configuration*. Available: https://www.manualslib.com/manual/1666045/Dspace-Ds1103.html

Biography

Taufik Mohamed G Taluo was born on March 21st, 1974, in Zwara–Libya. He finished elementary and high school in 1993 in Tripoli. And in 1993, he enrolled the Faculty of Engineering at the University of the 7th of April in Libya, where he received a Bachelor's degree in electrical engineering in 1998. He enrolled the Master studies in 2014, in the department of Power Converters and Drives at the School of Electrical Engineering, University of Belgrade, he graduated with an overall average score of 9, where he defended his Master's thesis on December 2016, entitled "Modeling of three phase boost rectifier in electrical drive with frequency converter and analysis of its operation based on simulation results" under the mentorship of Prof. Dr. Leposava Ristić Mr. Taufik enrolled in doctoral studies at the department of Power Converters and Drives at the School of Electrical Engineering, University of Belgrade, in 2018-2019, he passed all the required exams with a grade point average of 10. He worked at "GENERAL ELECTRICITY COMPANY OF LIBYA'' in Zwara–Libya as an engineer from 2000 to 2005, then in the period from 2005 to 2006 he worked at the Repsol Oil Company as an electrical engineer. Since 2009–present he has been a lecturer in the electrical and electronic department, College of Technical Engineering, Zwara-Libya.

List of publications

[1] L. Ristić, M. Bebić, T. Taluo, M. Šinik, I. Mihailović, D. Jevtić, N. Rašić, ANALYSIS OF ENERGY EFFICIENCY AND INFLUENCE TO THE SUPPLY GRID OF ELECTRICAL DRIVES WITH ACTIVE RECTIFIER, VI Regional Conference: "Industrial Energy and Environmental Protection in South Eastern Europe, pp. 1 - 6, Zlatibor, Srbija, Jun, 2017, ISSN/ISBN: 978-86-7877-028-9.

[2] L. Ristić, B. Brković, M. Majstorović, U. Milović, T. Taluo, and M. Bebić, "Electrical Drives with Active Rectifiers Connected to Distorted Utility Grid," in 2018 5th International Symposium on Environment-Friendly Energies and Applications (EFEA), 2018, pp. 1-6, doi:10.1109/EFEA.2018.8617093.

[3] T. Taluo, L. Ristić, M. Jovanović, Performance analysis of doubly fed induction wind generators, VII Regional Conference - Industrial energy and environmental protection in the countries of Southeast Europe, pp. 336 - 347, Thermic Society of Serbia, Zlatibor, June, 2019, ISSN/ISBN   978-86-7877-033-3.

[4] T. Taluo, L. Ristić, M. Jovanović, Performance analysis of brushless doubly fed reluctance machines, XX International Symposium on Power Electronics - Ee 2019, pp. 1 - 6, Society for Power Electronics Novi Sad, Novi Sad, Oct, 2019.

[5] T. Taluo, L. Ristić, M. Jovanović, Voltage Oriented Control Design for Brushless Doubly-Fed Reluctance Machines, 7th international conference IcETRAN 2020, pp. 1 - 6, Novi Sad, Serbia, Sep, 2020.

[6] T. Taluo, L. Ristić, and M. Jovanović, "Dynamic Modeling and Control of BDFRG under Unbalanced Grid Conditions," Energies, vol. 14, p. 4297, 2021, doi:10.3390/en14144297.

Biography

[7] T. Taluo, L. Ristić, M. Jovanović, Steady State analysis of Brushless Doubly Fed Reluctance Generator, 7th International Symposium on Environment-Friendly Energies and Applications (EFEA 2022), pp. 1 - 6, IEEE Xplore, Mauritius, Dec, 2022.

[8] T. Taluo, L. Ristić, B. Brković, M. Terzić, Design and Performance Study of a Large-Scale Brushless Doubly Fed Reluctance Generator, 7th International Symposium on Environment-Friendly Energies and Applications (EFEA 2022), pp. 1 - 6, IEEE Xplore, Mauritius, Dec, 2022.

Изјава о ауторству

Име и презиме аутора __Тауфик Талуо (Taufik Taluo)__

Број индекса _____5046/2018_____

Изјављујем

да је докторска дисертација под насловом

Алгоритам управљања двострано напајаним релуктантним генератором у условима несиметричног мрежног напона

Control Algorithm of Brushless Doubly-Fed Reluctance Generator under Unbalanced Grid Voltage Conditions

- резултат сопственог истраживачког рада;
- да дисертација у целини ни у деловима није била предложена за стицање друге дипломе према студијским програмима других високошколских установа;
- да су резултати коректно наведени и
- да нисам кршио/ла ауторска права и користио/ла интелектуалну својину других лица.

Потпис аутора

У Београду, ___27.02.2023.___

Изјава о истоветности штампане и електронске верзије докторског рада

Име и презиме аутора _____Тауфик Талуо (Taufik Taluo)_____

Број индекса _____5046/2018_____

Студијски програм _____Енергетски претварачи и погони_____

Наслов рада _____Алгоритам управљања двострано напајаним релуктантним генератором у условима несиметричног мрежног напона_____

Ментор _____проф. др Лепосава Ристић, ванредни професор_____

Изјављујем да је штампана верзија мог докторског рада истоветна електронској верзији коју сам предао/ла ради похрањивања у **Дигиталном репозиторијуму Универзитета у Београду.**

Дозвољавам да се објаве моји лични подаци везани за добијање академског назива доктора наука, као што су име и презиме, година и место рођења и датум одбране рада.

Ови лични подаци могу се објавити на мрежним страницама дигиталне библиотеке, у електронском каталогу и у публикацијама Универзитета у Београду.

Потпис аутора

У Београду, _____27.02.2023._____

Изјава о коришћењу

Овлашћујем Универзитетску библиотеку „Светозар Марковић" да у Дигитални репозиторијум Универзитета у Београду унесе моју докторску дисертацију под насловом:

Алгоритам управљања двострано напајаним релуктантним генератором у условима несиметричног мрежног напона

Control Algorithm of Brushless Doubly-Fed Reluctance Generator under Unbalanced Grid Voltage Conditions

која је моје ауторско дело.

Дисертацију са свим прилозима предао/ла сам у електронском формату погодном за трајно архивирање.

Моју докторску дисертацију похрањену у Дигиталном репозиторијуму Универзитета у Београду и доступну у отвореном приступу могу да користе сви који поштују одредбе садржане у одабраном типу лиценце Креативне заједнице (Creative Commons) за коју сам се одлучио/ла.

1. Ауторство (CC BY)

2. Ауторство – некомерцијално (CC BY-NC)

3. Ауторство – некомерцијално – без прерада (CC BY-NC-ND)

4. Ауторство – некомерцијално – делити под истим условима (CC BY-NC-SA)

5. Ауторство – без прерада (CC BY-ND)

6. Ауторство – делити под истим условима (CC BY-SA)

(Молимо да заокружите само једну од шест понуђених лиценци.
Кратак опис лиценци је саставни део ове изјаве).

Потпис аутора

У Београду, _____27.02.2023._____

12